Summer 2007

An intermediate-layer lithography method for producing metal micron/nano patterns and conducting polymer-based microdevices

Xinchuan Liu
Louisiana Tech University

Recommended Citation

AN INTERMEDIATE-LAYER LITHOGRAPHY METHOD FOR

PRODUCING METAL MICRO/NANO PATTERNS AND

CONDUCTING POLYMER-BASED MICRODEVICES

By

Xinchuan Liu, MS

A Dissertation Presented in Partial Fulfillment
of the Requirements for the Degree
Doctor of Philosophy

COLLEGE OF ENGINEERING AND SCIENCE
LOUISIANA TECH UNIVERSITY

August, 2007

UMI Number: 3270931

INFORMATION TO USERS

The quality of this reproduction is dependent upon the quality of the copy submitted. Broken or indistinct print, colored or poor quality illustrations and photographs, print bleed-through, substandard margins, and improper alignment can adversely affect reproduction.

In the unlikely event that the author did not send a complete manuscript and there are missing pages, these will be noted. Also, if unauthorized copyright material had to be removed, a note will indicate the deletion.

UMI®

UMI Microform 3270931

Copyright 2007 by ProQuest Information and Learning Company.

All rights reserved. This microform edition is protected against unauthorized copying under Title 17, United States Code.

ProQuest Information and Learning Company
300 North Zeeb Road
P.O. Box 1346
Ann Arbor, MI 48106-1346

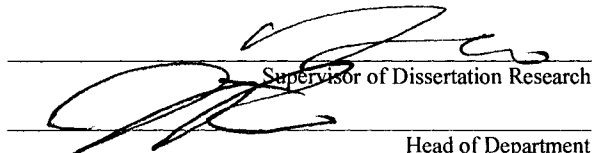# LOUISIANA TECH UNIVERSITY

THE GRADUATE SCHOOL

7/12/2007

_____
Date

We hereby recommend that the dissertation prepared under our supervision

by Xinchuan Liu

entitled An intermediate-layer lithography method for producing metal micro/nano patterns

and conducting polymer-based microdevices

be accepted in partial fulfillment of the requirements for the Degree of

Doctor of Philosophy in Engineering

_____
Supervisor of Dissertation Research

_____
Head of Department

College of Engineering and Science
Department

Recommendation concurred in:

Advisory Committee

Approved:

_____
Director of Graduate Studies

_____
Dean of the College

Approved:

_____
Dean of the Graduate School

GS Form 13
(5/03)

ABSTRACT

Metals have been widely used in the areas of integration circuit (IC) and microelectromechanical systems (MEMS) fields as materials for gates, contact pads, interconnects, corrosion resistance coatings, rectifying contacts, redundancy memories, heating elements, mechanical parts, magnetic component, etc. due to their good properties, such as high electrical conductivity and good thermal conductivity. Conducting polymers, because of their promising potential to replace silicon and metals in building devices, have attracted great attention in recent decades.

Traditional photolithography methods are often used to pattern metals and conducting polymers. However, it cannot be used to fabricate nano patterns because the minimum feature size is limited by wavelength of light. Lithography processes also involve aggressive chemicals, organic solvents, light, or moisture, and thus may affect human health, pollute the environment, and degrade devices. Therefore, a new pattern technique is needed to solve these problems. Soft lithography has been successfully used to fabricate both metal and conducting polymer patterns. The techniques are free of harmful radiations and other chemicals that might alter the properties of the conducting polymer. However, the problems which result from a soft stamp may cause dislocations of patterns or variations of dimensions. The hot embossing process has low cost, high throughout, and high reliability. Also, no chemical etchant or light is involved in this process. On the other hand, it cannot be directly used to pattern metal or conducting

polymer.

Motivated by a macrocutting process often used in the manufacturing industry to pattern sheet metals, an innovative intermediate-layer lithography (ILL) approach is developed in this work to generate micro/nano patterns in a thin metal or conducting polymer film. In the ILL method, an intermediate layer of PMMA is introduced between a silicon substrate and a thin metal or conducting polymer film. Subsequently, the metal or conducting polymer film is imprinted through a mold insertion using a hot embossing technique. The ILL has been applied to produce various micropatterns in Al, PEDOT, and PPy films. Micro devices, such as heaters, diodes and capacitors, were also fabricated using the ILL method. Metal nanopatterns have been successfully generated using this approach. This dissertation addresses the corresponding fabrication details and gives a numerical interpretation of some interesting experimental phenomena observed.

APPROVAL FOR SCHOLARLY DISSEMINATION

The author grants to the Prescott Memorial Library of Louisiana Tech University the right to reproduce, by appropriate methods, upon request, any or all portions of this Dissertation. It is understood that "proper request" consists of the agreement, on the part of the requesting party, that said reproduction is for his personal use and that subsequent reproduction will not occur without written approval of the author of this Dissertation. Further, any portions of the Dissertation used in books, papers, and other works must be appropriately referenced to this Dissertation.

Finally, the author of this Dissertation reserves the right to publish freely, in the literature, at any time, any or all portions of this Dissertation.

Author ___Xinchuan Lin___

Date ___7/16/2007___

TABLE OF CONTENTS

LIST OF TABLES

LIST OF FIGURES

xi

ACKNOWLEDGEMENTS

First, I would like to thank my advisor, Dr. Cheng Luo, for his guidance, encouragement, and support on this dissertation. In four years, he not only taught me scientific working style and research skill, but also strict and meticulous scholarship.

Second, I would like to thank my advisory committee members, Mr. Ji Fang, Dr. Jun-ing Ker, Dr. Chester Wilson, and Dr. Yuri Lvov. They gave me lots of helpful advice for this dissertation. I also thank all the faculty and staff at Louisiana Tech University, especially Mr. Donald Tatum and Dr. Karen Xu, who helped me with the operation of the hot embossing machine and metrology instruments.

I thank my friendly group members, Anirban Chakraborty, Ganga Parthasarathi, Fang Meng, Hao Li, Hui Wang, Si Chen, Rakesh S. Poddar, Anand Francis, and Yiyun Guo, for their co-operation and continuous support.

This dissertation is also a present for my family. I thank my wife, my daughter, and my son for their everlasting and unconditional support and love. I thank my parents and my sisters for their long-time love and education.

CHAPTER 1

INTRODUCTION

1.1 Introduction

Metals have been widely used in the areas of integration circuit (IC) and microelectromechanical systems (MEMS) fields as materials for gates, contact pads, interconnects, corrosion resistance coatings, rectifying contacts, redundancy memories, heating elements, mechanical parts, magnetic component, etc. [1-3] due to their good properties, such as high electrical conductivity and good thermal conductivity. Conducting polymers, because of their promising potential to replace silicon and metals in building devices, have attracted great attention since the discovery of high conductivity in doped polyacetylene in 1977 [4]. Since then, many researchers have been working on the mechanism of polymer conduction and development of polymer microelectronic devices. Compared with Si-based devices, conducting polymer-based devices have the distinctive advantages of low weight and good flexibility, and may potentially replace the corresponding Si-based devices.

The minimum feature size of traditional lithography methods is limited by the wavelength of light. These methods also involve aggressive chemicals, organic solvents, light, or moisture, which may affect human health, pollute the environment, and degrade electrical devices. In this work, stimulated by a macrocutting process commonly

1

used in the metal manufacturing industry to create macropatterns in a sheet metal, the ILL approach was applied to generate metal [5] and conducting polymer [6-8] micropatterns using a single mold insertion. Compared with standard ultra-violet lithography, the patterning process of the ILL has the distinctive advantage of simplicity, is free of aggressive chemistry, and breaks through the limitation of wavelength of light.

1.2 Current Methods to Pattern Metal and Conducting Polymer

Generally, metal film is deposited on a substrate. There are two types of deposition processes: physical vapor deposition (PVD) and chemical vapor deposition (CVD) [1-3]. Chemical vapor deposition (CVD) is an approach with excellent step coverage, large throughout, and low-temperature processing. Although Tungsten and molybdenum have been successfully deposited using LPCVD (low-pressure chemical vapor deposition), most metal films are deposited using PVD. The simplest method of PVD is thermal evaporation. Metal materials are evaporated via heating (e.g., using electrical resistor, inductive frequency or laser) or electron bombardment (e.g., using e-gun) and then condensed on a substrate to form metal films. Compared to the sputtering process (another PVD process), lower vacuum pressure causes few or negligible gas entrapment in thermal evaporation. In sputter deposition, energetic ions bombard target metal materials and release surface metal atoms from the target. The released atoms are condensed on a substrate to form metal film. Although the sputtering process is very well controlled, it is easy to trap gases because it is operated at relatively high pressure. The trapped gas atoms may cause stress changes and propertied degrading.

Since most pre-polymers of most conducting polymers can be solved in water or organic solvents, cast and spinning-coating are the major deposition methods to form conducting polymer film on a substrate.

Various patterning techniques have been already developed and are used extensively to fabricate devices.

1.2.1 Photolithography

Lithography approach is the most basic process in microfabrication to transfer geometric pattern from a photomask to a light-sensitive chemical (photoresist, or simply "resist") on the substrate. The procedure of lithography is schematically illustrated in Fig. 1.1. A thin photoresist film is spinning-coated on a substrate. Visible or ultraviolet (UV) light travels across a photomask, which blocks it in some areas and lets it pass in others. Development of the photoresist in a developer solution after its exposure to light produces a resist pattern on the wafer. Two types of photoresist materials are negative and positive photoresists. Negative resists become less soluble in the developer solution when exposed to light, forming negative images of the mask patterns on the wafer. Positive resists become more soluble in the developer when exposed to light, forming positive images of the mask patterns on the wafer. The utility of following processes, such as chemical etching and lift-off, transfer patterns from the photoresist to the substrate.
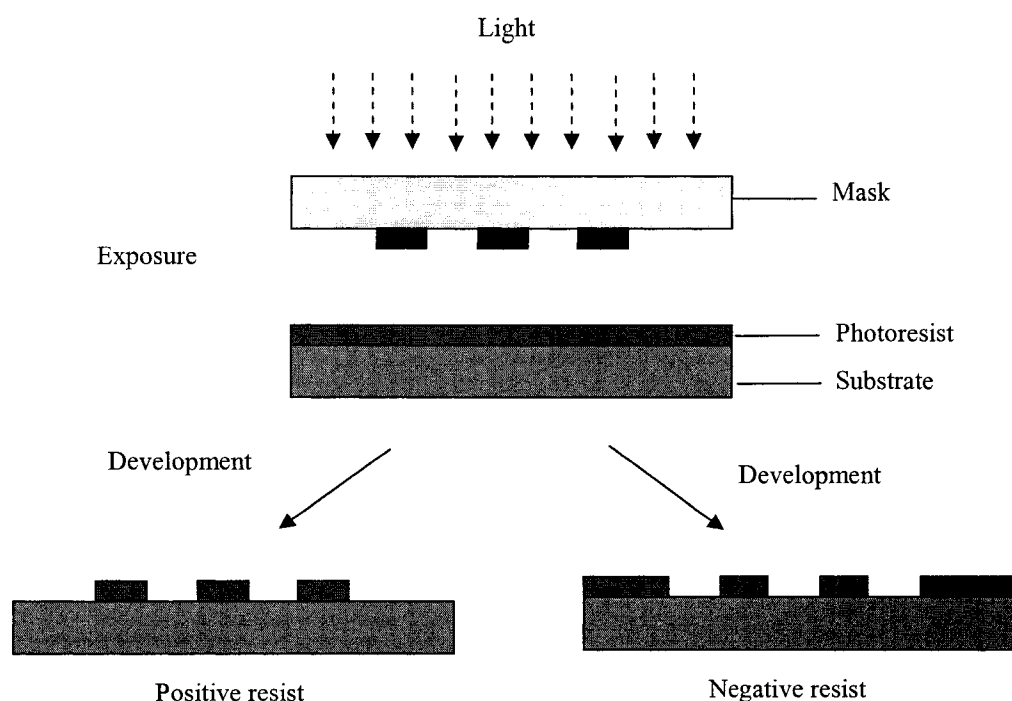
Light

Figure 1.1 Schematic illustration of lithography process.

Photolithography is the most widely used pattern technique because it can exactly control the shape and dimension of the features. However, because the wavelength of UV light ranges from 200 – 400 nm, the minimum feature size created using photolithography is limited in this range due to the effect of light diffraction. Moreover, it requires a flat substrate and extremely clean operating conditions.

Chemical wet and dry etching processes [1-3] (Fig. 1.2) which often follow photolithography process, are the most widely used approaches to pattern metal and conducting polymer film. Metal or conducting polymer film is coated on a substrate first. A layer of organic resist is then coated on the top surface. Photolithographic process, laser beam, or electron beam (e-beam) may be used to pattern the protective resist. Strong corrosive acidic or alkaline solutions (HF, HNO$_3$, H$_3$PO$_4$, CH$_3$COOH, HCl, H$_2$SO$_4$, KOH, etc.), flourine- or chlorine-containing gases (CF$_4$, SF$_6$, Cl$_2$, CCl$_3$F, CCl$_4$, BCl$_3$,

etc.), or organic solvents (acetone, toluene, chloroform, etc.) are used to attack unprotected metal or conducting polymers to control feature dimensions. After selective removal of the resist, metal or conducting polymer patterns are left on the substrate. Chemical etching is simple and easy to be operated. However, aggressive chemicals do harm to human health and pollute the environment. The residue of those chemical (e.g. Cl^-, F^- and K^+) degrades properties of devices. Some polymers can be patterned directly using light or electron beams without strong chemicals. For example, poly(alkylthiopenes) cross-link under UV irradiation [9,10], although that may also cause the polymer to degrade.

(a) Coat metal or conducting polymer on a substrate, then coat and pattern protective mask layer on the top.

(b) Remove the exposed metal or conducting polymer using wet/dry etching.

(c) Remove the protective mask and leave the desired patterns on the substrate.
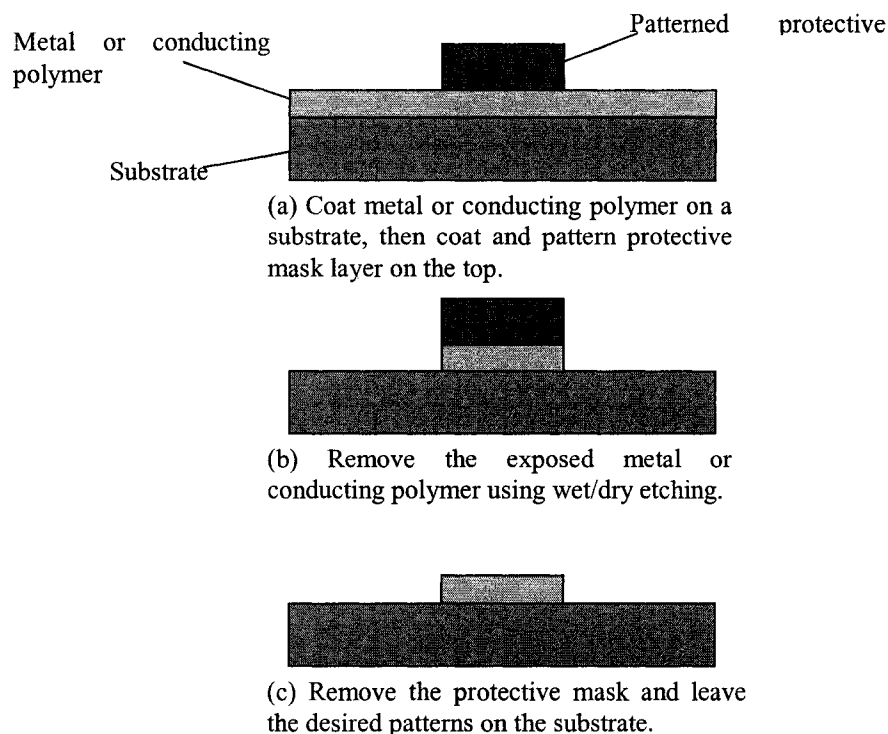
Figure 1.2 Schematic illustration of chemical etching.

Lift-off is a common patterning method. The basic procedure is shown in Fig. 1.3. A layer of sacrificial organic material is coated on a substrate first, and then it is patterned using the lithography approach (Fig. 1.3a). Sequent, metal, or conducting

polymer film is coated (Fig. 1.3b). The sacrificial layer is removed along with the metal or conducting polymer on it, using organic solvent. Desired metal or conducting polymer film patterns are left on the substrate (Fig. 1.3c). Lift-off process is simple and easy to operate. However, round profile limits its application.
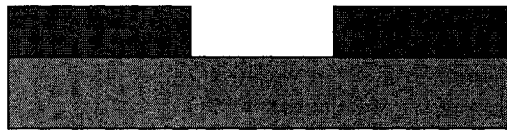
(a) Coat and pattern sacrificial layer.
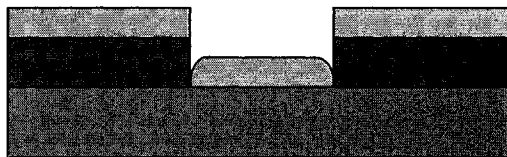
(b) Deposit metal or conducting polymer.

(c) Remove the sacrificial layer.

Figure 1.3 Procedure of lift-off.

Self-aligned silicide process is used to pattern metal on silicon wafers without any additional lithography and alignment [1]. The silicon-silicide interfaces are very clean. However, chemical aggressive etchant is still needed to remove the unwanted (unreacted) metal in this method. A brief procedure of self-align silicide process is shown in Fig. 1.4: silicon wafer is patterned initially. A layer of metal film is deposited on it. Annealing is carried out to form silicide at the interface between silicon and metal. Unwanted metal is etched by wet etching.

Polysilicon

SiO$_2$

Silicon wafer

(a) Pattern Si wafer.

Metal

(b) Deposit metal film and anneal.

(c) Etch out unwanted metal.
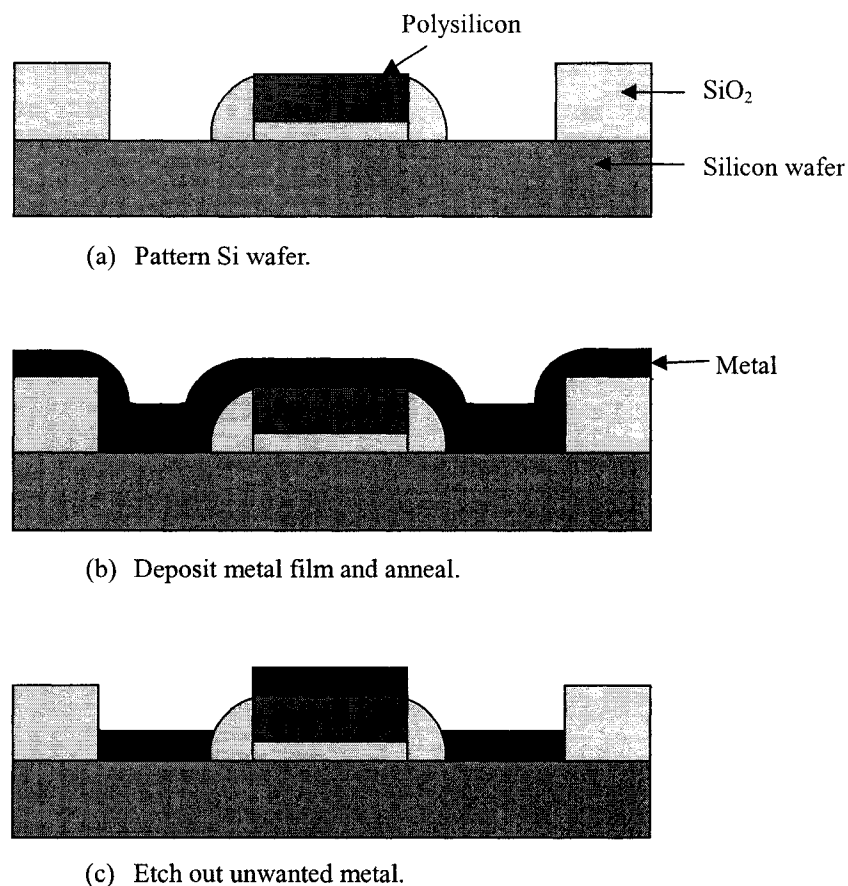
Figure 1.4 Procedure of self-align silicide.

1.2.2 Soft Lithography

Soft lithography is often used to pattern both conducting polymers and metals [11-14]. Soft lithography techniques are free of harmful radiations and other chemicals that might alter the properties of the conducting polymer, which include microcontact printing (μCP), replica molding (REM), microtransfer molding (μTM), micromolding in capillaries (MIMIC), and solvent-assisted micromolding (SAMIM) [11-14]. Elastometric stamp or mold is the key element to transfer patterns in those techniques. Hence, they are called 'soft lithography'.

A versatile and cost-effective method to pattern self-assembled monolayers (SAMs) is μCP. The procedure is very simple (Fig. 1.5). An elastomeric stamp, which is made from polydimethylsiloxane (PDMS), is coated with a layer of 'ink' with an appropriate solution of alkanethiol. Then it is stamped on a substrate with gold, silver, or copper film. The ink molecules are transferred to the surface of the substrate. The patterned SAMs might be resists in selective etching or templates in selective deposition for various materials: metals, silicon, liquids, polymers, and biomaterials.
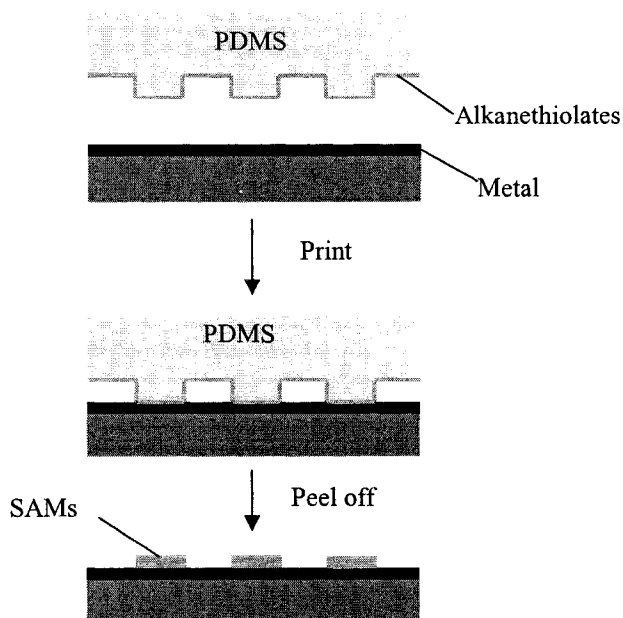
Figure 1.5 Procedure of μCP.

In REM (Fig. 1.6), the prepolymer solution is casted on a PDMS mold first. It has to be cured and solidified. Then it has to be peeled off the PDMS mold. The solid polymer patterns (replica) are left behind. Due to the low surface energy (21.6 dyn/cm) of PDMS, the replica is easily separated from the mold.
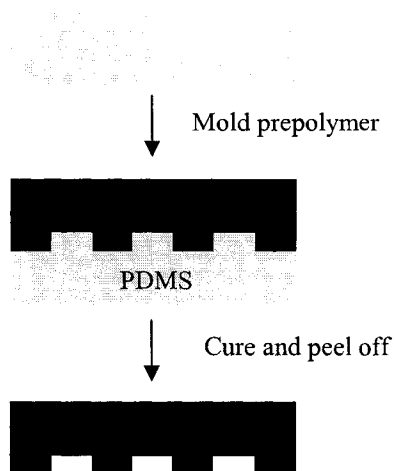
Figure 1.6 Procedure of REM.

The procedure of μTM (Fig. 1.7) is as follows: the prepolymer solution is dropped on a PDMS mold. The excess solution is wiped by scraping with a razor blade. The filled PDMS mold is then placed on a substrate and cured via heating. The mold is peeled away, and the polymer patterns are left on the substrate. The most significant advantage of μTM is that it can fabricate microstructures on both planar and nonplanar contoured surfaces.

prepolymer

PDMS

Remove excess
prepolymer

PDMS

Place on the support

PDMS

Cure and peel off

Residual film
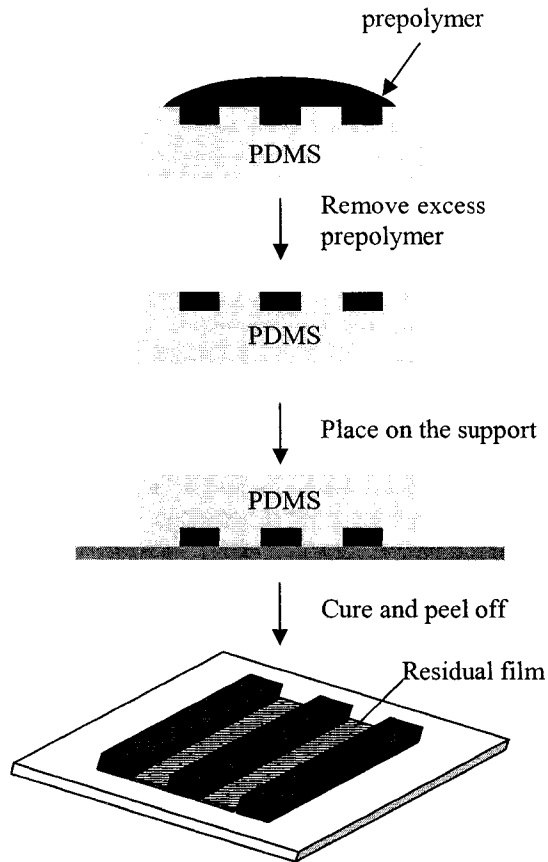
Figure 1.7 Procedure of μTM.

MIMIC (Fig. 1.8) process can also be applied to both planar and curved surfaces. In MIMIC, patterned PDMS mold is placed on a substrate. The relief structure in the mold and the substrate form a network of empty channels with at least two open ends. Low-viscosity liquid prepolymer is next dropped at one open end of the channels. The liquid fills into the channels due to capillary action and then is cured into a solid state. The PDMS mold is peeled away and the network of polymer is left on the substrate. MIMIC can be used to manufacture complex structure. However, the low production efficient which results from the slow filling speed limits the application of MIMIC.

PDMS mold

Support

Place a drop of prepolymer at one end

Fill channels by capillary action

Cure and peel off
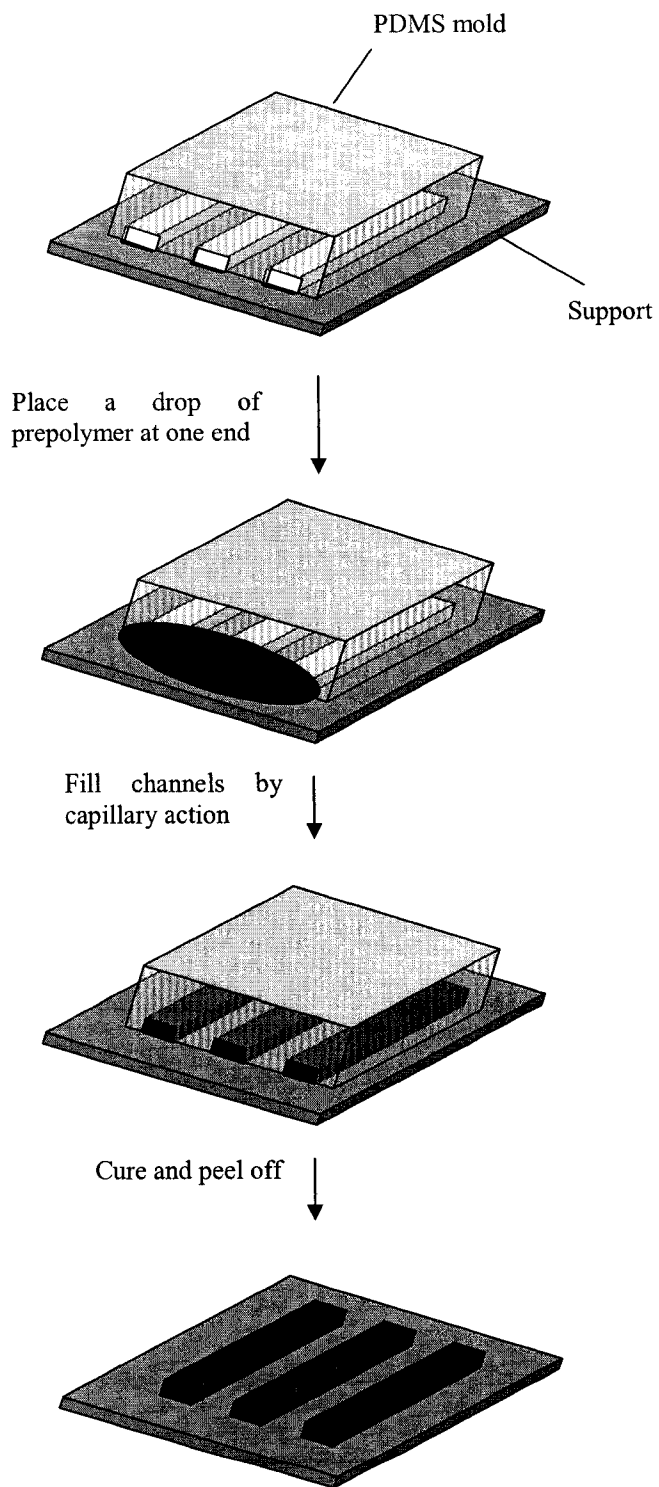
Figure 1.8 Procedure of MIMIC.

In SAMIM (Fig. 1.9), a PDMS mold is wetted with solvent and then brought into contact with the surface of a polymer, which is coated on a substrate. The solvent dissolves the polymer so the PDMS mold can emboss into the subatrate. After heating to remove the solvent and peeling away the mold, polymeric patterns remain on the substrate.
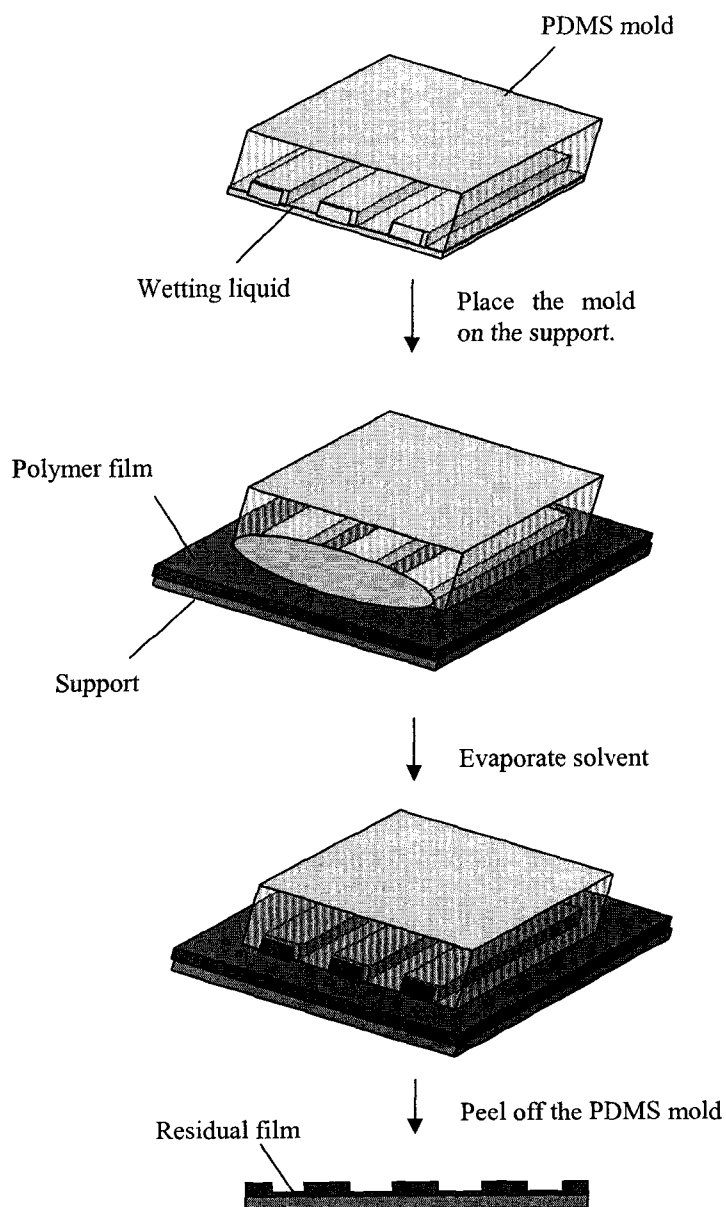
Figure 1.9 Procedure of SAMIM.

The utility of soft lithographic techniques is often limited by PDMS mold. The

PDMS mold has several technical problems, such as pairing, sagging, and shrinking (Fig.

1.10).
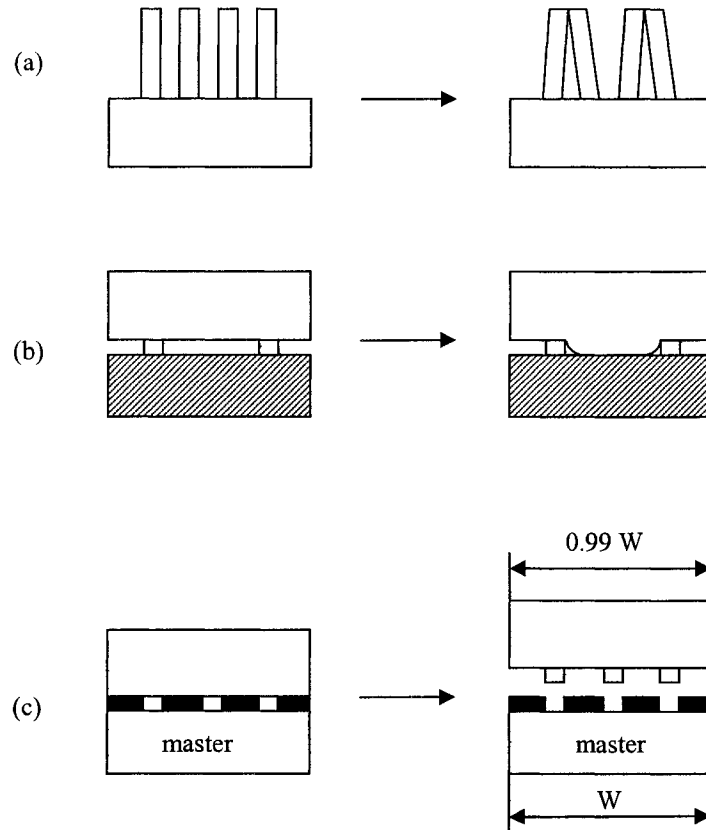
Figure 1.10 Schematic illustration of problems of PDMS mold in soft lithography: (a) pairing, (b) sagging, and (c) shrinking.

1.2.3 Hot Embossing and Nanoimprinting

Hot embossing lithography (and nanoimprint lithography) is a technique for the

fabrication of micro/nano structures on large surfaces. It is not a novel technique. Since

Chou and co-workers [15-17] expanded it to nano-scale, more and more researchers have

been attracted to this field due to its advantages of high reliability, large throughout, and

low cost. The hot embossing method is based on thermo-plastic polymers, such as

polymethylmethacrylate (PMMA) and polycarbonate (PC), and molding with common

pattern transfer methods. Once a stamp with a convex structure is fabricated, it can be used for the replication of thermo-plastic polymer patterns on a substrate surface. Therefore, its resolution is no longer limited by the wavelength of light, which is its dominant advantage over a photolithographic approach.

In the standard hot embossing lithography (Fig. 1.11a), first a layer of thermal-plastic polymer material (often PMMA) is coated on a substrate. Then the polymer is heated above its glass transition temperature (i.e., T_g), thereby decreasing the polymer viscosity for the imprinting process. A stamp (or mold) with relief structure, which is usually made from silicon or nickel, is forced to imprint (insert) into the soften polymer layer. As force is applied, the material begins to flow into the relief structures (i.e cavities or channels) of the stamp, initially flowing across the boundary of the tool features. The stamp is held for a sufficient time to allow the polymer material to flow into the cavities of the stamp. After cooling and separation of the stamp, re-solidified polymer is patterned with unwanted residue. Figure 1.12 shows the time history of temperature and applied force. After hot embossing, metal or conducting polymer is coated, and the lift-off process is then carried out. The final patterns remain on the substrate.

Thermo-plastic polymers can be patterned directly by a hot embossing process (Fig. 1.11b) to fabricate accelerometers [18], micro lens [19,20], waveguides [21], micro fluid system [22,23] and bioMEMS [24]. However, no research suggests that metals or conducting polymers can be patterned directly using the hot embossing process.

(a) Combined with lift-off   (b) Without lift-off

Coat thermo-plastic polymer   Coat conducting polymer

Insert mold into the polymer   Insert mold into the polymer

Cool down and release the mold   Cool down and release the mold

Apply RIE to remove residue   Apply RIE to remove residue

Coat metal or conducting polymer

Apply lift-off
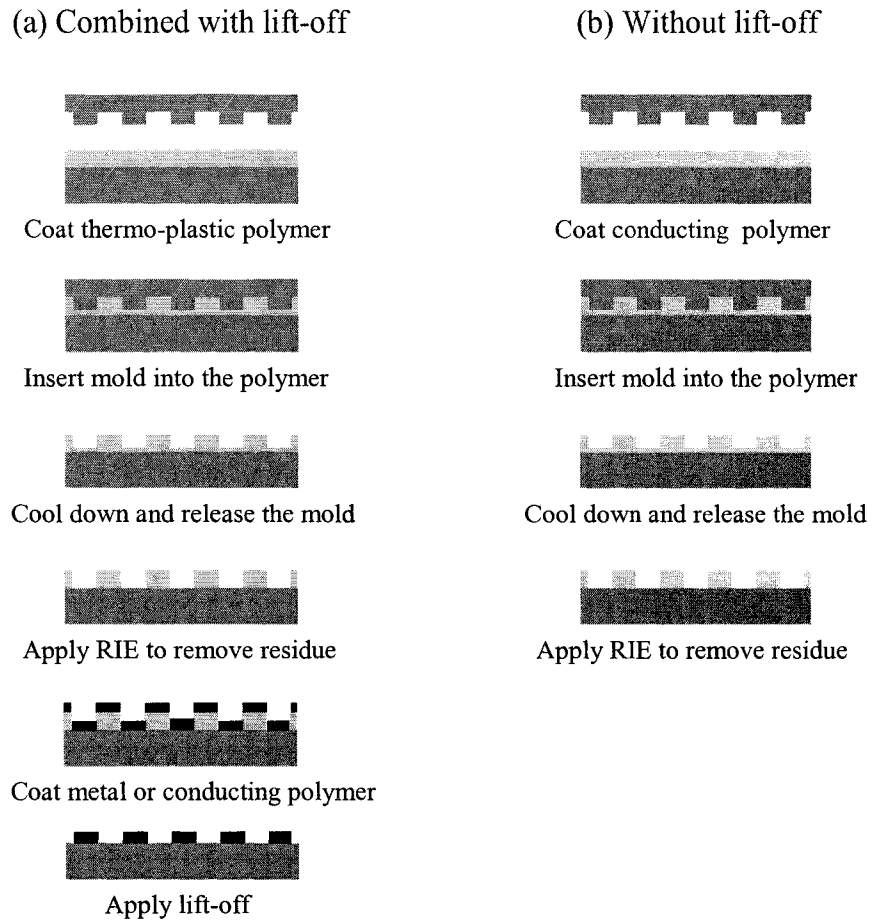
Figure 1.11 (a) Procedures of hot embossing technique to pattern metal or conducting polymer. (b) Direct hot embossing technique to fabricate polymer-based devices.
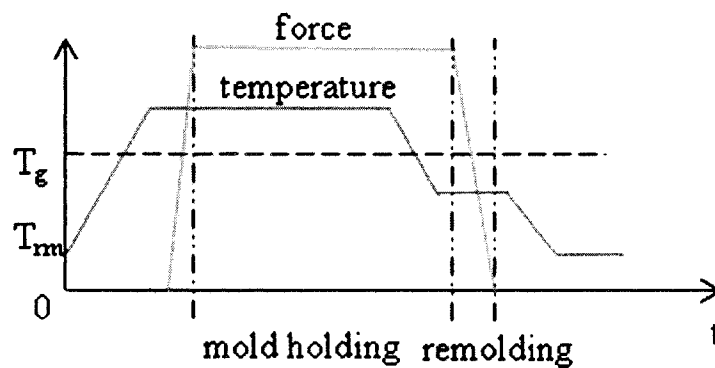
Figure 1.12 Hot embossing chart.

1.2.4 Summary

Traditional photolithography pattern methods were discussed first in this section. Photolithography is most widely used in IC and MEMS because of its exact controlled shape and dimensions of features. However, the minimum feature size of the traditional lithography approach is around 300 – 400 nm, which is limited by wavelength of light and sensitivity of photoresist. Moreover, these methods involve aggressive chemicals, organic solvents, light, or moisture, and they may affect human health, pollute the environment and degrade devices. Therefore, a new pattern technique is needed to solve these problems. Non-traditional (i.e., non-photolithographic) patterning methods are also presented in the previous sections. Soft lithography has been successfully used to fabricate both metal and conducting polymer patterns. The technique is free of harmful radiations and other chemicals that might alter the properties of the conducting polymer. However, the problems (e.g., pairing, sagging and shrinking), which result from soft stamp, may cause dislocations of patterns or variations of dimensions. Hot embossing process has low cost, high throughout, and high reliability. Also, no chemical etchant or light is involved in this process. On the other hand, it cannot be used to pattern metal or conducting polymer directly. The other non-traditional patterning methods, such as injection molding, cast molding, laser ablation, e-beam lithography, ink-jet printing, etc. [11], are restrained by high temperature, high energy beam, and/or low throughout.

In this work, stimulated by a macrocutting process commonly used in the metal manufacturing industry to create macropatterns in a sheet metal, the ILL approach is developed to generate metal or conducting polymer. The patterning process of the ILL

has the distinctive advantage of simplicity and is free of aggressive chemistry, high temperature and high energy beam. It is capable of massive production and nano patterns.

1.3 Macrocutting in Sheet Metal Process

For over a hundred years, a macrocutting process has been used to cut off macropatterns in sheet metal (i.e., a thin metal plate) in the manufacturing industry [25]. A hard punch and a rigid die of the desired convex and concave macropatterns, respectively, are adopted in this process. The concave macropatterns in the die are slightly wider than the corresponding convex mold structures in the macrocutting process, so that the convex mold structures can properly enter those concave patterns. The macrocutting process includes three basic steps (Fig. 1.13a). First, a sheet metal is placed on the rigid die. Second, the punch and the substrate are brought into physical contact by a high force. The insertion of the punch into the die may create deformations and stresses on the sheet metal. The maximum stress on the sheet metal happens just underneath the edges of the punch. During this step, when the maximum stress exceeds the break strength of the metal, part of the metal plate right underneath convex mold structures is cut off from the neighboring metal by the punch and dropped down to the bottom of the concave patterns in the die (Fig. 1.13b). Finally, the punch and the die are seperated, and the patterned sheet metal is removed from the die (Fig. 1.13c).
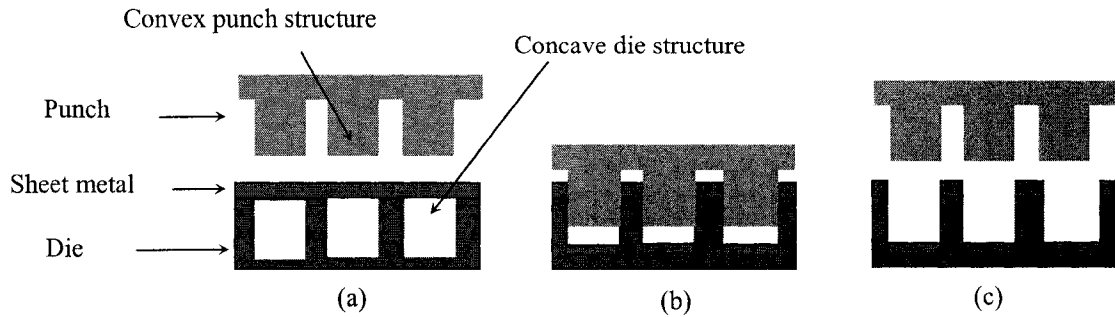
Figure 1.13 The three-step procedure to create macropatterns in sheet metal using the macrocutting process (cross-section schematics): (a) place sheet metal on the top of the die, (b) insert the punch into the die, and (c) separate the punch and the die.

Cutting metal by punching utilizes failure in shear; therefore, the cutting forces and the energy required are functions of the shear strength of the material [26]. Figure 1.14 shows a schematic illustration of how the metal is sheared between the cutting edges of the punch and the die.
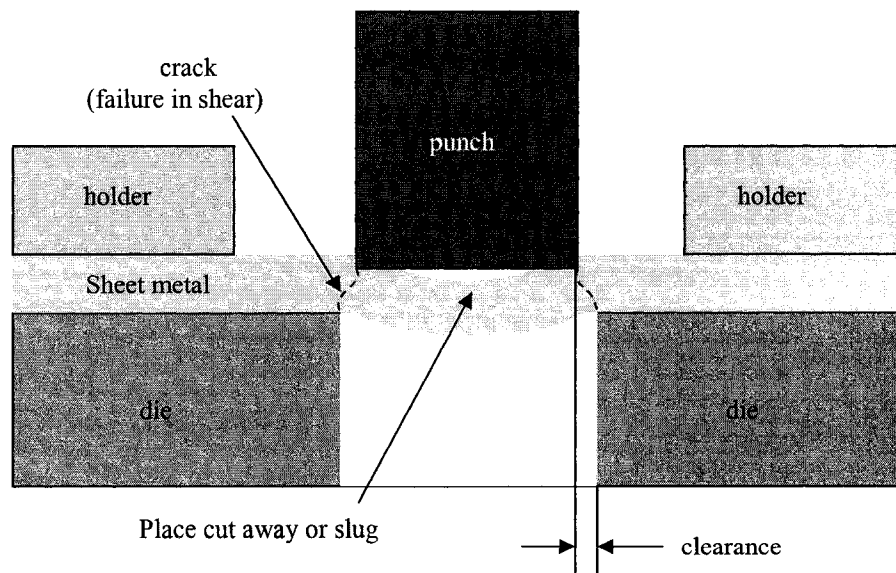
Figure 1.14 Schematic illustration of principle of punching sheet metal.

1.4 Objective of the Research

Stimulated by the macrocutting process, the ILL method has been developed to produce micropatterns in a thin metal or conducting polymer film based on a hot embossing technique. A silicon mold with the desired features is adopted in this method. The procedure of applying the ILL to pattern a metal is as follows (Fig. 1.14): (i) a silicon substrate coated with a layer of PMMA and a layer of a metal are heated up to $120 - 160°$ C, which is above the glass transition temperature (T_g; softening temperature) of PMMA (i.e., $105°$ C) and far below the melting temperature (T_m) of the metal (e.g., T_m of Al is $660°$ C) (Fig. 1.15a); (ii) the mold and the substrate are brought into physical contact by high pressure, followed by subsequent cooling (Fig. 1.15b); finally, (iii) they are separated when their temperature is below T_g of the PMMA, completing the pattern transfer from the mold to the metal layer (Fig. 1.15c). Molding in the ILL occurs in both the PMMA and metal layers. The metal right underneath a convex mold structure is first cut off from the neighboring metal at the beginning of the mold insertion and then pushed down to the bottom of the formed PMMA pattern (Fig. 1.15b). The cutting is due to the shearing forces at these edges caused by the mold insertion. Because of the interface bonding force, the PMMA at the interface of the PMMA and the cut-off metal move down together with the cut-off metal.
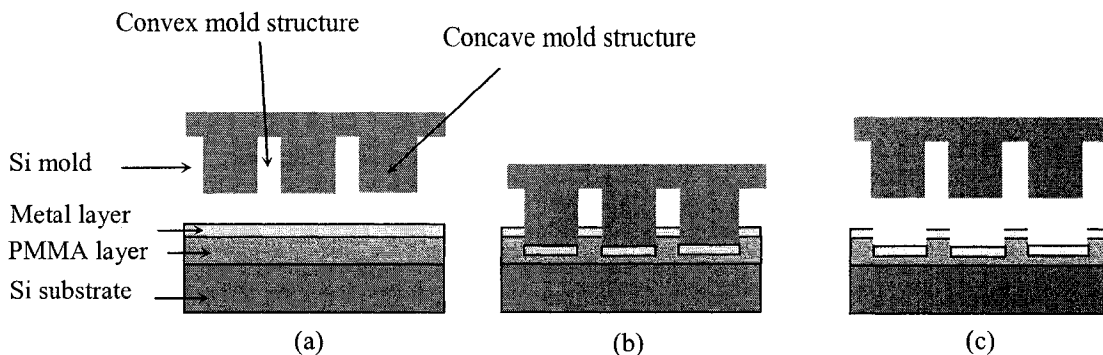
Figure 1.15 The three-step procedure to fabricate metal micropatterns using the ILL method (cross-section schematics): (a) heating of the substrate, (b) insertion of the mold into both the metal film and the PMMA layer on the substrate, and (c) separation of the mold and the substrate.

Like the macrocutting process, the ILL method makes use of the cutting principle to create metal patterns. Unlike the macrocutting, the substrate in the ILL does not involve concave structures. Instead, an intermediate layer of PMMA is introduced to assist the cutting, which avoids the experimental efforts and time needed in fabricating the concave structures. Furthermore, the macrocutting occurs at room temperature, while relatively high temperature is needed in the ILL to soften the PMMA so that the cut-off metal can be pushed inside the PMMA and separated from the uncut metal.

In the macrocutting process, a metal plate is supported by a rigid die and fixed by hard holders. Therefore, the metal plate has negligible slide on the die surface. During the insertion of the punch into the die, the metal plate deforms due to the pushing of the punch. As illustrated in Fig. 1.16, the part of the metal in the gap between the punch and the die experiences both elastic and plastic deformations before it finally breaks [3,25]. The part of the metal right underneath the punch also has elastic and plastic deformations while it does not break, since the experienced pressure is normally smaller than the break strength. The same applies for the part of the metal sandwiched between the rigid die and

holders. Also, this part of the metal does not move along the vertical direction due to the constraints of both the rigid die and the rigid holders. The ILL method does not adopt any rigid holders. Therefore, the part of the metal between two neighboring convex mold structures is only constrained by the PMMA layer underneath, so it has freedom to move up. As the PMMA layer is softened at the printing temperature, this part of the metal moves up, and together with the PMMA, fills the mold cavities between the neighboring convex mold structures (Fig. 1.17). Similar to what occurs in the macrocutting, the metal right underneath the convex mold structures may have elastic and plastic deformations while the metal does not break. On the other hand, stress concentrations occur at the edges of this part of the metal, cutting off this part of the metal from the neighboring metal, as these concentrated stresses are larger than the break strength of the metal. The portion of the metal at these edges should have both elastic and plastic deformations before the break happens.
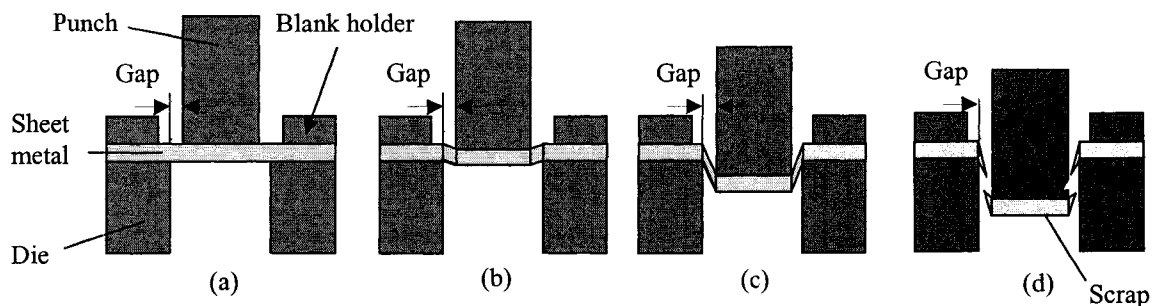
Figure 1.16 The deformation phases of a macrocutting process in patterning a sheet metal: (a) initial contact of the punch with the sheet metal, (b) elastic deformations, (c) plastic deformations, and (d) fracture and abruption.
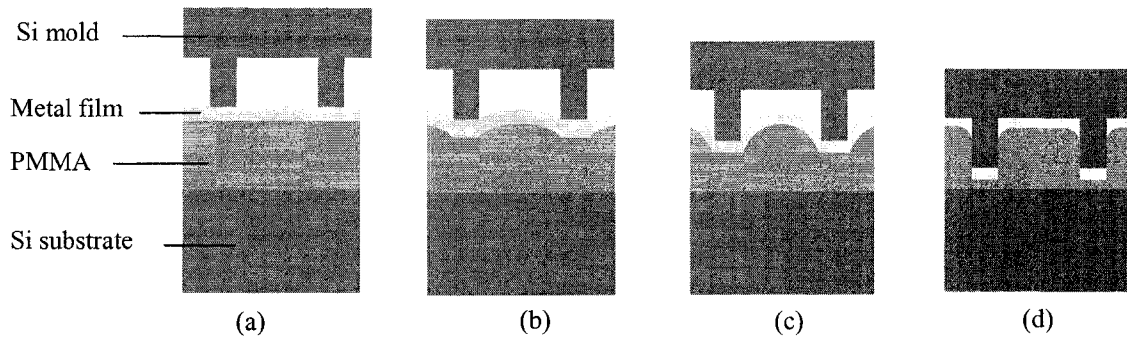
Figure 1.17 The deformation phases of a metal film in the ILL: (a) initial contact of Si mold with the metal film, (b) elastic deformation, (c) plastic deformation, and (d) fracture and abruption.

Finally, during the patterning process, the PMMA underneath the concave mold structures is not punched and has freedom to move into the concave mold structures. It should not have much residual stress. Accordingly, the quality of the metal patterns located on top of this part of the PMMA should not be affected by the potential residual stress in the PMMA. On the other hand, the PMMA underneath the convex mold structures is directly punched and should have residual stress, affecting the metal located on top of it. Since this part of metal is unwanted, it does not have to be concerned with its quality.

1.5 Difference Between ILL Method and Punching

Although the ILL method is stimulated from punching (sheet metal), the two techniques are quite different. Hard die is a critical component in the punching process, while a layer of soft, rubber-like polymer is substituted in the ILL. Correspondingly, concave die structures are in the punching process and a piece of flat smooth polymer in the ILL. The punching process operates at room temperature, while samples need to be heated to $120 - 160°$ C in the ILL.

1.6 Difference Between ILL Method and Hot Embossing

There are two critical differences between a commonly used hot embossing process and the ILL method. First, the substrate in the hot embossing process has only the layer of the thermoplastic material to be imprinted, while the substrate in the ILL approach involves a layer of a thermoplastic material and a layer of a metal or conducting polymer. Second, the hot embossing technique aims at creating a thickness contrast in the thermoplastic material, but the ILL approach makes use of the thermoplastic material to cut off the metal or conducting polymer.

1.7 Dissertation Outline

The outline of this dissertation is as follows. The ILL is introduced in Chapter 1. The research needs and related research are presented in Chapter 2 and 3, respectively. The principle of numerical simulation of this method is given in Chapter 4. In Chapter 5, detailed experimental procedures to generate metal micropatterns and corresponding results analysis are described. In Chapter 6, conducting polymer-based devices are fabricated and characterized. The fabrication of metal nanopatterns using ILL method is introduced in Chapter 7. Some methods to extend the lifetime of Si molds are presented in Chapter 8. Finally, this work is concluded in Chapter 9.

CHAPTER 2

RESEARCH NEEDS

2.1 Experiment Facilities

2.1.1 Fabrication Facilities

- Clean room

- Hot embossing machine

- Deep reactive ion etching (DRIE) system

- Spinner

- Thermal evaporator

- Reactive ion etching (RIE) system

- Hot plate

2.1.2 Measurement Equipments

- Optical microscope

- Scan electron microscope (SEM)

- Atomic force microscope (AFM)

24

- Surface profiler

2.1.3 Assist Tools

- Wafer boxes

- Tweezzers

- Wipers

- Diamond cutter

- Multimeter

- Timer

2.2 Experiment Materials

2.2.1 Basic Materials

- Si wafer

- PMMA

- Al source for thermal evaporated

- Au source for thermal evaporated

- PEDOT

- PPy

2.2.2 Other Materials

- Acetone

- DI water

- Photoresist 1813

- Developer MF319

- Buffered oxide etch (BOE) solution

- Liquid N_2

- Gases: O_2, N_2, SF_6 and C_4F_8

CHAPTER 3

RELATED TECHNIQUES

3.1 Hot embossing

Hot embossing is the major technique in the ILL method. A detailed description was given in Section 1.2.5.

3.2 DRIE

Si mold in this work is fabricated using the deep reactive ion etching (DRIE) approach. DRIE is developed from the reactive ion etching (RIE) technique. In RIE, neutral reactive gases are excited to plasma by an electric field or radio frequency (RF). The plasma is a collection of electrons, singly and multiply charged positive and negative ions, neutral atoms, molecules, and molecular fragments [1]. There are two interactions in RIE: physical interaction and chemical interaction. Physical interaction occurs through surface bombardment by energetic ions, and chemical interaction occurs through standard electronic bonding processes.

An additional electric field is applied in RIE to accelerate ions towards the surface to be etched, which increases the extent of anisotropy and depth of the etched feature, as compared to conventional RIE. Hence, it is so-called DRIE. In order to gain high-aspect-

27

ratio features, etchant (e.g., SF_6) and protector (e.g., C_4F_8) is applied to Si surface alternatively. Figure 3.1 shows the schematic illustration of the process flow of DRIE. The cycle begins with isotropic etching of the silicon with SF_6 (Fig. 3.1a). Then, SF_6 is switched off, and C_4F_8 is used to deposit a fluorinated polymer coating on both the trench bottom and the sidewalls (Fig. 3.1b). At the end of the cycle, C_4F_8 is switched off and SF_6 is switched on again. SF_6 etches the protective polymer off the trench bottom faster than the sidewalls (Fig. 3.1c). Thus, the silicon is etched on the trench bottom while the sidewalls are protected by the polymer. The protective sidewall polymer layer is eventually etched away, and the process switches back to the deposition step, and the entire process is repeated [27].

(a) Si is etched by SF$_6$ plasma.

(b) C$_4$F$_8$ is deposited on the Si surface.

(c) Protective deposition layers on the horizontal surfaces are bombed away and Si is etched by SF$_6$ plasma.
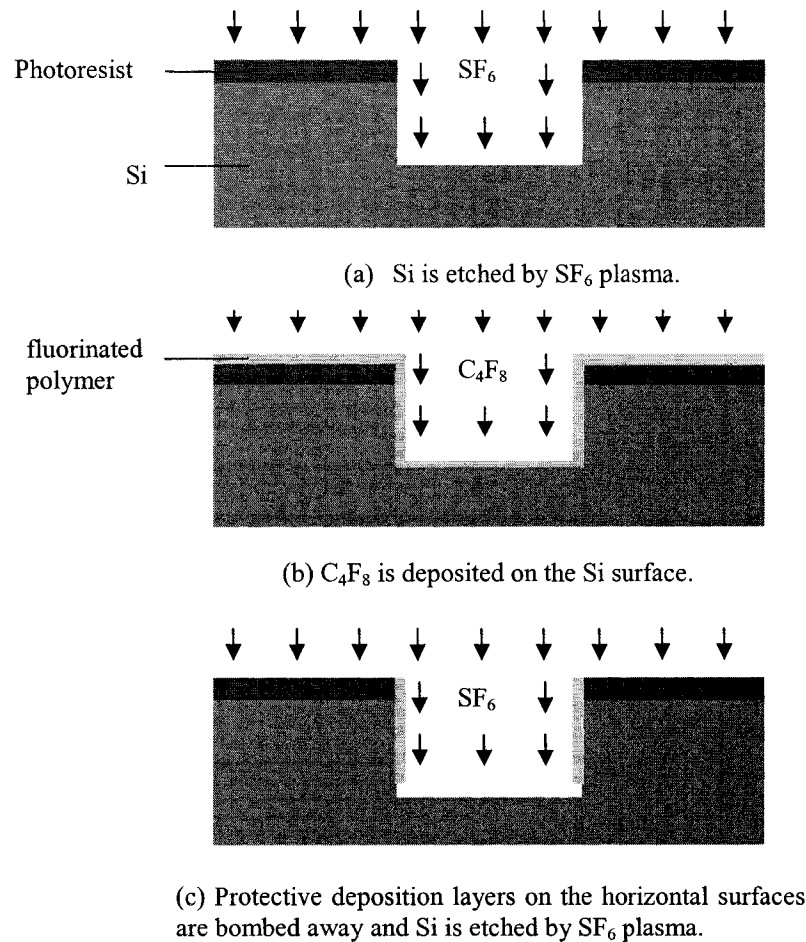
Figure 3.1 Schematic illustration of process flow of DRIE.

3.3 Vacuum Thermal Evaporation

In this work, aluminum and gold are used to fabricate metal patterns using the ILL method. Al and Au are deposited on a PMMA sheet via vacuum thermal evaporation, which is a kind of PVD process.

The vacuum thermal evaporation deposition technique starts with the heating and evaporation of the target material (e.g., Al or Au in this work) to be deposited. The material vapor finally condenses in the form of a thin film on the cold substrate surface. In order to avoid reaction between the vapor and atmosphere, evaporation is usually

carried out at low pressures, which range from 10^{-6} to 10^{-5} Torr. At these low pressures, the vapor atoms travel in straight lines from the evaporation source towards the substrate.

In thermal evaporation techniques, different methods can be applied to heat the material. The equipment available in the laboratory use either resistance heating (Joule effect) or bombardment with a high energy electron beam, usually several KeV, from an electron beam gun (electron beam heating). Resistance heating is simple and low cost. Compared to resistance heating, e-beam heating generates uniform deposition film without thermal deformation.

3.4 SEM

The scanning electron microscope (SEM) (Fig. 3.2) generates a beam of electrons from a (Tungsten, LaB_6 or field emission guns) filament in a vacuum chamber. The beam is collimated by electromagnetic condense lenses, focused by an objective lens, and scanned across the surface of the sample by electromagnetic deflection coils. The primary imaging method is accomplished by collecting secondary electrons that are released by the sample. The secondary electrons are detected by a scintillation material that produces flashes of light from the electrons. The light flashes are then detected and amplified by a photomultiplier tube.

Scanning electron microscope (SEM) uses accelerated electrons to replace visible light in optical microscopes. Optical microscopes have their resolution limited by the diffraction of light. Visible light has wavelengths from 400 to 700 nanometers, while electrons accelerated to 10,000 KeV have a wavelength of 0.12 Angstroms. Hence, the

scanning electron microscope breaks through the resolution limitation of optical microscopy. Moreover, the large depth of field of SEM images gives them a 3D effect.

SEM requires a conductive surface of the sample and vacuum chamber. Those disadvantages limit the application of SEM.
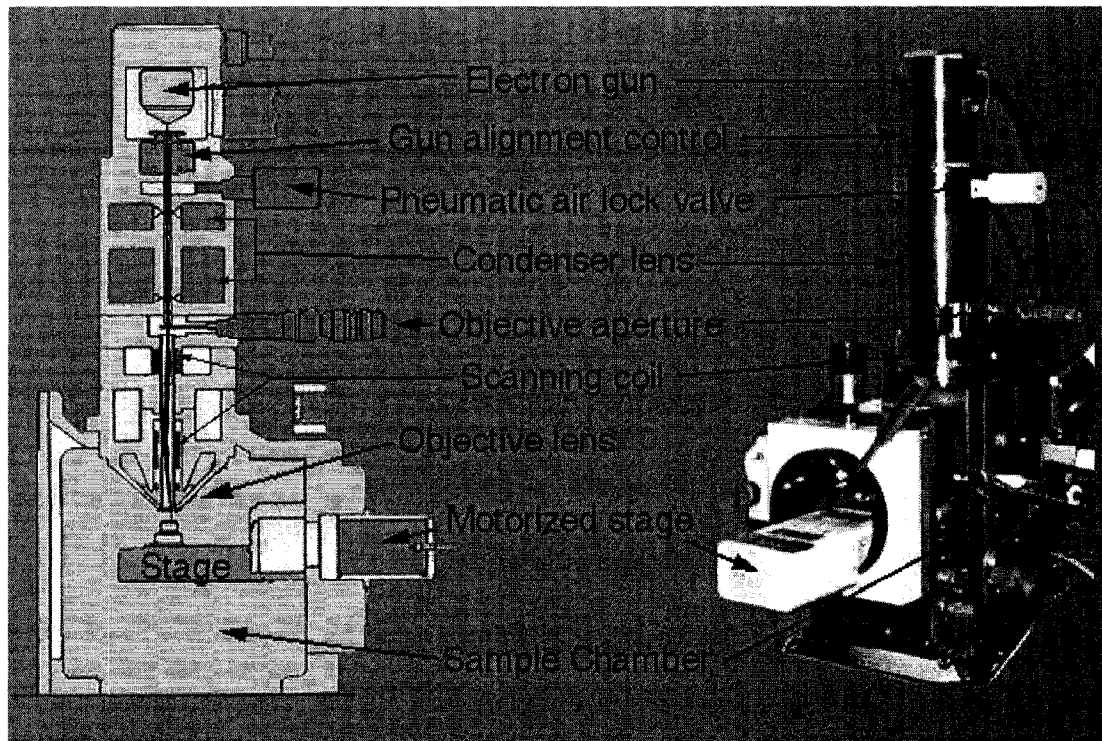
Figure 3.2 The schematic illustration of structure of SEM [28].

3.5 AFM

Atomic force microscope (AFM) provides pictures of atoms on surfaces. AFM utilizes a tip on the end of a cantilever, which bends in response to the force between the tip and the sample, moving over the surface of a sample in a raster scan. Figure 3.3 illustrates how this works: as the cantilever flexes, the light from the laser is reflected onto the split photo-diode. By measuring the difference signal, changes in the bending of

the cantilever can be measured. Since the cantilever obeys Hooke's Law for small displacements, the interaction force between the tip and the sample can be found. The movement of the tip or sample is performed by an extremely precise positioning device made from piezoelectric ceramics, most often in the form of a tube scanner. The scanner is capable of sub-angstrom resolution in x-, y-, and z-directions. The z-axis is conventionally perpendicular to the sample.

AFM has high resolution. Both nonconductive and conductive samples can be inspected in AFM, so it can be used in soft material and biomaterials. AFM is carried out in atmosphere, even in fluid. However, AFM has a small height range of measurement and slow scan rate, compared to SEM.
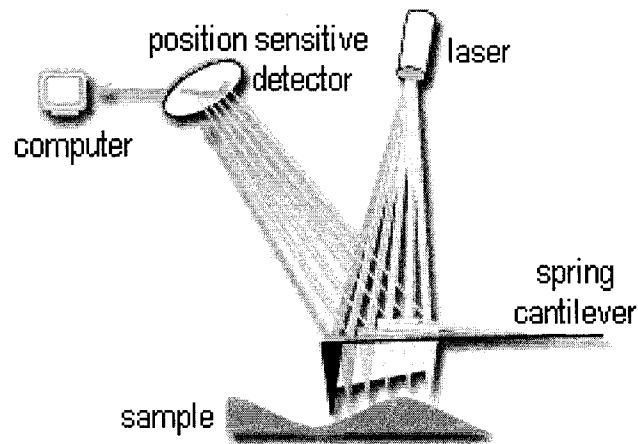
Figure 3.3 The schematic illustration of principle of AFM [29].

CHAPTER 4

NUMERICAL CONDUCTION

Numerical simulation was conducted in this work for a better understanding of experimental results, which will be discussed in Chapter 5, 6, and 7. Two methods have been used by researchers to study large deformations of a polymer during a hot embossing process as the imprinting temperature is above its T_g. Rowland et al. [30,31], Jeong et al. [32], and Worgull et al. [33] considered the polymer as a viscous Newtonian flow under viscous dominant conditions, and used commercial computational fluid dynamics codes GOMA [30,31], CFDACE [32] and Moldflow [33], for the corresponding simulation. Hirai et al. [34,35] treated the polymer as a nonlinear elastic solid material characterized by a Moony-Rivlin constitutive relationship, and employed a commercial package MARC [34,35] in the numerical calculation. These researchers considered the filling behaviors of polymers under different geometry conditions and showed that both the liquid and solid models could address some deformation characters during the hot embossing. These simulation results provide a good understanding about the polymer deformations during the molding process. On the other hand, they could not be used to quantitatively describe the deformation behaviors due to the following concerns. The PMMA is first heated up and then cooled down during the molding process, while the Mooney-Rivlin relationship does not describe the corresponding

33

thermal effects. Also, the cross-section profile produced during the molding cannot be fully recovered, which is the characteristic of a plastic deformation. Therefore, the PMMA should be better modeled as a thermo-plastic material during the molding process, which is also our case. However, to the best of our knowledge, such a thermo-plastic model has not yet been established.

In this work, in order to have a good understanding about the ILL and interpret some interesting experimental phenomena observed, the second method was adopted to consider the case when the PMMA was coated with a thin Al film. That is, the PMMA was modeled as a nonlinear rubber-like, hyperelastic solid following the Moony-Rivlin constitutive relationship. The form of the strain energy potential of this relationship is [36]:

$$\sigma_i = \lambda_i \frac{\partial W}{\partial \lambda_i}, \tag{4.1}$$

where λ is the expansion rate and W is a strain density function. W is expressed as

$$W = C_{10}(I_1 - 3) + C_{01}(I_2 - 3) + \frac{1}{d}(J - 1)^2, \tag{4.2}$$

where $I_1 = \lambda_1^2 + \lambda_2^2 + \lambda_3^2$, $I_2 = \lambda_1^2 \lambda_2^2 + \lambda_2^2 \lambda_3^2 + \lambda_3^2 \lambda_1^2$, $I1$ is the first deviatoric strain invariant, $I2$ the second deviatoric strain invariant, C_{10} and C_{01} material constants characterizing the deviatoric deformation of the material, and d the material incompressibility parameter. The initial shear modulus is defined as $\mu = 2(C_{01} + C_{10})$, and the initial bulk modulus is defined as $k = \frac{2}{d}$. C_{10} and C_{01} are the 1st and the 2nd strain energy constrains, respectively. They are derived from the following approximated relations [36]:

$$C_{01} = 0.25C_{10}$$
(4.3)

$$6(C_{10} + C_{01}) \approx E$$
(4.4)

where E is the Young's modulus of the polymer. From Equation (4.3) and (4.4),

$$C_{01} = 0.034 E$$
(4.5)

$$C_{10} = 0.134 E .$$
(4.6)

Due to the nonlinear terms in Equation (4.2), it is difficult to find an analytical solution. Therefore, numerical simulation is needed to find the residual deformation. Since the finite-element software ANSYS 8.0 allows the simulation of a material using the Moony-Rivlin stress-strain relationship, it was chosen in this work to establish the simulation model. The deformation of PMMA should mainly happen in the area around the mold insertion. In Fig. 4.1, the Si mold depth was 15 μm. For simplicity, the thickness of PMMA was set as 50 μm instead of 500 μm. Al was simulated as a hyperelastic solid. Silicon is a hard material. Its Young's modulus is high, about 170 GPa, which is much higher than those of PMMA and Al. Hence, silicon mold was considered as a rigid solid (i.e., did not experience any deformations) in the simulation. As such, the thickness of the bottom mold layer (i.e., the layer on which the mold structures were located) should not affect the molding results in the simulation. Consequently, to save computational time, this bottom mold layer was simulated as a 10-μm-thick layer (Fig. 4.1), although its real thickness was around 470 μm. The silicon mold structures were set to be the real dimensions. The basic material properties used in the simulation are given in Table 4.1. Due to geometric symmetry, only part of the mold structures and their insertion were considered in the simulation. As shown in Fig. 4.2, the

simulated Si model structure had a concave mold structure and two half convex

structures. The filling course of Al and softened PMMA into a Si channel is as follows:

(a) before the Al film breaks, the part of Al underneath the Si channel curves up (Fig.

4.2a); (b) after the Al film breaks, the part of Al in the channel is pushed deeper inside

the Si channel by PMMA and suffers larger deformations (Fig. 4.2b); and (c) the final

configuration of Al and PMMA is defined by the cross-section profile of the Si channel

after PMMA completely fills the channel (Fig. 4.2c).
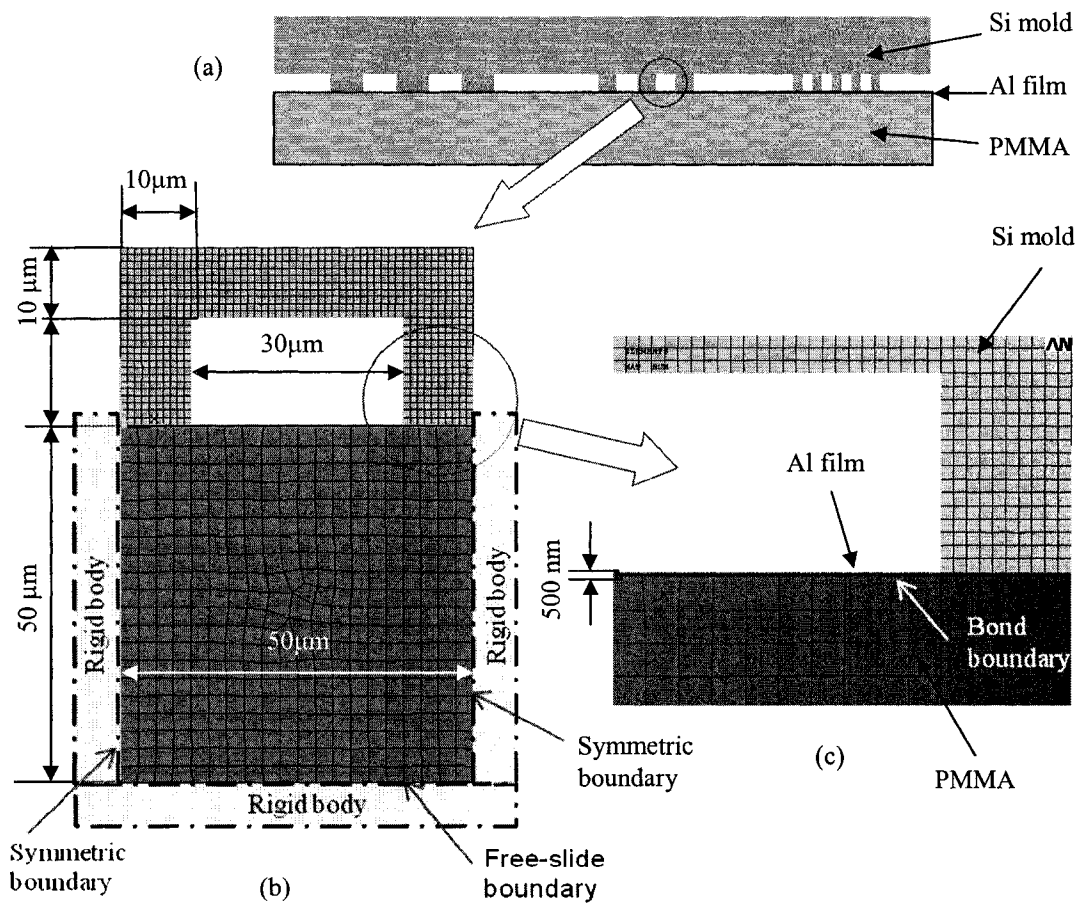
Figure 4.1 (a) The schematic set-up of the ILL, (b) the portion that was picked up for simulation, and (c) a close-up view of a channel corner.

(a)   (b)   (c)
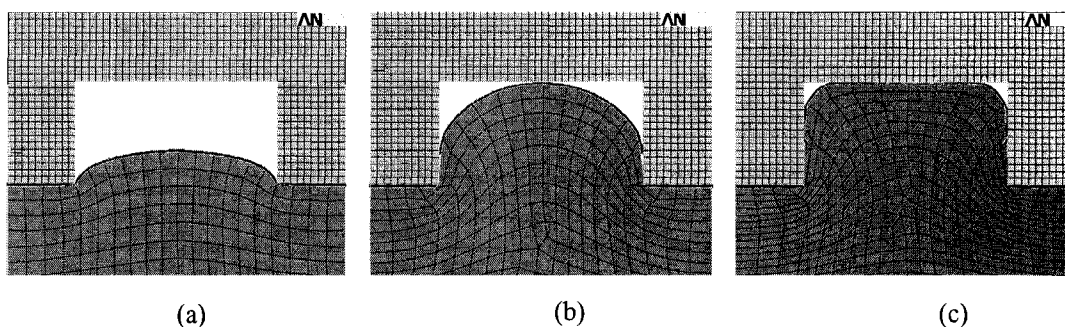
Figure 4.2 The filling of Al and softened PMMA into a Si channel: (a) before the Al film breaks, the part of Al underneath the Si channel curves up; (b) after the Al film breaks, the part of Al in the channel is pushed deeper inside the Si channel by PMMA and suffers larger deformations; and (c) the final configuration of Al and PMMA is defined by the cross-section profile of the Si channel after PMMA completely fills the channel.

Table 4.1 Material properties of PMMA, aluminum, and silicon for simulation

Properties	PMMA	Aluminum	Silicon
	Hyperelastic solid	Hyperelastic solid	Rigid solid
Young's modulus (GPa)	2.5 – 0.5	21	170
C_{10}	0.3325 - 0.0665	2.793	-----
C_{01}	0.0825 - 0.0165	0.693	-----
Poisson ratio	0.49	0.3	0.23
Density (Kg/m^3)	1.2×10^3	2.3×10^3	2.5×10^3

The PMMA did not have horizontal displacements at its left and right edges due to the deformation symmetry with respect to the other side of either edge. The PMMA bottom was fixed due to its contact with the rigid substrate. The Al film was bonded to the PMMA. Therefore, both the Al film and PMMA layer should have the same deformations at their interfaces. As the PMMA and Al get inside the Si concave mold structure, their movements might be affected by the friction forces on the sidewalls of the concave mold structure. The corresponding friction efficient was set to be 0.01.

Figure 4.3 shows stress distribution on the part of the Al underneath the convex mold structures before it is cut off from its neighbor. The maximum stress on the Al occurs just underneath the edges of the convex structures.
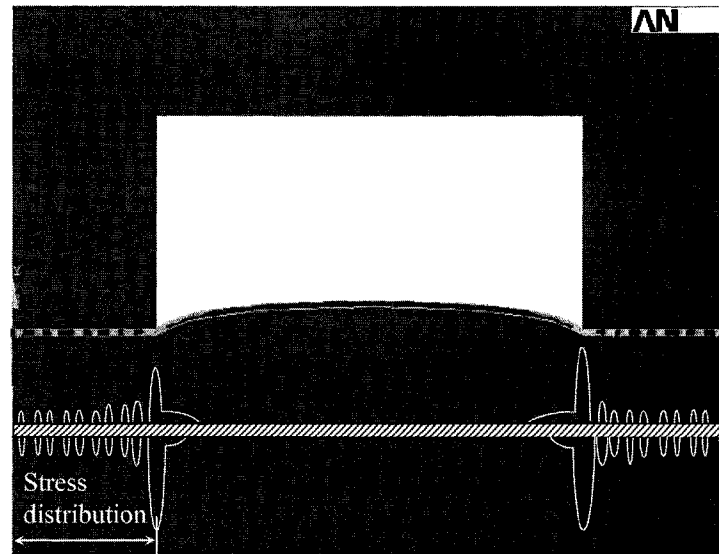
Figure 4.3 Stress distribution on the part of the Al underneath convex mold structures before it is cut off from its neighbor. The maximum stress on the Al occurs just underneath the edges of the convex structures.

CHAPTER 5

FABRICATION OF METAL MICROPATTERNS

5.1 Fabrication of Silicon Mold

Molds are very old tools to fabricate metal, plastic, rubber, or glass parts, such as coins, car bodies, tires, and wine bottles. Although it may be expensive to make a mold, the cost of the mold is assigned to every part in mass production. Furthermore, the usage of the mold cut short the whole fabrication procedure and made the product easy to be fabricated with low cost.

Two major kinds of mold widely used in hot embossing technique are nickel and silicon molds. Nickel mold is used in commercial processes, while silicon mold is used in laboratories [37].

In this work, silicon molds were selected to pattern metal film. They were fabricated using ultra-violet lithography and deep reactive ion etching (DRIE) as follows. A 1-μm-thick layer of a positive photoresist 1813 (Shipley Company) was spin-coated on a SiO_2-coated a 4-in silicon wafer (Fig. 5.1a). The photoresist was then patterned using ultra-violet light exposure, followed by development (Fig. 5.1b). Using the patterned photoresist as a masking layer, SiO_2 structures were created through wet etching using a Buffered Oxide Etch solution (BOE) (6 parts 40% NH_4F and 1 part 49% HF) (Fig. 5.1c).

39

Finally, silicon mold structures were produced via DRIE with the SiO_2 as a protective layer (Fig. 5.1d). The DRIE is a dry-etching technique which is commonly used in the MEMS area to produce deep and high-aspect-ratio trenches in silicon by alternating SF_6 plasma etch with C_4F_8 protective deposition [1,3]. In this work, the DRIE was conducted in an Alcatel 610E ICP machine. The flow rates of SF_6 and C_4F_8 were 300 standard cubic centimeters per minute (SCCM) for 7 seconds and 120 SCCM for 3 seconds, respectively. The silicon molds structures had depths of about 10, 20, 40, 60, 80, and 100 μm, respectively. Figure 5.2 shows pictures of the Si mold, which was fabricated using the previous method.

Photoresist

SiO_2

Si substrate

(a)

(b)

(c)

(d)
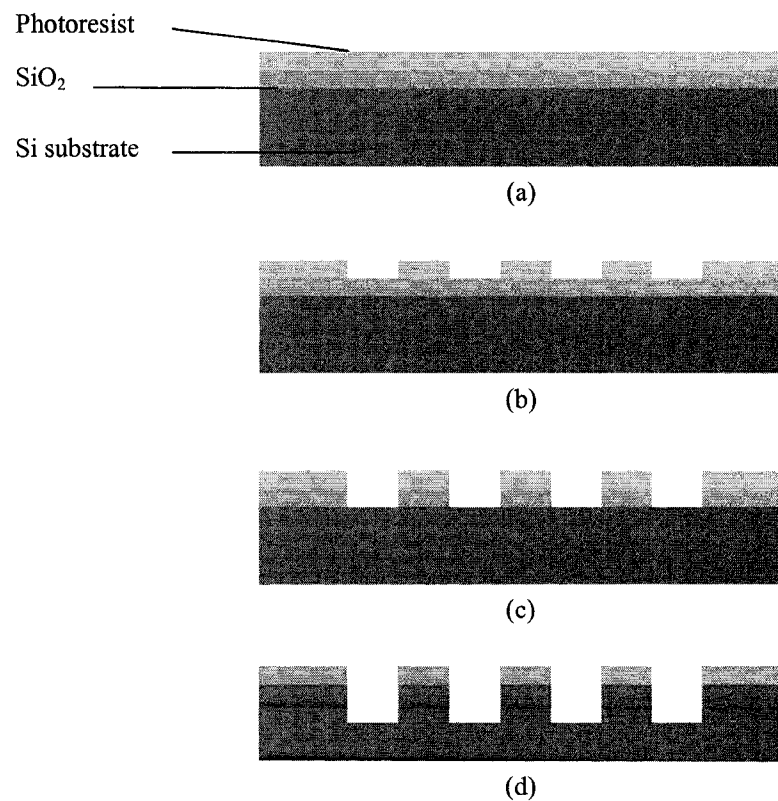
Figure 5.1 The schematic illustration of fabrication of Si mold.

(a)

(b)

(c)

(d)
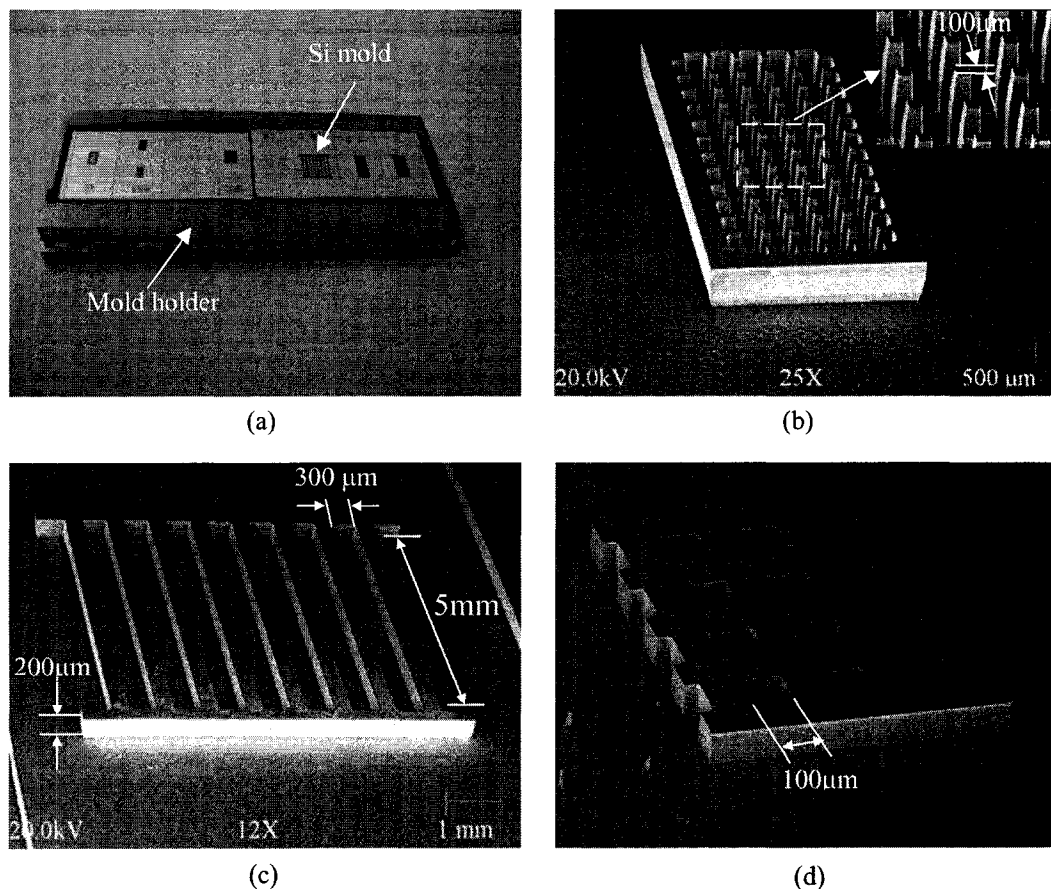
Figure 5.2 Si mold used in ILL method: (a) overview of Si mold and mold holder, (b) square dots with 100 μm width, (c) micro channels with 300 μm width and 5 mm length, and (d) square holes with 300 μm width.

5.2 The Procedure of ILL Method

Silicon molds were used to imprint metals. PMMA sheets (Cryo Company) were adopted as the intermediate layers. The sheets were 500 μm thick, 170 mm wide, and 170 mm long. PMMA was chosen as the intermediate layer material, since it was demonstrated as a good hot embossing material [15,16]. PMMA is a thermal-plastic polymer. Its T_g is about 105° C, and the imprinting temperature, which is used to fabricate metal micropatterns, is typically between 120 and 160° C. PMMA is an electrical insulator. The metal patterns (i.e., the part of the metal located directly

underneath the concave mold structures) would be separated from the part of the unwanted metal (i.e., the part of the metal located directly underneath the convex mold structures) by the PMMA. Due to the electrical insulation of the PMMA, there would be no shorting problems in electrical applications of the metal patterns. The ILL method was examined through the patterning of Al, a metal widely used in MEMS.

Thermal vacuum evaporation (DV-502A, Denton vacuum Company) was employed to form thin Al films on PMMA layers. These Al films, which were patterned in this work, had thicknesses of 100, 200, 300, 400, and 500 nm, respectively. Hot embossing process was performed in a commercial hot embossing system HEX 01/LT (JENOPTIK Mikrotechnik Company). This hot embossing system allows a good control of the key imprinting parameters, such as temperature, pressure, embossing environment, and molding and de-molding speeds. Using this machine, the substrate and the mold can be heated and regulated at a temperature up to 200° C with a precision of 0.1° C. In this work, the mold insertion speed used was 1 mm/min, the imprinting force was between 1,000 and 1,800 N, the mold was kept on the substrate for 5 – 10 min, the de-molding process was performed at 80 – 95° C with a speed of 1mm/min, and the imprinting temperature ranged from 120 to 160° C. Table 5.1 is a typical hot embossing recipe for ILL method.

Table 5.1 Hot embossing recipe and its explanation for micro patterns

Command	Explanation.
Initialize force control [true/false]=1	Basic force unit is initialized.
Temperature [Top=90 deg, Bottom=90 deg]	Starts heating of substrate and embossing tool.
Close Chamber []	Closes the vacuum chamber.
Evacuate Chamber []	Evacuates the vacuum chamber.

Wait time [time=20 s]	Wait.
Show chart window [Show/Hide=11/0]	Displays the graphical view of the parameter change.
Touch Force [Force=50 N]	The tool, when in contact with the substrate, applies an initial force of defined limit for efficient heat transfer.
Wait time [time=20 s]	Wait.
Heating [Top=130 deg, Bottom=130 deg]	Heats the tool and the substrate to the process temperature.
Temperature >= [Temperature=105 deg, Channel=10);	Heats until the temperature of the tool and the substrate assembly reach the desired temperature.
Wait time [time=10 s]	Wait.
Heating [Top=120 deg, Bottom=120 deg]	Heats the tool and the substrate to the process temperature.
Wait time [time=60 s]	Wait.
Position relative [position=0.15mm, velocity=10 mm/min]	Insert mold into PMMA with 0.15 mm distance.
Wait time [Time=500 s]	Sets the holding duration.
Cooling [Top=60 deg, Bottom=60 deg]	Starts cooling the substrate and the tool assembly.
Wait Time [Time=50 s]	Wait.
Temperature <= [Temperature=95 deg, channel=10]	System waits until the temperature falls down to 95° C.
Wait Time [Time=50 s]	Waits for the temperature to stabilize.
Demolding Adv [Stretch=1.5 mm, velocity = 1.0 mm/min]	Demolds tool and the substrate. Demolding takes place at a set speed.
Venting []	Vents the chamber.
Open chamber []	Opens the chamber.
Show chart window [Show/Hide = 01/0]	Hides the chart which displays the graphical view of the embossing parameters with respect to time.

5.3 Force Analysis During ILL Method

Actually, the mold insertion during ILL method can be considered a process in which the PMMA layer with metal film fills into a silicon channel. The force condition

on the metal film is different before and after the metal film is broken. Before broken, metal film is a whole unity (Fig. 5.3a). All the parts of it are pulled by their neighbors. The parts underneath the convex structures are held by the convex structures and the softened PMMA layer. They can not move horizontally. However, they can be pushed down directly by the convex structures. They give the pull forces to their neighbors, which are in the channels. Those parts would be pushed up by the softened PMMA layer because PMMA continues to fill into the empty channels. They are elongated due to the deformation of PMMA. Therefore, there are concentrated stress points just under the edges of the convex structures. The simulation result of the distribution of stresses (Fig. 5.4) proved the previous assumptions. When the concentrated stress exceeded the ultimate tensile strength of the metal material, the metal film was broken into pieces. The broken lines should at the mold's edges.

After broken, because metal film is cut into pieces (Fig. 5.3b), it can not be considered as a whole film any longer. Those pieces of broken metal film lose the holding pull from their neighbors. However, the pieces underneath the convex structures are still held by the convex structures and PMMA layer. Hence, those pieces cannot slide laterally. But they can be pushed down directly by the convex structures of the mold. As for the pieces of the Al film which were between the convex structures and in the channels, they lose the pull forces from the neighbors. They would be pushed up and aside by the softened PMMA layer. Because they were attached onto the surface of the PMMA layer, they would be elongated continuously with the deformation of the PMMA. However, when the elongation of metal film exceeded the maximum elongation of metal

material, or the internal stress in the metal film exceeded the ultimate tensile strength of metal material, these parts would be broken into pieces.

Therefore, deeper mold insertion causes more deformation of PMMA and creates more cracks on the metal film.
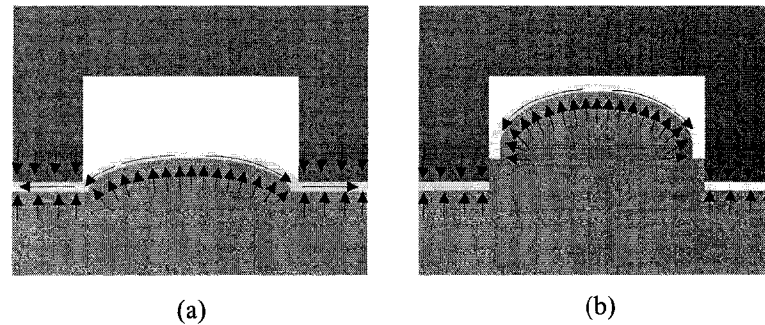
Figure 5.3 The forces on the Al film during ILL process, (a) before Al film was broken, (b) after Al film was broken.
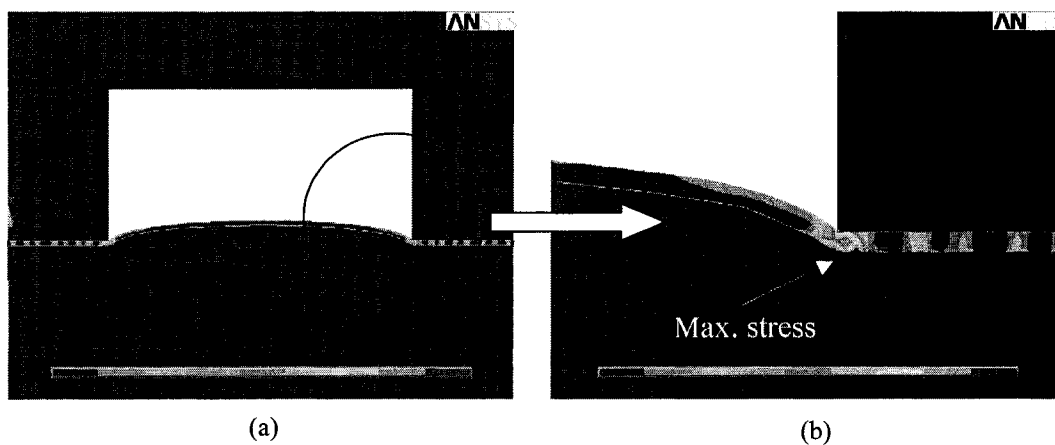
Figure 5.4 Stress distribution before the Al film breaks. The maximum stress on the Al film is just underneath the edges of the convex structure.

5.4 Cross-Sectional Profiles After ILL Method

The ILL method has been applied to generate various Al patterns of lateral dimensions ranging from 10 to 300 μm, including lines, square dots, square holes, and truss structures (Fig. 5.5). These experimental results indicate that the ILL method can be potentially used to generate metal patterns commonly used in the MEMS area.
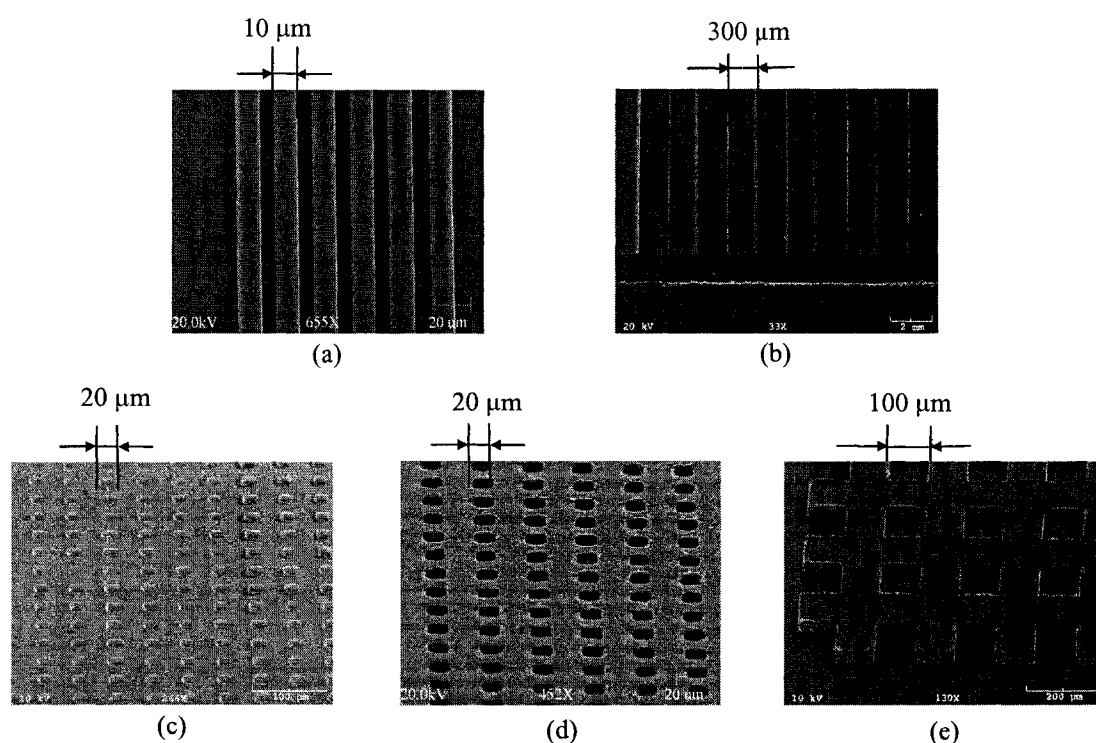
Figure 5.5 SEM (scanning electron microscopy) pictures of different Al structures: (a) microwires with a width of 10 μm, (b) microlines with a width of 300 μm, (c) square dots with dimensions of 20×20 μm², (d) square holes with dimensions of 20×20 μm², and (e) truss structures of lateral dimensions of 100 μm.

A representative sidewall generated is shown in Fig. 5.6. It is interesting to see that an Al film may not be perfectly cut along the edges of convex mold structures, and may also appear on the upper part of the sidewalls. One possible explanation was found through the simulation. Figure 4.1 shows the geometric model used in the simulation.

Figure 4.2 gives the corresponding simulation results. During the mold insertion in the ILL, the part of the Al film underneath the convex structure is pushed down and suffers a downward force. Meanwhile, the PMMA underneath the convex structure flows out and fills the neighboring concave mold structures. During the initial mold insertion (Fig. 4.2a), PMMA in the concave mold structures curves up due to surface tension. The Al on this part of PMMA curves up accordingly and is elongated. At the same time, the Al right underneath the convex structures is just pushed down without much deformation, while stress concentrations occur at the edges of this part of Al (Fig. 4.3).

After the further mold insertion, the maximum stresses at the stress concentration increase and break the Al at the same locations. Consequently, the part of Al right underneath the convex mold structures is cut off and further pushed down (Fig. 4.2b). Meanwhile, due to the fact that more PMMA flows from the region right underneath the convex mold structures to the concave mold structures, the PMMA gets deeper inside the concave mold structures, and the part of the Al in the concave mold structures is further separated from the part of Al underneath the convex mold structures. When the PMMA completely fills the concave mold structures, the top surface of the PMMA, as well as the Al on the top of the PMMA, is flattened. During the process of filling the concave mold structures, the Al is elongated. After it is flattened, the elongated part deflects and stays on the upper part of the sidewall of the PMMA (Fig. 4.2c). In addition, it was also noted: (i) the part of Al underneath Si concave structures also suffers deformations as it is pushed up into the Si concave structures by PMMA, (ii) these deformations increase with the insertion depth, and (iii) a deep mold depth induces large stresses. Because the

stresses are larger than the break strength of Al, the part of Al in the concave structures breaks.

The edge of cut-off and pushed-down Al

The edge of uncut Al

(a)   (b)
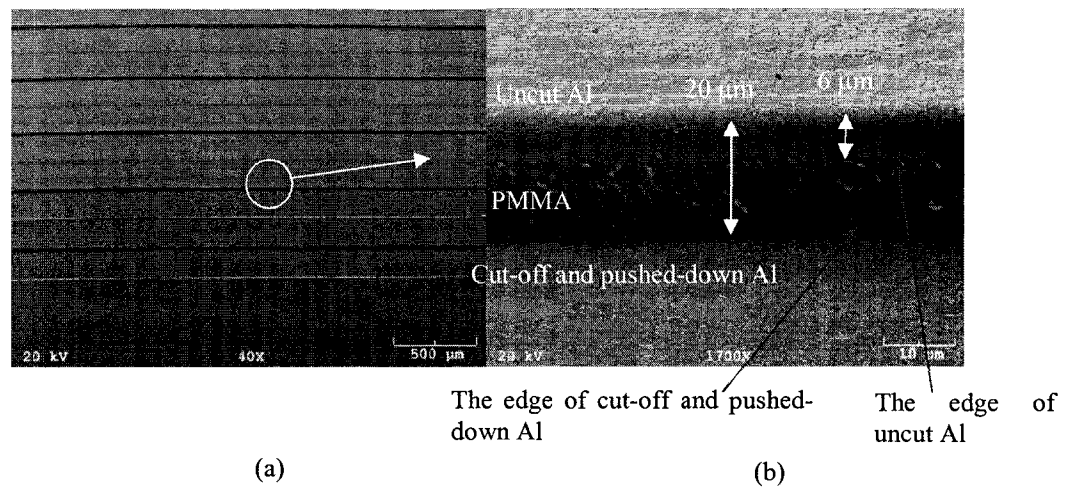
Figure 5.6 (a) Top (SEM) view of 300 μm microlines, and (b) sidewall of a representative microline.

It is found from the simulation results that the ratio of the length, a / b, of the two parts is dependant on the embossing temperature (Fig. 5.7). The higher temperature may cause the smaller Young's modulus of the PMMA. The Young's modulus of Al is assumed as a constant. Therefore, higher temperature increases the difference of Young's modulus between PMMA and Al and forces Al film to deform more to match the deformation of PMMA. That means the part of extended Al film becomes longer and longer with embossing temperature increasing. In the other words, the ratio a / b is larger and larger.

(a)   (b)
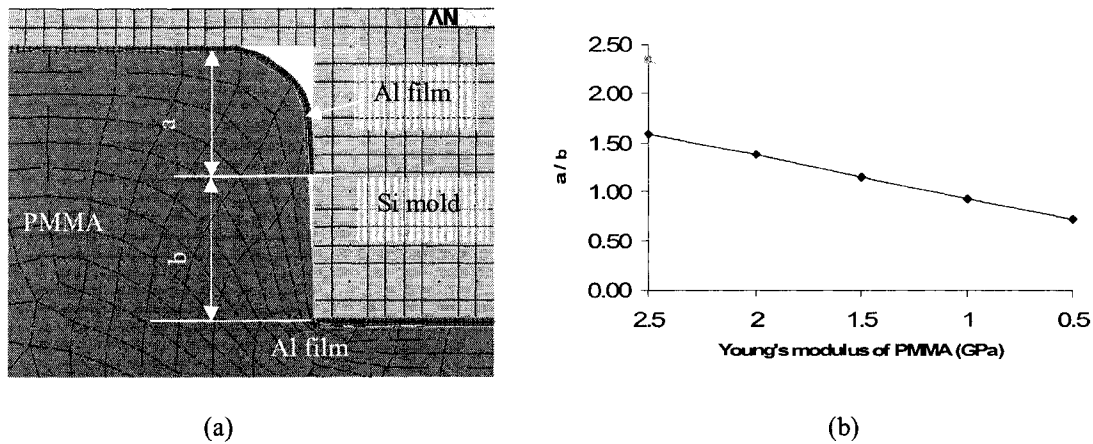
Figure 5.7 Al film on the sidewall of PMMA micro line. (a) Deformation after mold insert into 35 μm. (b) The temperature dependence of a / b.

Another interesting point found is that large patterns are taller than small patterns. Figure 5.8 shows such an example. In a microheater pattern, the two contact pads had a height of 100 μm, while the serpentine-shaped wires between the two contact pads had a height of 40 μm. Simulation was conducted to address this phenomenon (Fig. 5.9). The simulated mold and the PMMA had the same dimensions as those used in the experiments. Figure 5.9(a) shows the deformations of the PMMA during the molding process. The simulated PMMA heights in the large and small cavities were 100 μm and 15 μm, respectively. Figures 5.9(b), (c) and (d) give the distributions of displacement vectors at nodes, the normal stress components along the y direction on the central lines of a 500-μm-wide cavity and the 50-μm-wide cavity right beside this 500-μm-wide cavity, and the normal stress components along the x direction. These results were used to examine how the PMMA flowed and got into the cavities. Figure 5.9(b) shows that the PMMA underneath the mold region involved with small cavities (i.e., the region ABCD labeled in Fig. 5.9(a) intended to flow toward the large cavities. Figure 5.9(c) shows that

the normal stress components which were along x direction was negative in the region below the interface of the mold and PMMA.

(a)   (b)
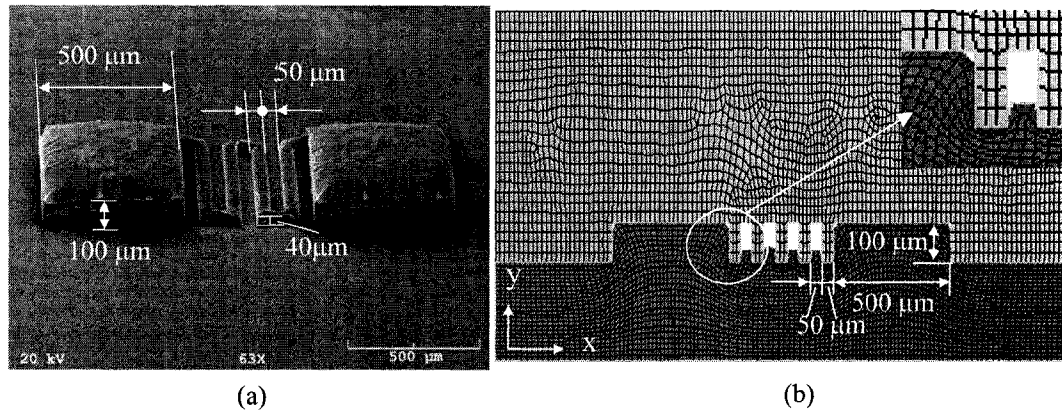
Figure 5.8 (a) A microheater sample created by ILL; the heater wires and the contact pads had different heights. (b) The simulation result shows that there is a height difference when wide and narrow structures are generated together.

Since the Poisson's ratio of the PMMA was positive, the normal stress components along the x direction favored the stretching of the PMMA along the y direction and the flow of the PMMA into the cavities. Figure 5.9(d) indicates that the normal stress components along the y direction on the central lines of the large and small cavities are negative at the regions far below the interface of the mold and PMMA, meaning the PMMA was compressed over there. At the places below the interface, the magnitudes of the normal stress components along the central line of the 50-μm-wide cavity was larger than those along the central line of the 500-μm-wide cavity, implying that the PMMA under the small cavity was compressed harder by the mold. On the other hand, the normal stress components above the interface were positive, indicating that the PMMA in the cavities was pushed up and that the normal stress components along the y direction also favored the flow of the PMMA into the cavities.
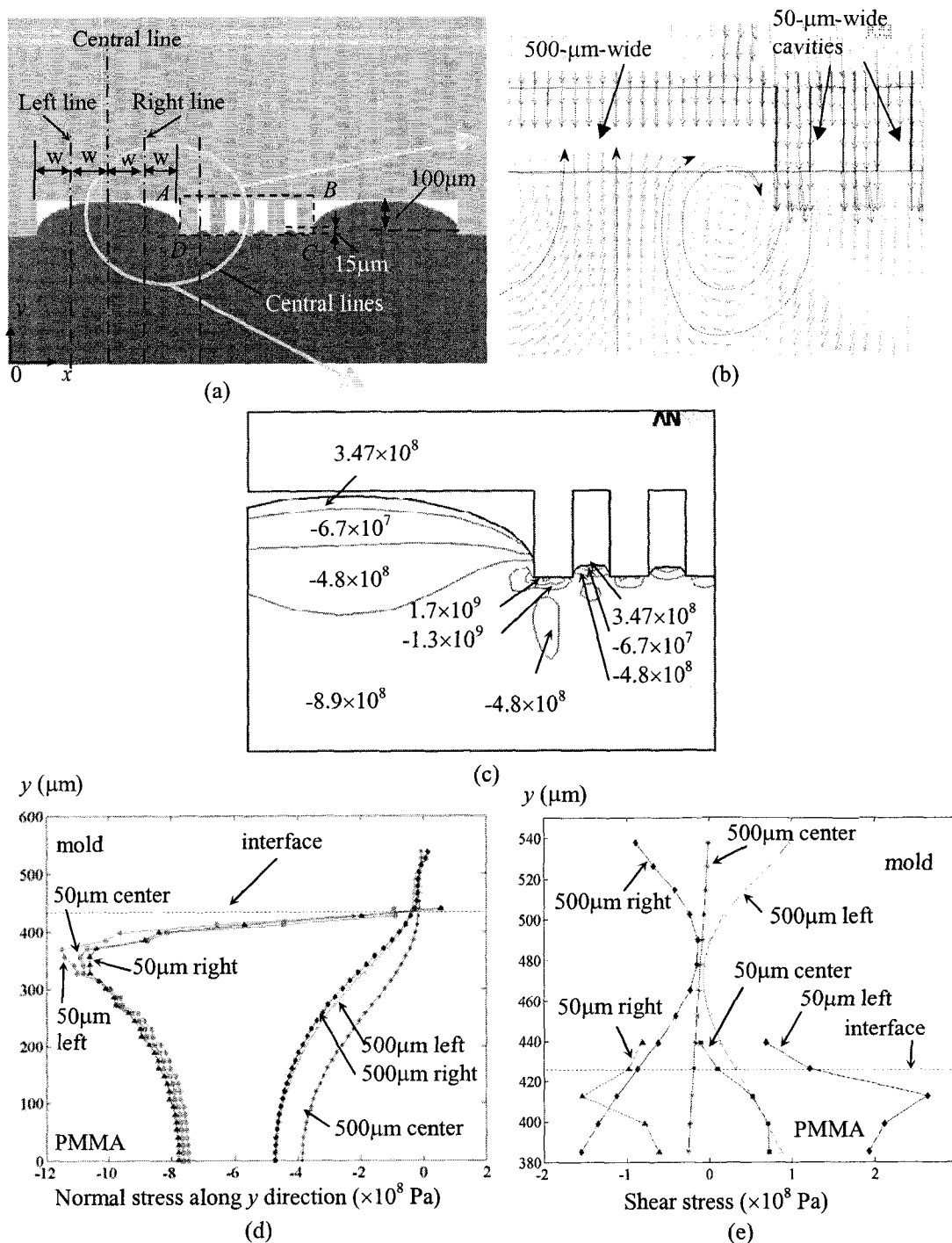
Figure 5.9 (a) Deformations of PMMA. (b) Map of displacement vectors at nodes: part of the PMMA underneath the mold region involved with small cavities (i.e., the region *ABCD* labeled in Fig. 11a) intended to flow toward the large cavities. (c) Distribution of the normal stress components (along the *x* direction) in the PMMA. (d) Normal stress components (along the *y* direction) and (e) distributions of shear stress components along the left, central, and right lines in both cavities whose widths are 500 and 50 μm, respectively.

The 500-μm-wide cavities were much wider than the 50-μm-wide cavities. This was a key factor which induced the phenomenon of height difference. The surface tension on the sidewalls of a 500-μm-wide cavity can be considered the same as that on the sidewalls of a 50-μm-wide cavity because of the same sidewall conditions. However, since the large cavity is much wider than the small cavity, the surface tension has less effect on the central region of the large cavity. Consequently, the PMMA in this region suffers less shear stress, i.e., less resistance to its flow. To see this point more clearly, three vertical lines were considered for the 500-μm-wide cavity: the left, central, and right lines. The central line went through the center of the cavity, while the left and right lines were located on the left-handed and right-handed sides of the central line, respectively, and were 125 μm away from the central line along the x direction (Fig. 5.9(a)).

Another three vertical lines were also picked for the 50-μm-wide cavity right beside the 500-μm-wide cavity: the left, central and right lines. The central line went through the center of the small cavity, while the left and right lines were located on the left-handed and right-handed sides of the central line, respectively, and were 12.5 μm away from the central line along the x direction. Shear stress distributions around the cavities were found and given in Fig. 5.9(e). Two points can be seen from this figure. First, the magnitudes of the shear stresses on the central line of either cavity were smaller than those on the left and right lines, making the PMMA on the central line easier to move up than that on another two lines. Consequently, the PMMA at the central line should be higher than that on another two lines. Second, the magnitudes of the shear stresses inside the 500-μm-wide cavity were smaller than those inside the 50-μm-wide

cavity, making the PMMA inside the large cavity easier to move up than that inside the small cavity. This reason might be why the PMMA pattern inside the large cavity was taller than that inside the small cavity.

5.5 Thicknesses of Al Films

It was found in our experiments that thin Al films were relatively easy to break during the molding processes. As seen in Fig. 5.10, under the same molding conditions (imprinting and demolding temperature were 140 and 95° C, respectively, and applied force was 1600 N), 100-nm-thick Al films broke, while 500-nm-thick Al films did not. The cracks of the Al films were detected as follows: the silicon substrate was removed from the PMMA sheet, and the PMMA sheet was placed on the stage of an optical microscope. The light source underneath the stage was turned on, and finally, the patterns were watched from above the sample. PMMA was transparent to the light, while Al was not. Light should be seen in the sample area which was not covered with Al. According to the light patterns, the Al distribution could be identified. As shown in Fig. 5.10a, the light was seen at the places where Al cracked. The Al cracks were found in the neighborhoods of microline edges but not in the central area of these microlines, indicating that these cracks might be introduced by the pulling forces from the part of cut-off Al during the fracture phase (Fig. 1.16d). On the contrary, cracks were not seen in the 500-nm-thick Al films (Fig. 5.10b). The light was only seen at the microline edges, indicating that the microlines were cut off as designed in Fig. 1.14.

(a)   (b)
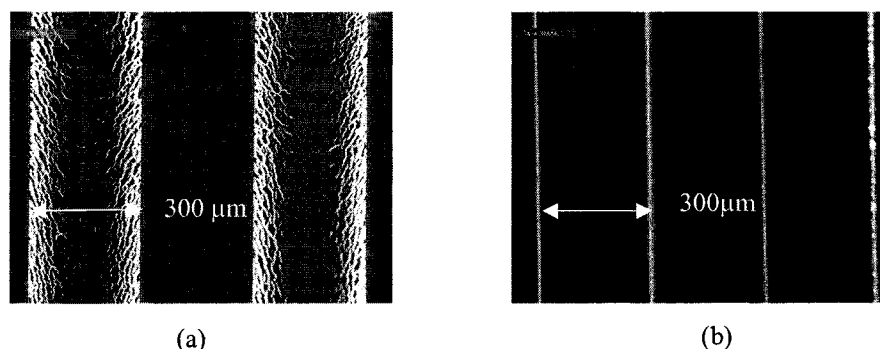
Figure 5.10 Optical pictures of 300-μm-wide microline created through Si mold with a depth of 45 μm. Thicknesses of coated Al films are (a) 100 nm and (b) 500 nm. Light came from underneath the samples, and cracks were seen on the 100 nm Al film in picture (a).

5.6 Demolding Temperature

The demolding temperature used in this work was around 80 - 95° C. If it was 95 - 105° C, since it was close to T_g of PMMA, the patterns which were created by ILL method might be recovered. If it was lower than 80° C, high friction forces would generate between the Si molds and the PMMA substrates due to the increase of PMMA's viscosity induced by the low temperature. The very high friction may cause patterns to deform (Fig. 5.11), or even damage the Si mold. Figure 5.12 shows a sample in which imprinting and demolding temperatures were 160 and 70° C, respectively. The high friction forces made PMMA sheet curve up after the separation of the Si mold and the PMMA.
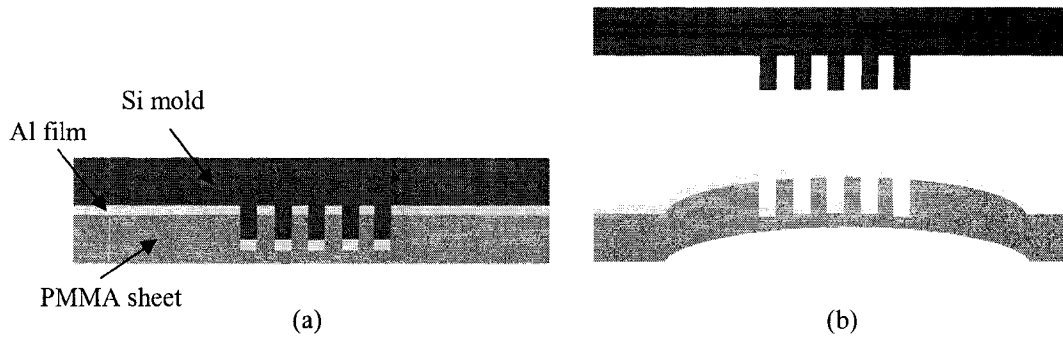
Figure 5.11 Schematic of 3D structure made through ILL method using low demolding temperature: (a) before demolding and (b) after demolding.
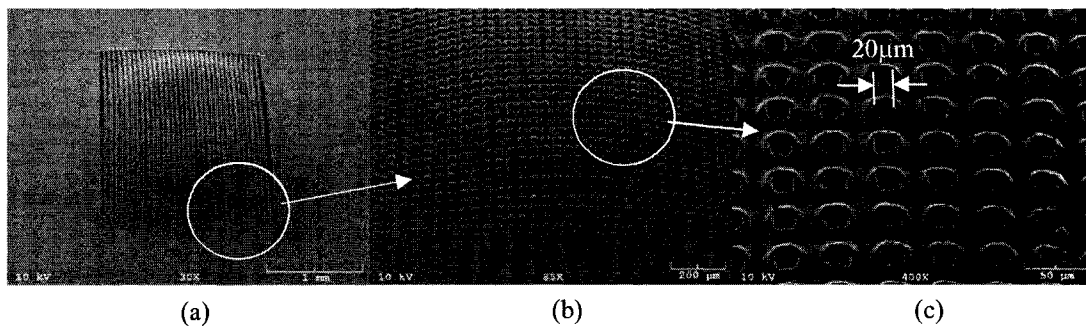
Figure 5.12 Square-hole arrays on a vaulted structure fabricated using the ILL at a low demolding temperature of 70° C (SEM): (a) an overview of the whole structure; (b) and (c) close-up views.

5.7 Mold Depth

An advantage of the hot embossing technique is the high aspect ratio of its features. However, high aspect ratio may cause cracks in the Al film on the desired patterns in the ILL method. In Section 5.4, a phenomenon was mentioned that the part of Al in Si concave structures may break due to large mold depth. When the PMMA completely filled into the cavities of the Si mold, the height of patterns is equal to the mold depth (i.e., the depth of the cavities of the Si mold). Two products were compared in Fig.5.13. Microlines (Fig. 5.13 (a1) and (b1)) and microblocks (Fig. 5.13 (a2) and

(b2)) were fabricated through the Si mold with depth 20 and 80 μm, respectively.

Patterns made by 20-μm-deep mold have the desired breaking lines at the mold edges.

However, Al film on the patterns made by 80-μm-deep mold has lots of irregular cracks.

Mold depth = 20 μm   Mold depth = 80 μm

(a1)   (a2)

(b1)   (b2)
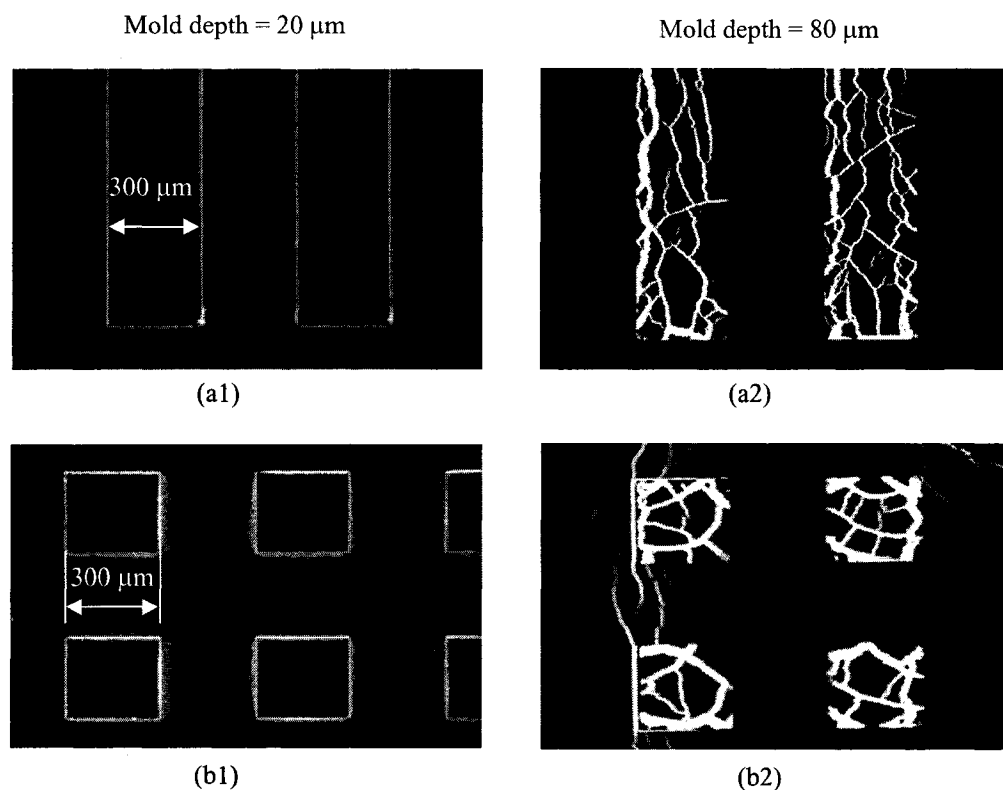
Figure 5.13 Optical pictures of 300-μm-wide microlines (a1 and a2) and micro blocks (b1 and b2) created through Si molds with a depth of 20 (a1 and b1) and 80 μm (a2 and b2), respectively. Thicknesses of coated Al films are 500 nm. Light resource came from underneath the samples. Black area is covered by Al film and white area stands for cracks of Al film. Al cracks were seen on the patterns created through 80-μm-deep Si mold.

In order to explain this phenomenon, the deformation development in the ILL method must be considered. During the initial mold insertion (Fig. 5.14a), PMMA in the concave mold structures curves up due to surface tension. The Al on this part of the PMMA curves up accordingly and is elongated. At the same time, the Al right underneath the convex structures is just pushed down without much deformation, while stress

concentrations occur at the edges of this part of Al. After further mold insertion, the maximum stresses at the stress concentration increase and break the Al at the same locations. Consequently, the part of Al right underneath the convex mold structures is cut off and further pushed down (Fig. 5.14b). Meanwhile, due to the fact that more PMMA flows from the region right underneath the convex mold structures to the concave mold structures, the PMMA gets deeper inside the concave mold structures, and the part of the Al in the concave mold structures is further separated from the part of Al underneath the convex mold structures.

However, the ends (A and B point) of the Al film in the concave structure of Si mold suffer pressure from soften PMMA. They are squeezed on the walls of the cavity of the mold. Hence, friction forces are generated between the walls and the Al film at points A and B. The ends may be fixed there or may move up slowly with further mold insertion. The remainder of the Al film (i.e., the middle part) in the cavity only suffers pressure from hyperelastic PMMA. Hence, the middle part of the Al moves up. It makes the Al film in the cavity elongate more and more (Fig. 5.14c). The deformation of the Al film includes elastic and plastic components. If the total deformation exceeds the ultimate elongation of Al, the Al film cracks. When the PMMA completely fills the concave mold structures, the top surface of the PMMA, as well as the Al on the top of the PMMA, is flattened. At this time, an elastic deformation may reverse, but a plastic one can not. After the pattern is flattened, the excess part of the Al film deflects and stays on the upper part of the sidewall of the PMMA (Fig. 5.14d).

(c)   (d)
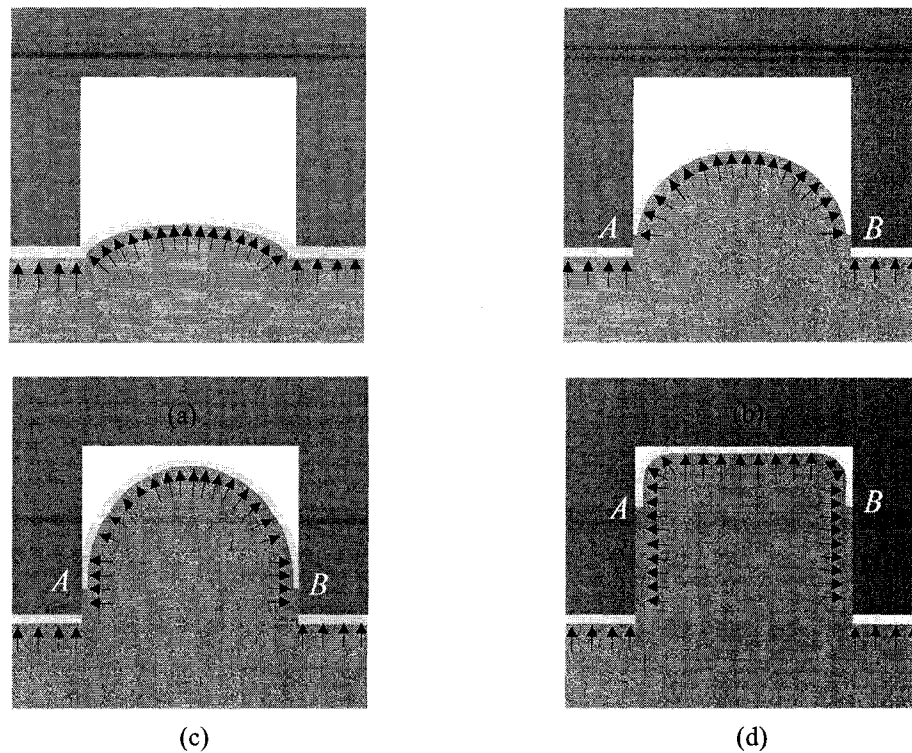
Figure 5.14 The flow of softened PMMA with Al into the channel: (a) before the Al film is broken, it is an integrated unit and suffers elastic and plastic deformation; (b) – (c) after the Al film is broken, the part of Al film in the channel continues to be pushed up by the PMMA and experiences more deformation; (d) the final shape of the Al film and the PMMA layer is depends on filled profiles in the mold cavities. Arrows stand for pressure given by the PMMA.

In order to find the relationship between the geometry of the Si mold and the deformation of the Al film in the cavity of the mold, it is assumed that the part of the Al film in the channel does not break during the whole PMMA filling process. In Fig. 5.15, the solid yellow line and dashed white line shows the shapes of the Al film when it just touches the ceiling of the channel and when the PMMA completely fills the channel.
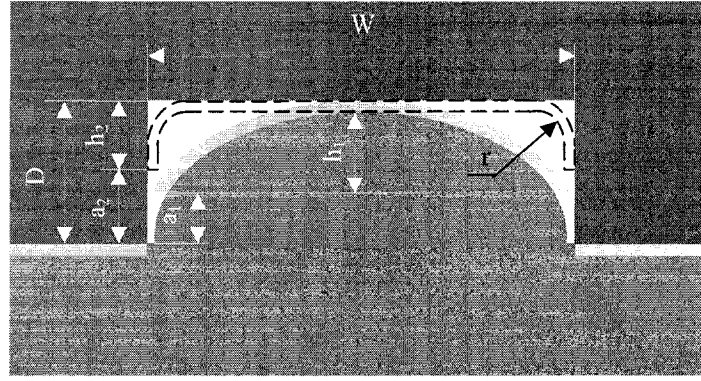
Figure 5.15 The geometry of PMMA and Al film during ILL method. A solid yellow line stands for the case when Al film just touches the ceiling of the channel of silicon mold. The dashed line is the shape of Al film after complete filling.

Neglecting the elastic deformation, it is supposed the length of the Al film in the channel does not change after it is separated from its neighbors. The length of Al film, when it just touches the ceiling of the channel is

$$L_1 = \frac{W\left(\pi - 2ac\tan\left(\dfrac{\dfrac{1}{2}W - \dfrac{2a_1D}{W}}{D - a_1}\right)\right)}{\sin\left(\pi - 2ac\tan\left(\dfrac{W}{2D}\right)\right)} .$$
(5.1)

If the chamfer is assumed as 0 (i.e. $r = 0$) for simplification, when the PMMA completely fills into the channel, the length of Al film is

$$L_2 = W + 2h_2 .$$
(5.2)

Combining the above two equations and noting $L_1 = L_2$,

$$h_2 = \frac{\dfrac{1}{2}W\left(\pi - 2ac\tan\left(\dfrac{\dfrac{1}{2}W - \dfrac{2a_1D}{W}}{D - a_1}\right)\right)}{\sin\left(\pi - 2ac\tan\left(\dfrac{W}{2D}\right)\right)} - \frac{1}{2}W .$$
(5.3)

If $a_I = 0$, then Equation (5.3) will be simplified to

$$\frac{h_2}{D} = \frac{W}{2D}\left[\frac{\left(\pi - 2ac\tan\left(\frac{W}{2D}\right)\right)}{\sin\left(\pi - 2ac\tan\left(\frac{W}{2D}\right)\right)} - 1\right].$$ (5.4)

When the curve $\frac{h_2}{D}$ vs. $\frac{W}{D}$ is plotted in Fig. 5.16, it is clear that the Al film part,

which is bent onto the sidewall of the PMMA, is related to the geometry of mold,

$\frac{h_2}{D} \propto \frac{W}{D}$. Keeping the same width, a deeper mold may make more Al film bend onto the

sidewall of PMMA. It may create larger deformations of Al film and make it more easily

broken.
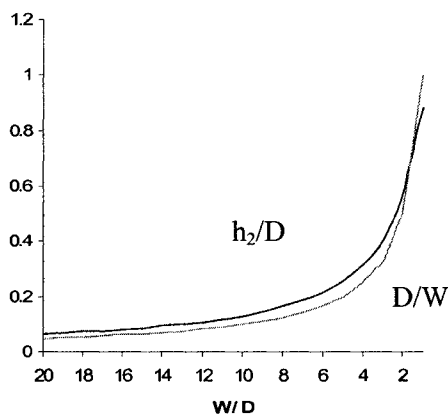
Figure 5.16 The relationship between the residual Al film on the sidewall of PMMA and the geometry of the silicon mold.

An interesting observation is that the value of h_2/D is close to D/W. Hence, the

width (W) and depth (D) of the channel can be used to roughly estimate the residual Al

film on the sidewall of PMMA, h_2.

Al film is elongated while the PMMA fills into the cavity of the Si mold. To keep

the same volume at any time, Al film has to decrease its thickness. Therefore, there must

be stress concentration points on the Al film. Figure 5.17 shows stress distribution when

the mold insertion is 35 μm. The maximum stress happens at the end of the Al film. The

stress on the Al film is non-uniform. If the maximum stress does not exceed the ultimate

strength, which is 200 MPa, the part of the Al film in the channel does not break.
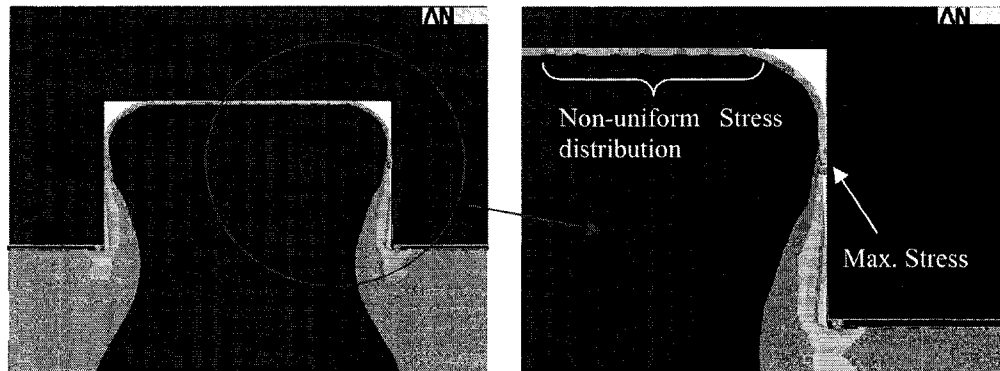
Figure 5.17 Simulated stress distributions on Al film by Ansys 8.0.

The break elongation of thermal deposited Al film is around 5%. That

means $\dfrac{2h_2}{W} = 5\%$. From Equation (5.4),

$$\frac{2h_2}{W} = \frac{\pi - 2ac\tan\left(\dfrac{W}{2D}\right)}{\sin\left(\pi - 2ac\tan\left(\dfrac{W}{2D}\right)\right)} - 1 \leq 5\% \tag{5.5}$$

Let

$$x = \pi - 2ac\tan\left(\frac{W}{2D}\right).$$

(5.6)

Then

$$\frac{x}{\sin x} - 1 \leq 5\% .$$

(5.7)

Since

$$\sin x = \sum_{k=1}^{\infty}(-1)^{k+1} \frac{x^{2k-1}}{(2k-1)!} = x - \frac{x^3}{6} + ...$$

(5.8)

By combining (5.7) and (5.8) and obliterating the higher order terms,

$$\frac{x}{x - \frac{x^3}{6}} - 1 \leq 0.05 .$$

(5.9)

Solving this equation,

$$x \leq 0.53 .$$

(5.10)

Substitution of Equation (5.6) into (5.10) leads to

$$\frac{W}{D} \geq 7.3 .$$

(5.11)

Although there are several assumptions for simplifying the calculation, this result is close to our experiment observation: a series of Si molds with depths of 10, 20, 30, 40, 50, 60, and 80 µm was used to pattern 500-nm-thick Al film using the ILL method. The features were microline with 300 µm width and 5000 µm long. The shallow molds, such as 10, 20, 30, and 40 µm, did not create cracks in the Al film, while the deeper molds,

such as 50, 60, and 80 μm, did. The limitation depth of the Si mold should between 40 to 50 μm. When (5.11) is applied, since $W = 300$ μm, $D \leq 41$ μm. Equation (5.11) is very useful to design patterns in using ILL method.

5.8 Optimize Experiment Parameters Using Taguchi Methods

In the previous sections of this chapter, some factors were discussed, which affect the quality of Al micro patterns fabricated using the ILL method, such as imprinting temperature and demolding temperature. In order to gain qualified products, Taguchi methods were used to optimize those control parameters.

Dr. Genichi Taguchi, a Japanese engineer of Nippon Telephones and Telegraph Company, proposed several approaches to experimental designs that are sometimes called "Taguchi Methods" [38,40]. These methods utilize two-, three-, and mixed-level fractional factorial designs. Large screening designs seem to be particularly favored by Taguchi adherents [38]. Taguchi methods have already been used to optimize parameters in hot embossing processes [23, 39].

At first, 'brainstorm' was used to list all the control parameters in the ILL method. Then, a cause-effect diagram (Fig. 5.18) was developed to find the major factors. There are six major factors in the ILL method: imprinting temperature, demolding temperature, embossing pressure, mold holding duration, thickness of Al film, and geometry of Si mold.
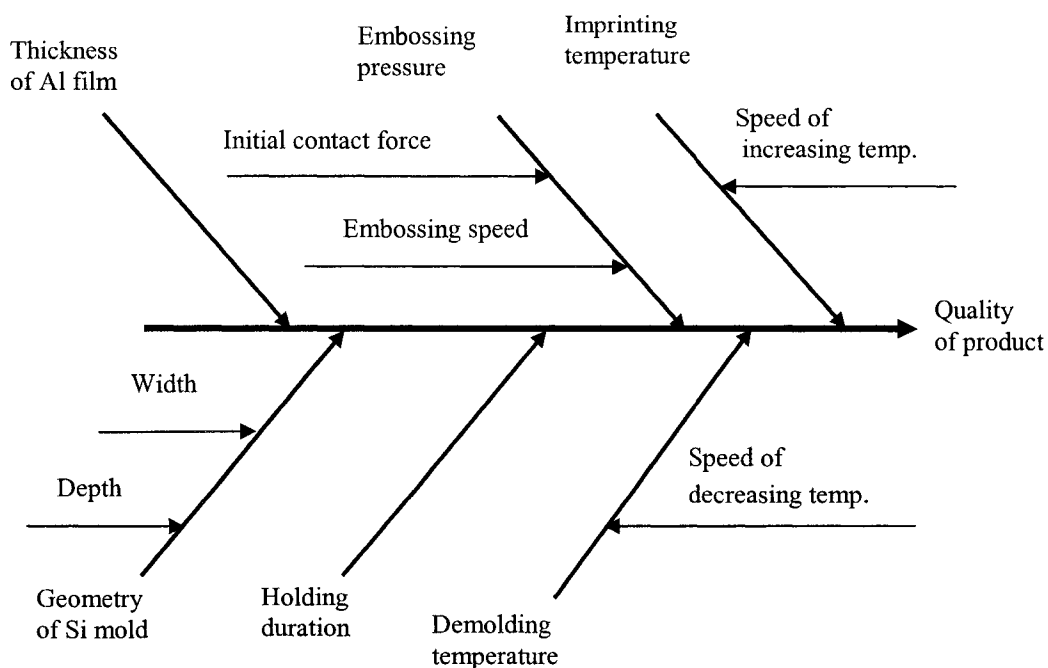
Figure 5.18 Cause-effect diagram of ILL method.

In Sections 5.5 and 5.7, the effects of thickness of Al film and geometry were detailed. These two parameters should be concerned in the original phase of product design. They are not process-control parameters. The remaining four processing parameters were selected as major factors for evaluation in the ILL method. They are imprinting temperature, embossing pressure, holding duration, and demolding temperature. Table 5.2 lists the processing parameters and parameter levels selected in the main experiment. The mold depth is 40 μm and Al thickness is 500 nm. The imprinting temperatures were 120, 130, and 140° C. The embossing pressures were 1, 1.5, and 2 MPa. The holding durations were 400, 500, and 600 sec. The demolding temperatures were set at 75, 85, and 95° C. To identify the relative significance of these four parameters using trial-and-error method, a large array of experiments with as many as 81 runs is required. The Taguchi method was used to reduce the experimental runs.

The levels of processing conditions and the experimental array used are shown in Table 5.3.

Table 5.2 Parameters and levels selected in the main experiment

Parameters	Level 1	Level 2	Level 3
A: Imprinting Temperature (°C)	120	130	140
B: Embossing pressure (MPa)	1	1.5	2
C: Holding duration (Sec)	400	500	600
D: Demolding temperature (°C)	75	85	95

Table 5.3 The L_9 orthogonal array used in the main experiment

Runs	Parameters			
	A	B	C	D
1	1	1	1	1
2	1	2	2	2
3	1	3	3	3
4	2	1	2	3
5	2	2	3	1
6	2	3	1	2
7	3	1	3	2
8	3	2	1	3
9	3	3	2	1

The quality factors of patterns include dimensions (length, width and height), profile of cross section (e.g., round edges and incomplete filling of PMMA), surface roughness and defects in the Al film (e.g., micro cracks, dots or holes). Any one of them

can not substitute the others. In other word, only one of the process factors can not be picked up as the target criteria. Hence, a 5-point valuation system was set up to evaluate the quality of the patterns fabricated using the ILL method (Table 5.4).

Table 5.4 Quality levels of patterns fabricated using ILL method

Quality level	Explanation
5	Dimensions are exact. PMMA filled into the cavities completely. Small round edges. Every surface is smooth. There is no obvious defect in Al film.
4	Dimensions are exact. PMMA filled into the cavities completely. Allow big round edges. Every surface is smooth. There are few minor defects in Al film.
3	Dimensions are exact. PMMA filled into the cavities completely. Allow big round edges. Few surfaces are rough. There are few minor defects in Al film.
2	Width and length are exact. Height is not exact. PMMA filled into the cavities incompletely. Few surfaces are rough. There are many obvious defects in Al film.
1	None of the dimensions are exact. PMMA did not filled into the cavities completely. Many surfaces are rough. There are many obvious defects in Al film or Al film collapses into many pieces.
0	No pattern at all, or no Si mold breaks.

Bigger-the-Best design [40] was adopted. The experiment data are listed in Table 5.5. The corresponding ratio of signal to noise (S/N) response table and figure was obtained in Table 5.6 and Figure 5.19. Accordance to the response table and figure of S/N ratio, the optimal combination parameter of current research was A3 (140° C), B3 (2 MPa), C2 (500 sec), and D3 (95° C). In the four parameters, demolding temperature has the largest effect on the quality of patterns.

Table 5.5 Tabulation of the quality for a microwire in the main experiment

Runs	Samples			Average	S/N
	Sample 1	Sample 2	Sample 3		
1	1	2	2	1.68	3.01
2	5	3.5	2	3.5	9.07
3	5	5	5	5	13.98
4	5	4.5	4	4.5	12.96
5	2	1	4	2.33	3.59
6	3.5	2.5	5	3.67	10.27
7	5	4.5	5	4.83	13.65
8	5	3	4	4	11.47
9	3	4	3.5	3.5	10.7
Optimum	7.39	6.98	10.05	9.65	15.7

Table 5.6 Average S/N table

	A	B	C	D
S/N level#1	8.69	9.87	8.25	5.77
S/N level#2	8.94	8.05	10.91	11
S/N level#3	11.94	11.65	10.41	12.8
Effect estimate	3.26	3.61	2.66	7.04
Rank	3	2	4	1
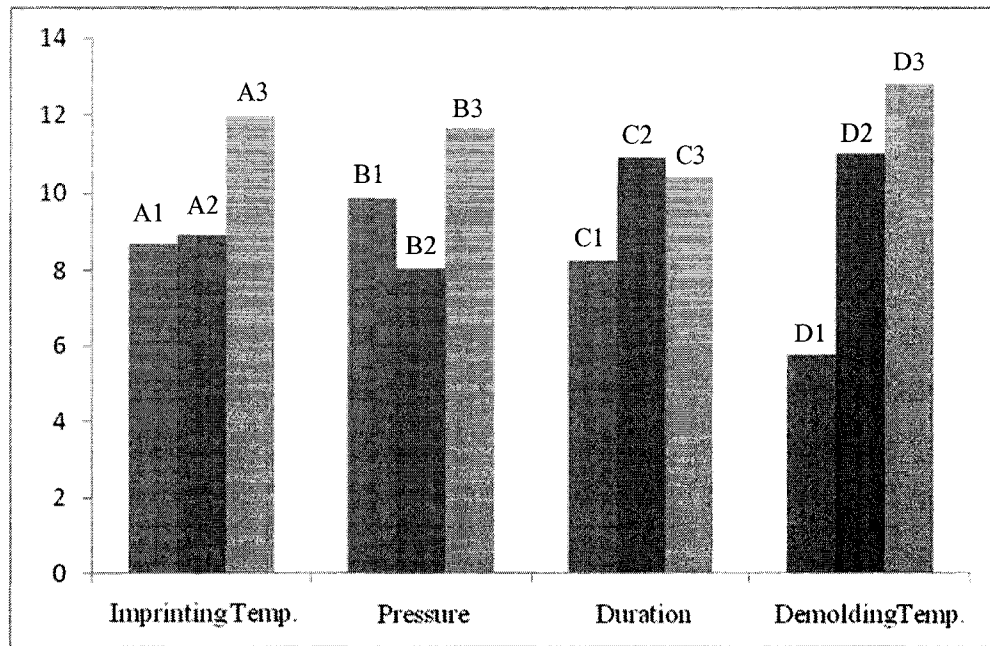
Figure 5.19 Control factor of S/N ratio.

5.9 Cutting of Au

The cutting of Au films was also examined using the ILL method. As shown in Fig. 5.20, 500-nm-thick Au films could be cut as well. However, an interesting phenomenon was observed in the experiments, i.e., under the same imprinting conditions, the patterned Al film which has same thickness as Au film may collapse due to large deformation, while the Au did not. For the examples shown in Fig. 5.20, when the imprinting and demolding temperatures were 140 and 95° C, respectively, the mold depth was 80 μm and the applied force was 1,800 N, and the Al film cracked while the Au did not. This result is due to the higher ductility of the Au. The break elongations of Au and Al are around 60% and 5%, respectively. Therefore, under the same deformation conditions, Al is easier to break than Au.

(a1)   (a2)   (a3)

(b1)   (b2)
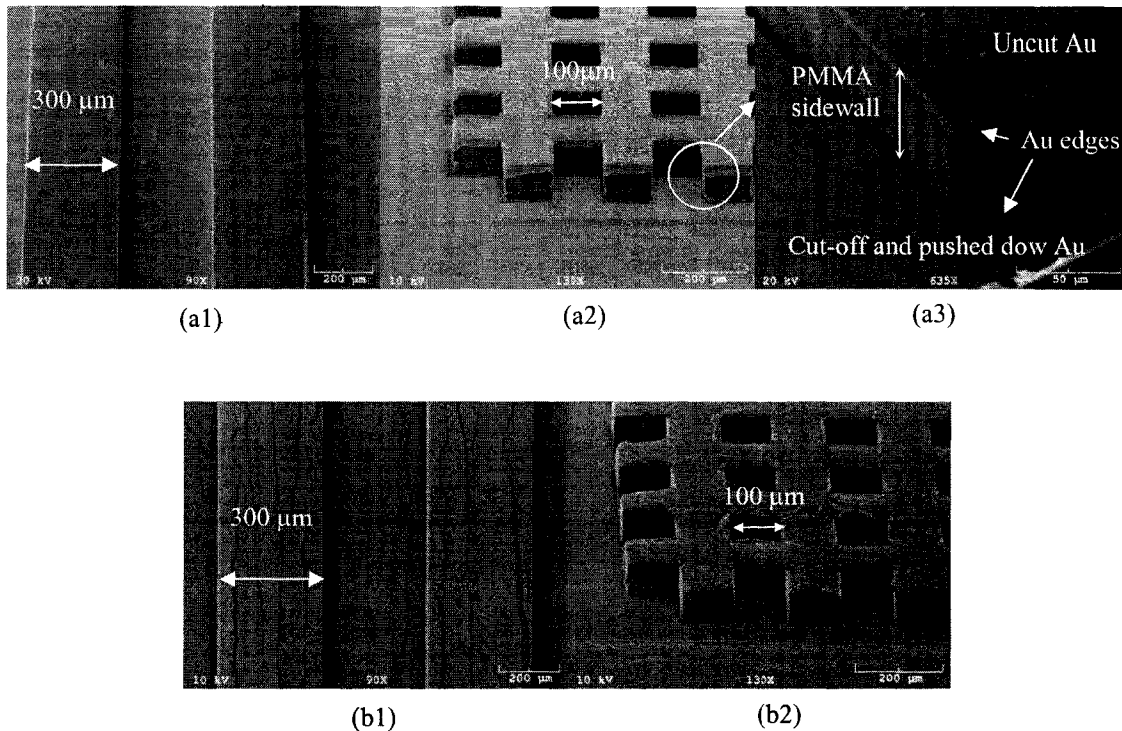
Figure 5.20 Comparison of Al and Au patterns created through ILL method (SEM). Au patterns are given in (a1) and (a2), and Al patterns are shown in (b2) and (b2). The sidewall of a Au microline is shown in (a3). The patterns had a height of 80 μm. Both the Al and Au films are 500 nm thick. The Al films crack while the Au layers do not.

5.10 Patterning of Free Standing Al foil

In the previous sections, the Al films with 100 - 500 nm were successfully patterned using the ILL method. In order to examine the potential of the ILL method, an Al foil with 10 μm thickness was patterned because it is hard to deposit extremely thick Al film on a PMMA sheet.

The pattern procedure is as follows. First, a piece of Al foil is placed on a PMMA sheet. Second, a hot embossing process is applied. Third, after the sample is allowed to cool and the Si mold is released, the sample is withdrawn. The Al foil is peeled off from the PMMA sheet. Al foil is relatively thicker and stronger than the thermal-deposited Al

film, and Al foil has much less attached force to the PMMA sheet. Hence, one of advantages of using Al foil is that it can be easily peeled from the PMMA sheet. The debris cut from Al foil can be stuck on the PMMA sheet and used as patterns. Figure 5.21 shows such an example.

The advantages to pattern Al foil are: 1) Unwanted material can be removed. 2) The Al foil, which is peeled from a PMMA sheet, is the unwanted part; however, it may have other applications, for example, serving as a mask for stencil technique.

(a)   (b)
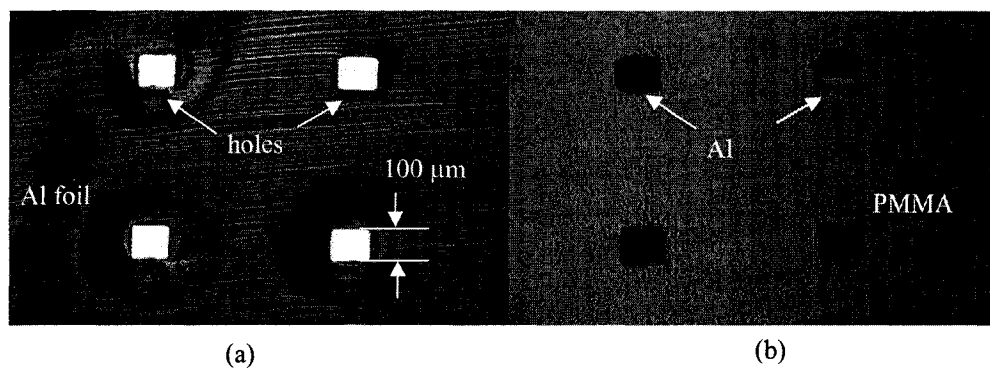
Figure 5.21 (a) Optical picture of square holes fabricated on 10-μm-thick Al foil using ILL method. Light resource came from underneath of the sample. Black and white areas stand for Al foil and pierced holes, respectively. (b) Debris of Al cut from Al foil was attached on the PMMA sheet. This picture was taken via an optical microscopy. Light sources came from both front and back sides of the samples.

5.11 Inspection Techniques of Cutting-off

Although it could be identified directly from the SEM pictures of the generated patterns whether the Al patterns were cut off as discussed in Section 5.4, three methods are used to assist examination of this cutting-off issue. These three methods were optical microscopy, energy dispersive spectrometry (EDS) analysis, and electrical resistance measurement.

5.11.1 Optical Microscopy

Optical microscope is a basic metrology instrument. It is widely used in IC and MEMS field due to its simple operation and naturally visual image. In this work, an optical microscope was used to check the profile of patterns and judge whether Al film is cut through or not.

The key point of the ILL method is that an Al film is cut through by insertion of a Si mold. If the Al film is not cut through, the patterns still connect to the other part of the Al film. The short problem may happen.

If the Al film has been cut through at the mold's edges as expected, there are cracks around the patterns. A simple way to examine the cutting is via optical microscopy: a light resource is placed underneath the sample. Because PMMA is transparent and Al film is opaque, the light beam travels through the PMMA sheet and comes out of the cracks in the Al film (Fig. 5.22a). Hence, there are bright lines around patterns (Fig. 5.22b).
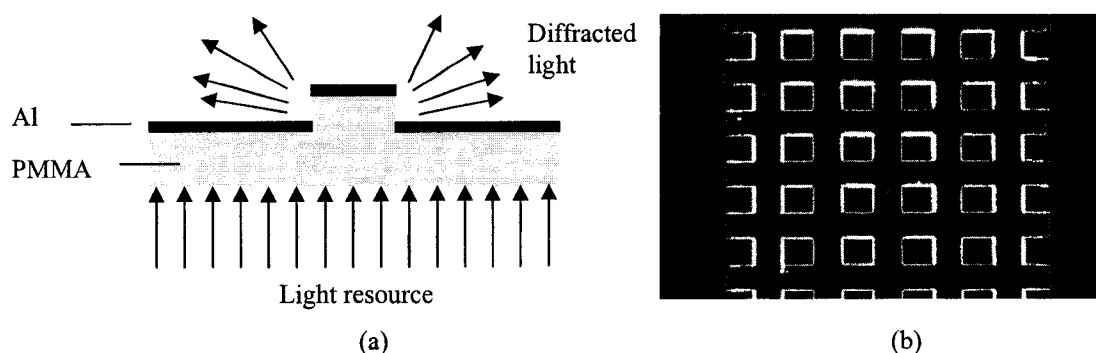
Figure 5.22 (a) Schematic illustration of inspection via optical microscopy. (b) An optical picture of a sample fabricated using the ILL.

5.11.2 EDS

In this method, a spectrum analysis of Al patterns was conducted using the software EDS2004 1.2 (IXRF Systems, Incorporate). X-ray spectra and x-ray maps were analyzed to determine the location of phase, particles, and other features on a sample that could be discriminated by variations in elemental composition [41]. In other words, the elemental distribution on x-ray maps can be seen. Figure 5.23a shows a SEM picture (taken by AMRAY 1830 from AMRAY Inc.) which was obtained from the 40-μm-high sidewall of a 300-μm-wide and 5000-μm-long line. The Al coating on this structure was 500 nm thick. The sample was titled by 60° to examine the Al distribution (Fig. 5.23b) on its sidewall. Two points can be observed from Fig. 5.23: (1) there is no Al on the bottom part of the sidewall (this part has a height of 23 μm), while Al is distributed on the top part of the sidewall (this part has a height of 17 μm), and (2) the Al located on the top of the PMMA line and the bottom of the PMMA valley still remains unbroken. These two points indicate that the part of the Al under the convex mold structures was cut off from the neighboring Al.

(a)   (b)
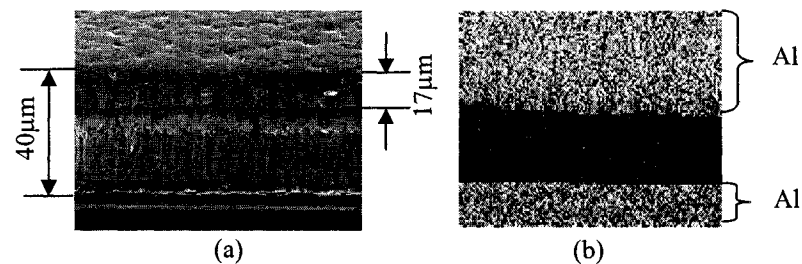
Figure 5.23 Spectrum analysis: (a) SEM picture of the 40-μm-high sidewall of a 300-μm-wide line (the structure was tilted by 60° to see the whole sidewall; Al coating was 500 nm thick), and (b) spectrum map of the Al distribution on the structure shown in (a): the light-colored area indicates that the Al exists on the top surface of a line and the valley between the two lines, while the black area implies that there is no Al on the lower part of the sidewall.

5.11.3 Measurement of Electrical Resistance

In this method, electrical resistances of metal patterns were measured using a Keithley system (Micromanipulator Company). Figure 5.24a shows the schematic of two types of measurements. In the first type of measurement, two probes were placed on the top surface of a same Al microline of a width of 300 μm, a length of 5 mm and a thickness of 500 nm (Fig. 5.24b). The distance between these two probes was about 1000 μm. The average resistance measured was 12 Ω. In the second type of measurement, the two probes were placed on the top surfaces of two neighboring lines, respectively (Fig. 5.24c). There was no current detected in this measurement. These two types of tests imply that Al on the top surface of each line remained unbroken, and that Al on the top surfaces of two neighboring lines was not connected. These results further demonstrate that the part of Al underneath the convex mold structures was cut off from the neighboring Al, and that functional Al patterns can be generated using the ILL method.
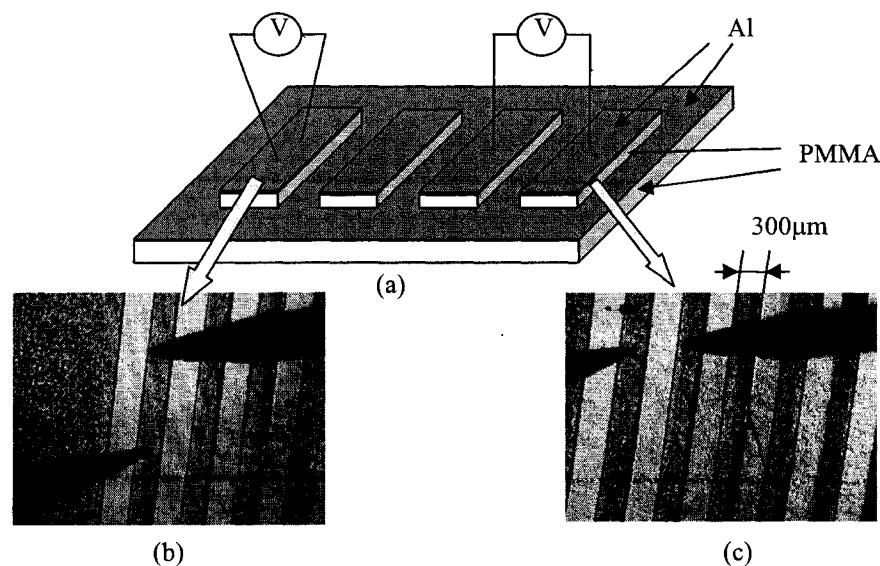
Figure 5.24 Two experimental set-up of resistance measurements: (a) schematic of these measurements, (b) the first type of measurement on a Al line of a width of 300 μm, a length of 5 mm, and a thickness of 500 nm; the distance between two probes is about 1 mm, and (c) the second type of measurement on two neighboring Al lines.

5.12 Summary

In this chapter, the ILL method was used to fabricate metal micropatterns. Various Al patterns, including channels, lines, square dots, square holes and truss structures, have been generated. The lateral dimensions of those patterns ranging from 10 to 300 μm and Al films of thickness ranging from 100 to 500 nm had been patterned by silicon molds of depths of 10 to 100 μm. The effects of imprinting temperatures, thicknesses of Al films, and geometries of silicon mold structures on the patterning results were experimentally investigated, followed by numerical exploration. As a new patterning method, the ILL approach has advantages of simplicity and massive production, and is free of aggressive chemistry. The embossing process parameters of the ILL were optimized by Taguchi methods when using a Si mold with a depth of 40 μm and a Al film with a thickness of 500 nm. Au film and free-standing Al foil were patterned using the ILL to extend its application range. Optical microscope and SEM pictures, maps of element distribution, and electrical resistance were used to examine the patterns.

CHAPTER 6

MICRO DEVICES FABRICATED USING THE ILL METHOD

6.1 Introduction

Diode and capacitor are the basic devices in IC and MEMS. There are several methods to make diodes or capacitors on silicon wafers. Top-to-bottom etching and bottom-to-top surface technology are the popular ways. Lithography, oxidation, deposition, wet and dry etching, ion implantation, and diffusion are applied to form patterns with deserved physical dimensions and electrical properties. Chemical etchant, light, ion beam, electron beam, x-ray, and high temperatures may be introduced to wafers. Poisonous chemical reagents not only do harm to human heath, but also may degrade electrical properties. High energy beams and high temperatures may result in deformation in the crystal lattice of the wafers so as to ruin the product. Moreover, expensive instruments involved in these technologies increase fabrication cost.

As potential replacements of Si-based devices, conductive polymer-based electronic devices, have high energy storage density, high capacitance, good chemical sensing capabilities, good light emission, flexibilities, low weight, and affordability. However, most conductive polymers are sensitive to the environment, and their electrical properties tend to deteriorate over time due to overoxidation (air), moisture, high temperature, and chemical alteration. The current fabrication techniques (i.e., lift-off, dry,

75

and wet etching processes) used in lithographic approaches, such as ultra-violet (UV), electron-beam, and x-ray, involve gases (for instance, oxygen and nitrogen), DI water, and/or chemical solution (such as photoresist and acetone), making them improper to pattern conductive polymers.

The ILL method has been developed to successfully fabricate metal patterns [5]. This method is simple, free of those degrading factors, and straightforward to use. Metal film with 100 – 500 nm thick which was coated on PMMA sheet was cut by Si mold to form lines, channels, dots, holes and truss structures with sizes ranging from 10 to 300 μm. In this chapter, the ILL was introduced to fabricate conducting polymer-based micro devices, for example, diodes and capacitors [8]. Multiple layers of polymers, such as polypyrrole (PPy) and Poly(3,4-ethylenedioxythiophene) poly(styrenesulfonate) (PEDOT:PSS), were coated on an intermediate layer (i.e. PMMA) and Si wafer, and then were cut through by a Si mold. No chemical reagent or high energy beam was involved in this work.

6.2 Fabrication and Characterization of PPy/PEDOT Heterojunctions

Two kinds of conducting polymers, PEDOT:PSS (Baytron Co.) and PPy (Aldrich Co.) in the form of aqueous solutions, were used in the fabrication of conducting polymeric_heterojunctions. A commercial PMMA sheet (Cyro Co.) was chosen as the intermediate layer, since PMMA has been demonstrated as a good hot embossing material. [15,16] The PMMA sheet was 500 μm thick, 170 mm wide, and 170 mm long. Both PEDOT and PPy are conjugated polymers [42]. PPy is an environment-stable, p-type, and semiconducting polymer. PEDOT:PSS is also highly conductive with a p-type

semiconducting property. The electrical conductivity of highly doped PEDOT:PSS [43] and PPy [44] about 200 S/cm and 10 to 40 S/cm, respectively. The interface between p-type PEDOT and p-type PPy is a heterojunction. PMMA is a good electrical insulation material. Its electrical resistivity is 1×10^{19} Ω.mm²/m [45]. Figure 6.1 shows the chemical molecular structure of PPy, PEDOT:PSS and PMMA [42].

(a)   (b)   (c)
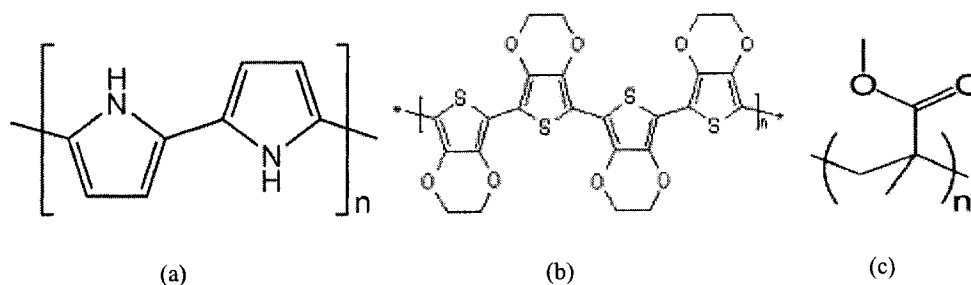
Figure 6.1 Chemical molecular structure of (a) PPy, (b) PEDOT:PSS, and (c) PMMA [42].

Figure 6.2 gives the procedure of using the ILL method to fabricate PPy/PEDOT heterojunctions. A PMMA sheet was placed on a 4-in Si wafer. A 10-μm-thick PEDOT layer and a 1-μm-thick PPy film were spin-coated on the PMMA sheet, respectively (Fig. 6.2a). Before the coating of PEDOT, the PMMA sheet had been treated by oxygen plasma in a reactive ion etching system, Micro-RIE series 800 (Technics Inc.), for 5 min to increase the adhesion to the PEDOT. The PEDOT layer was a little wider than the PPy film. The extra PEDOT space (compared with the PPy film) was used for ground contact.

The spin-coated film was first baked on a hot plate at 85° C to remove solvent and then cooled down slowly for minimizing thermal deformation. The baking duration was about 60 min for the 10-μm-thick PEDOT film and 5 min for the 1-μm-thick PPy layer. The imprinting was performed on a hot embossing system, HEX 01/LT (JENOPTIK Mikrotechnik Co.). The speed of mold insertion was 10 mm/min, the embossing pressure

was 1.5 to 3 MPa, the imprinting temperature was 140 to 150° C, and the demolding process was performed at 85 to 95° C with a speed of 1 mm/min. When the polymers were heated over T_g of PMMA and lower than that of PPy (169° C), a Si mold was inserted into them. It was reported that PEDOT doped with PF_6^-, BF_4^-, and $CF_3SO_3^-$ decomposed between 390 and 450° C [46]. It is observed that PEDOT:PSS remained in the solid phase up to the temperature of around 400° C. PPy and PEDOT are hard at the imprinting temperature, while PMMA is softened. The parts of the PPy film, respectively, under convex or concave structures of the Si mold, were separated from each other due to the insertion of the Si mold. Meanwhile, the PEDOT layer was deformed but not broken. The part of the PEDOT film under the convex structures was pushed down, and that part under the concave structures (cavities) flew up to fill the empty cavities (Fig. 6.2b). After the sample was cooled down below T_g of PMMA followed by the removal of the Si mold, desired PPy/PEDOT heterojunctions were fabricated (Fig. 6.2c).
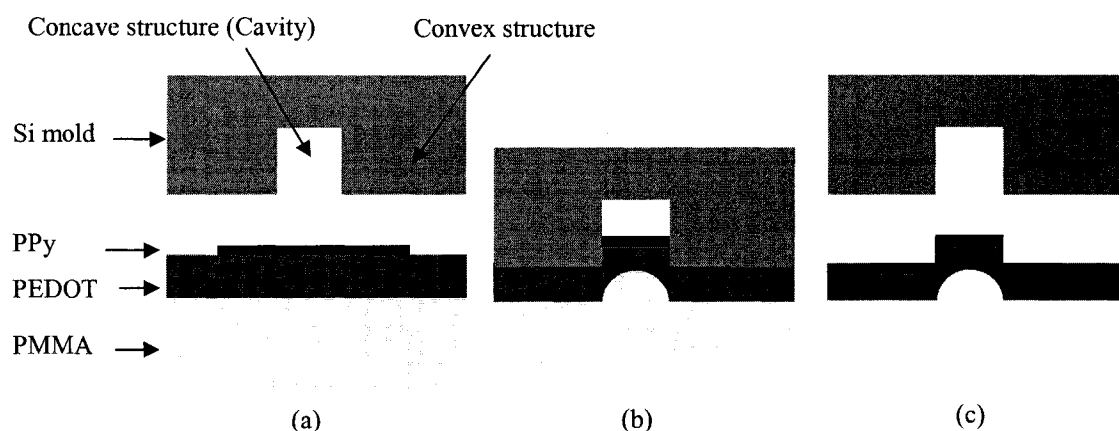
Figure 6.2 The procedure of employing the ILL method to fabricate PPy/PEDOT heterojunctions: (a) coat PEDOT and PPy on a PMMA sheet, (b) heat and apply hot embossing with the aid of a Si mold, and (c) cool down and release Si mold.

6.2.1 Geometry of PPy/PEDOT Heterojunctions

Figure 6.3 shows two examples of diodes fabricated using the ILL. One has the form of a square with dimensions $20\times300\times300$ μm^3 (Fig. 6.3a). The other has a shape of a microline with dimensions $20\times300\times5000$ μm^3 (Fig. 6.3b). In order to make a PPy/PEDOT heterojunction using the ILL, the top PPy layer should be cut off at the Si-mold edges while the PEDOT should be connected (Figs. 6.3c and d). A thin PEDOT layer might be cut off along with PPy, as shown in Fig. 6.4a for the case of a 4-μm-thick PEDOT film. Hence, a thick PEDOT layer (10 μm) is adopted as the bottom layer which serves as a common ground electrode for the generated heterojunctions. On the other hand, thick PEDOT results in slantwise sidewalls (Figs. 6.3c and d). The embossing pressure was 1.5 to 3 MPa. Vertical sidewalls might be formed if higher imprinting pressure (larger than 3MPa) were used. However, it was found that at such a high imprinting pressure, the Si mold may stick to the PMMA sheet. In addition, the Si molds had low depths, since deep depths might cause the PPy layer (even PEDOT) to collapse (Fig. 6.4b). Empirical ratios of mold depth to the thickness of PPy range from 5 to 10.
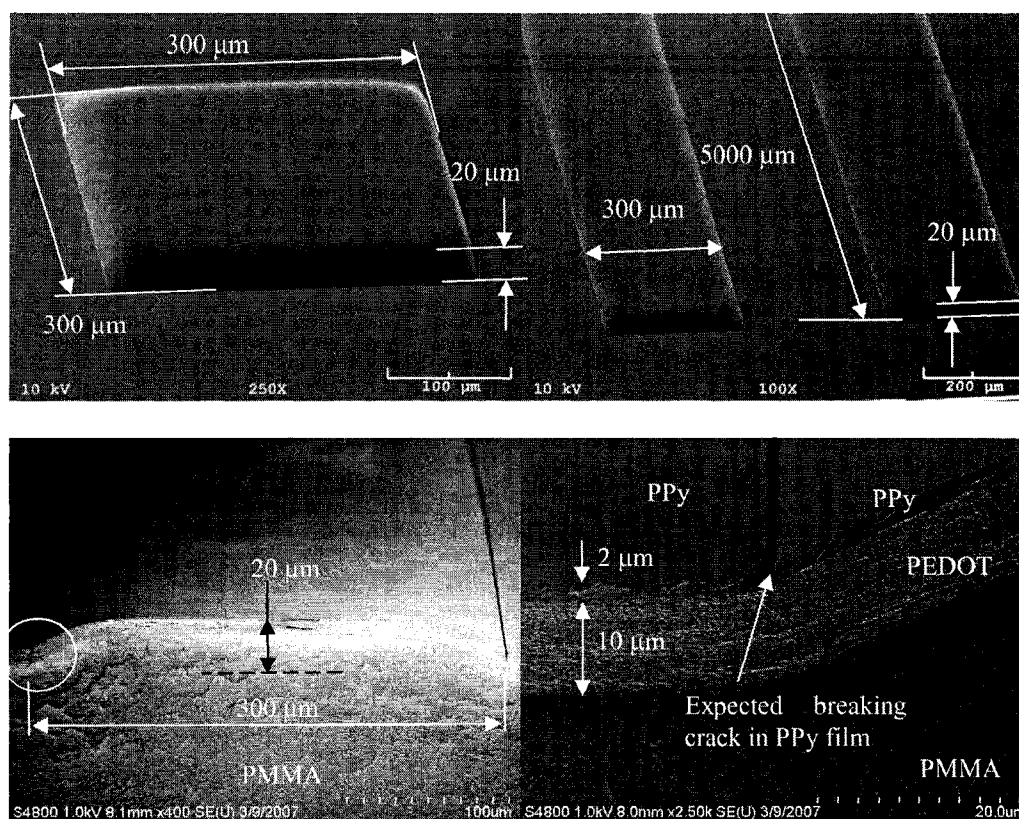
Figure 6.3 SEM pictures of heterojunctions fabricated using the ILL. (a) A block with dimensions 20×300×300 μm³; (b) microlines with dimensions 20×300×5000 μm³; (c) cross section of a microline; (d) close-up view of (c). The PPy layer was cut off at edges as expected.

Another interesting point was that the top PPy film was cut off at the mold's edges as expected, even if the polymers did not fill the mold cavity completely. Low imprinting temperature (below 130° C), low imprinting pressure (less than 1 MPa), or narrow cavity of mold (e.g., the width and depth of a Si mold were 50 and 20 μm, respectively, and the thickness of PEDOT layer was 10 μm) may cause incomplete filling of the polymers into the cavity of the Si mold. Figure 6.5 gives such an example. The polymers in the device areas were curved. The PPy layer broke at the edges of the Si mold. There was a 1.5 μm distance between the two separated parts of the PPy at the breaking point.

(a)

(b)
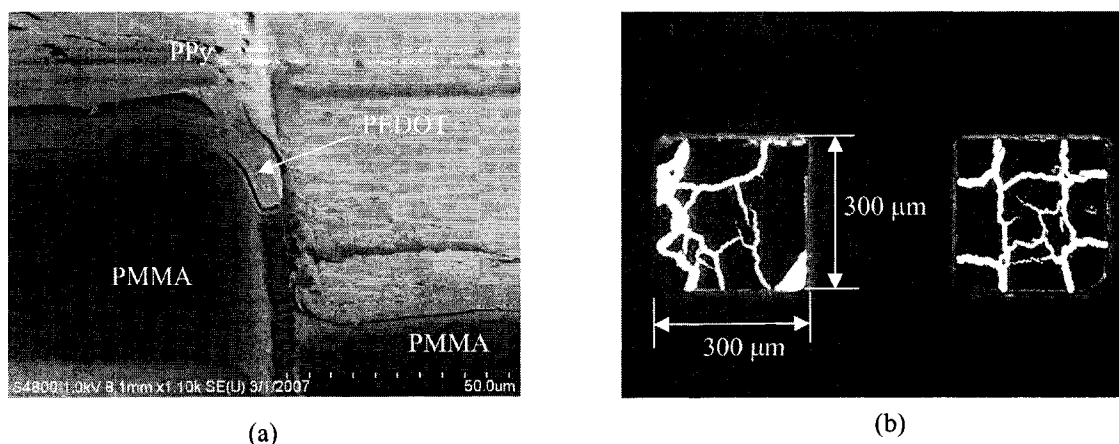
Figure 6.4 Improperly fabricated devices. (a) Both of the 1-μm-thick PPy and 4-μm-thick PEDOT films were cut through by the Si mold (SEM image). (b) PPy and PEDOT films cracked in microblocks fabricated using a Si mold whose depth was 65 μm. Black and white areas stand for the polymer films and cracks, respectively (Optical picture).

(a)

(b)
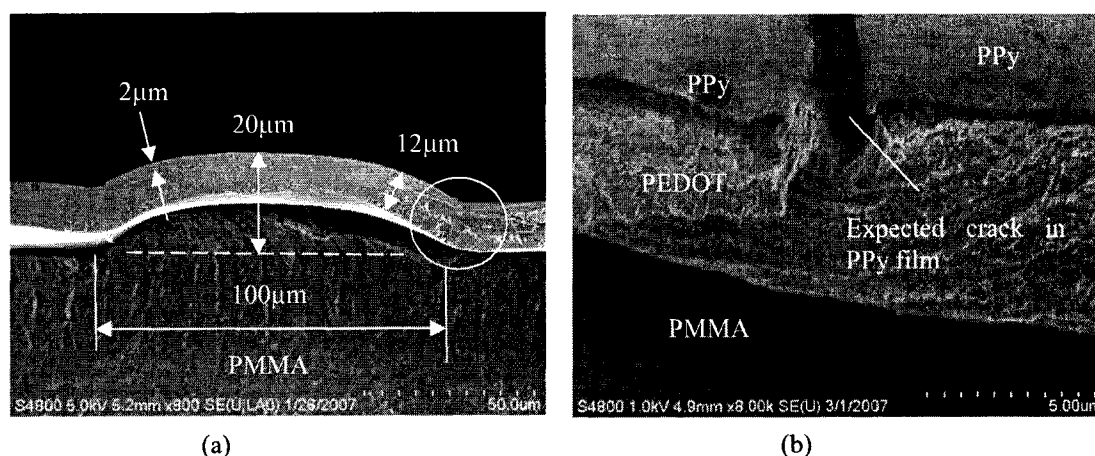
Figure 6.5 (a) SEM pictures of cross section of a microline fabricated at 130° C. (b) Close-up view of (a).

6.2.2 Characterization of a PPy /PEDOT Heterojunction

The electrical characterization was carried out in a Keithley test system (Keithley Inc.). The PEDOT and PPy layers were, respectively, connected to the Keithley system through highly conductive Ag glue and copper wires. The PEDOT electrode was at ground, and the bias voltages varied from -20 V to 20 V at the PPy electrode. The

measured *I-V* curve of a representative PPy/PEDOT heterojunction at room temperature is given in Fig. 6.6.

Liu and Cui [47] reported two Poly[2-methoxy-5-(2-ethylhexyloxy)-1,4-(1-cyano-vinylene) phenylene] (CN-PPV) based diodes. The breakdown voltages of a CN-PPV/PPy and CN-PPV/PEDOT diode were -6 and -5.4 V, respectively. The rectification ratio was 117 at 2 V for the CNPPV/ PPy diode and 26 at 2.5 V for the CN-PPV/PEDOT diode. From Fig. 6.6, the forward and reverse breakdown voltages of the PPy/PEDOT heterojunction were 5 and -8 V, respectively. The rectification ratios were 24 at 10 V. These measured quantities were close to those of the CN-PPV based diodes.

(a)   (b)   (c)
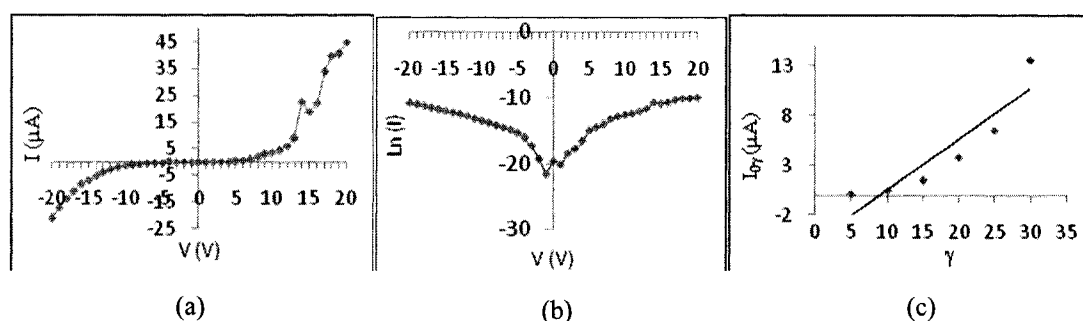
Figure 6.6 (a) The I-V characteristic of the PPy/PEDOT heterojunction. (b) The forward and reverse bias ln(I)-V characteristic of the heterojunction. (c) $I_{0\gamma}$-γ relationship for finding R_s and n.

In a conducting polymer, the charge carriers transport between ordered regions ('crystalline islands') through disordered regions by hopping or tunneling [48]. Hence, the band transport theory, which is widely used in inorganic semiconducting devices, does not apply to conducting polymer devices. The parameters of this heterojunction were found using the standard thermionic emission theory of the Schottky barrier model, which applies to heterojunctions as well. It was assumed that the current was only controlled by the transport of carriers across the junction, and the drift and diffusion

carriers within the depletion region were unimportant. According to the thermionic emission theory,

$$I = I_s \exp\left(\frac{qV_d}{nKT}\right),$$

(6.1)

where I_s is the saturation current, V_d is the voltage drop across the diode, n is the ideality factor, K is the Boltzmann constant (1.38×10^{-23} J/K), q is the elementary charge ($1.60217646 \times 10^{-19}$ C), and T is the operational temperature. In Equation (6.1), V_D is the voltage across diode and is determined by

$$V_D = V - IR_s$$

(6.2)

where V is the applied voltage, and Rs is the series resistance of the heterojunction. Also,

$$I_s = AA^*T^2 \exp\left(\frac{-q\Phi_B}{KT}\right),$$

(6.3)

where A is the surface area of the diode (0.015 cm^2), A^* is the effective Richardson constant (120 A/K^2-cm^2), and Φ_B is the barrier height. Extrapolating the semilog forward and reverse I-V characteristics, the forward and reverse saturation current densities were 16.7 and 10.3 μA/cm^2, respectively. Using these values, the forward and reverse barrier heights were calculated as

$$\Phi_B = \left(\frac{KT}{q}\right)\ln\left(\frac{J_s}{A^*T^2}\right).$$

(6.4)

The forward barrier height was 0.70 eV, and the reverse barrier height was 0.71 eV. These values are comparable to those of PPy/p-type Si heterojunctions, which are 0.57 to 0.72 eV [49,50].

Because the conducting polymers are low conductive, the I-V characteristic

showed that the PPy/PEDOT heterojunction had a high series resistance. The modified

Norde function method [51,52] was used to determine Rs, and n.

$$G_\gamma(V,I) = \frac{V}{\gamma} - \frac{kT}{q}\ln\left(\frac{I}{A^*AT^2}\right),$$ (6.5)

where γ is a dimensionless arbitrary integer. The V and I in Equation (6.4) are related by

the I-V characteritic. For each possible value of γ, there exists a value of the current, $I_{0\gamma}$

(say), which makes $G_\gamma(V,I)$ have the minimum value. For a particular value of γ, this $I_{0\gamma}$

can be obtained via $G_\gamma(V,I)$-I plot. Mathematically, $I_{0\gamma}$ satisfies

$$\left.\frac{dG_\gamma(V,I)}{dI}\right|_{I=I_{0\gamma}} = \left.(\frac{1}{\gamma}\frac{dV}{dI} - \frac{kT}{qI})\right|_{I=I_{0\gamma}} = 0.$$ (6.6)

With the aid of Equations (6.1) and (6.2), it follows from (6.6) that

$$I_{0\gamma} = \frac{kT(\gamma-n)}{qR_s}.$$ (6.7)

Figure 6.6c is the $I_{0\gamma}$-γ curve calculated using Equation (6.5). According to

Equation (6.6), the plot of $I_{0\gamma}$-γ is approximate a straight line, whose slope leads to the

value of the series resistance Rs and whose extrapolated intercept at $I_{0\gamma}=0$ gives n. Based

on this straight line and Equation (6.7), it was found that $R_s=51.6$ kΩ and $n=$ 8.88. The

ideality factor should be between 1 and 2. Hence, the ideality factor of this PPy/PEDOT

heterojunction is high. A PPy/p-type Si heterojunction was reported to have the high

ideality factor of 6.72, too [49]. However, the reason for getting a high ideality factor is

not clear yet. A possible explanation may be conduction contributed by carrier

recombination and tunneling across the depletion region. Also the conductivity of the

polymer exerts substantial influence on the barrier formation.

6.3 Fabrication and Characterization of Al/PEDOT Diodes

The structure and fabrication process of Al/PEDOT diode are similar with their counterparts of the PPy/PEDOT heterojunction. A thin Al film was used to replace the PPy layer. Low-conductive PEDOT (Aldrich Co.), which conductivity is 1×10^{-5} S/cm, instead of high-conductive PEDOT, was used as the ground layer. The junction between Al and p-type semiconducting PEDOT was a Schotty diode.

The fabrication procedure is briefed as follows: a PMMA sheet was placed on a 4-in Si wafer. A 10-μm-thick PEDOT was spin-coated on the PMMA sheet. A 200-nm-thick Al film was deposited on the top surface of the PEDOT layer via thermal evaporation using a metal evaporator, DV-502A (Denton Vacuum Inc.), followed by the hot embossing process. When the Si mold was pushed down, the thin Al film was cut through. The parts of the Al film under convex and concave structures of the Si mold were separated from each other after the mold insertion. Meanwhile, the PEDOT layer was deformed but not broken. The part of the PEDOT film under convex structures was pushed down and that under concave structures (cavities) flew up to fill the empty cavities.

Figure 6.7 shows Al/PEDOT diode fabricated using the ILL. Imprinting conditions were the same as those for the PPy/PEDOT heterojunction. The thin Al film on the top of the PEDOT was cut through as expected. Because the PEDOT layer was thick, the sidewall was not vertical.

The standard thermionic emission theory of the Schottky barrier model was used to analyze Al/PEDOT diode. The analysis procedure was the same as that in Section 6.2.2. It was assumed that the current was only controlled by the transport of carriers

across the junction and the drift and diffusion carriers within the depletion region were unimportant.

(a) (b)
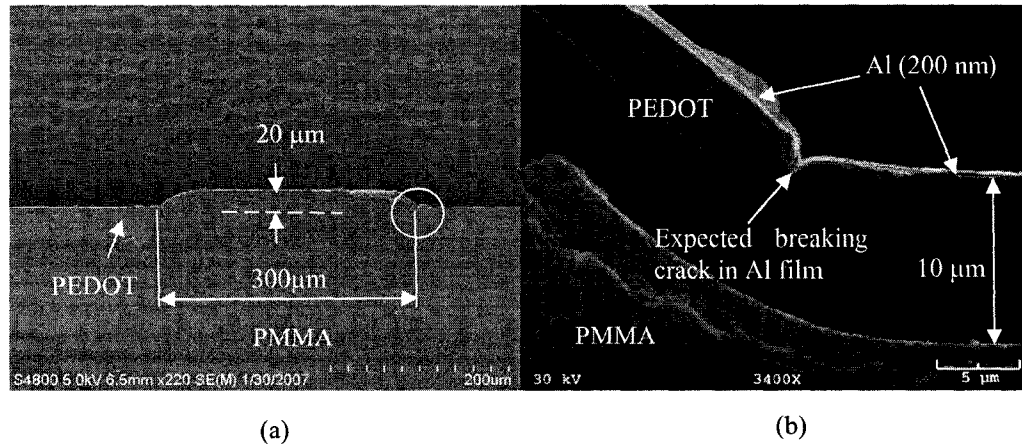
Figure 6.7 SEM picture of Al/PEDOT diode fabricated using the ILL. (a) Cross section of a microline with 300 μm thickness. (b) Close-up view of (a).

Figure 6.8 shows the *I-V* curve of a representative Al/PEDOT junction, which was measured at room temperature. The Al electrode was at ground and the voltage varied from -5 to 5 V. It was observed from this figure that the forward and reverse breakdown voltages were 3 and -2.5 V, respectively. Rectification ratio of the Al/PEDOT diode was 2 at 1 V.

(a) (b)
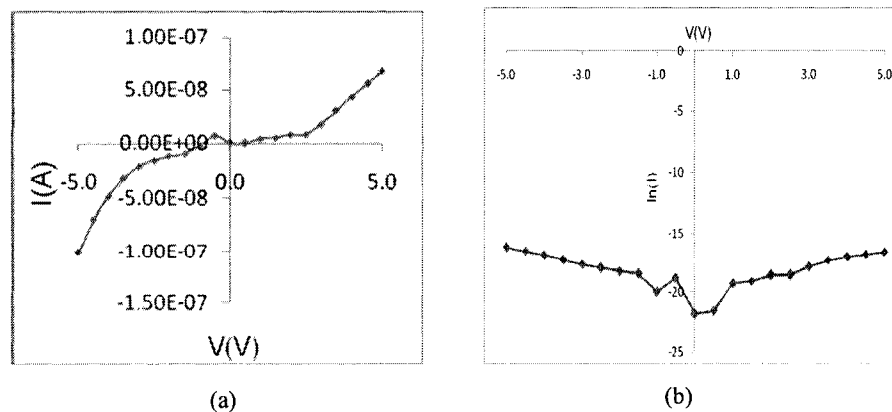
Figure 6.8 (a) The *I-V* curve of the Al/PEDOT junction. (b) The forward and reverse bias *ln(I)-V* characteristics of the junction.

Extrapolating the semilog forward and reverse I-V characteristics, the forward and reverse saturation current densities were 0.19 μA/cm^2 and 0.31 μA/cm^2, respectively. The forward and reverse barrier heights were found to be 0.81 and 0.82 eV, respectively. According to equation (6.3) - (6.7) and with the help of Fig. 6.8b, the ideality factor for this junction was calculated to be 19. A similar Al/PPy diode was reported by Liang et al. [50]. The breakdown voltage and rectification ratio of the Al/PEDT diode were about 5.5 V. The ideality factor was 1.42, and the barrier height was 0.97 eV. In comparison to the two Al/PEDOT diodes, those parameters are close except for the ideality factor.

6.4 Fabrication and Characterization of PEDOT/PMMA/PEDOT

Capacitors

The fabrication procedure of polymeric capacitors using the ILL (Fig. 6.9) is similar to that of the PPy/PEDOT heterojunctions. A PMMA layer was sandwiched between the two PEDOT films. Meanwhile, it served as an electrical insulation layer in the capacitor due to its good insulation property. It functioned as the intermediate layer in the ILL. The two high conductive PEDOT layers were the electrodes of the capacitor. PEDOT, PMMA, and PEDOT layers were spin-coated on a PMMA sheet (which functioned as the substrate and the intermediate layer) (Fig. 6.9a). The top PEDOT layer was relatively thinner, and the bottom was thicker. Subsequently, the ILL was applied to fabricate desired patterns (Fig. 6.9b and c). The imprinting temperature and pressure were 140° C and 3 MPa, respectively.
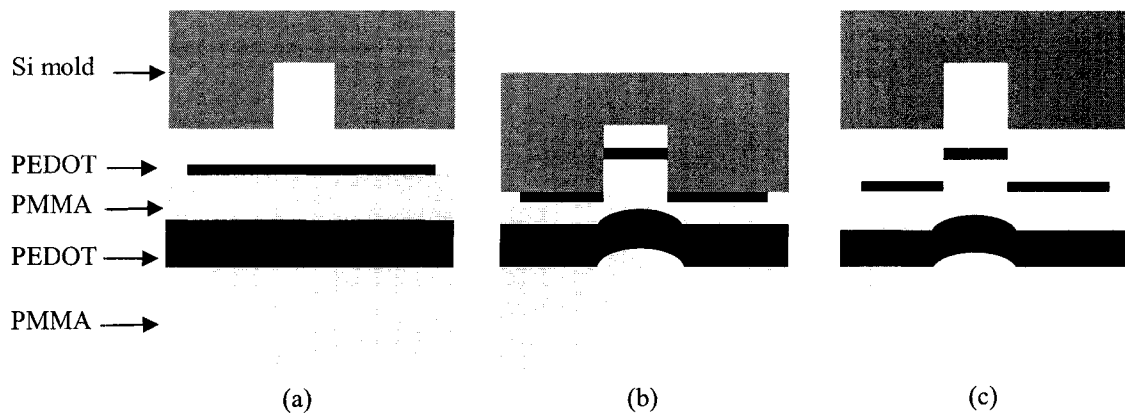
Figure 6.9 The fabrication procedure of the PEDOT/PMMA/PEDOT capacitor using the ILL: (a) PEDOT, PMMA, and PEDOT layers were spin-coated on a PMMA sheet, respectively. (b) Hot embossing was applied with insertion of Si mold. (c) Si mold was released.

Figure 6.10 shows a cross section of a PEDOT/PMMA/PEDOT capacitor. The top thinner PEDOT layer was cut through as in the cases of references 1 and 2. The thicker bottom PEDOT layer was pushed up into the mold cavity to be embowed by the PMMA substrate, which was softened during the ILL. The rubber-like PMMA layer, which was sandwiched between the two PEDOT layers, was squeezed and filled into the mold cavity completely. Its thickness was not uniform.

Heavily doped PEDOT:PSS layers functioned as the metal plates in the common metal parallel plate capacitor. The charges accumulated at the interfaces between the conducting polymer and insulator layer (i.e., PMMA) when bias voltages were applied onto the device. In conducting polymers, solitons, polarons, and bipolarons behave as charge carriers [51], while free electrons or holes do so in metals or semiconducting materials (i.e., Si, Ge or GaAs) [52]. Unlike the free electrons in metal, the charge carriers in conducting polymers transport between ordered regions ('crystalline islands') through disordered regions by hopping or tunneling. Hence, charge mobility in a polymer

capacitor is much lower than that in a common metal parallel-plate capacitor. According

to the definition of capacitance, $C = \dfrac{Q}{V}$, the capacitance of the polymer capacitor is lower

than the theoretically calculated value of a metal parallel-plate capacitor [51]. The $C-V$

characteristic of a representative capacitor fabricated using the ILL was measured by the

Keithley system at room temperature. As shown in Fig. 6.11, the $C-V$ curve was almost a

straight line, which was similar to that of a metal parallel-plate capacitor. The variation

and peaks in the lines might result from the fabrication process, such as the non-uniform

surfaces of polymers, contamination, or void in materials. The measured capacitance of

the capacitor at low frequency bias was about 0.06 pF, while the theoretically calculated

quantity was 1.38 pF.

(a)   (b)
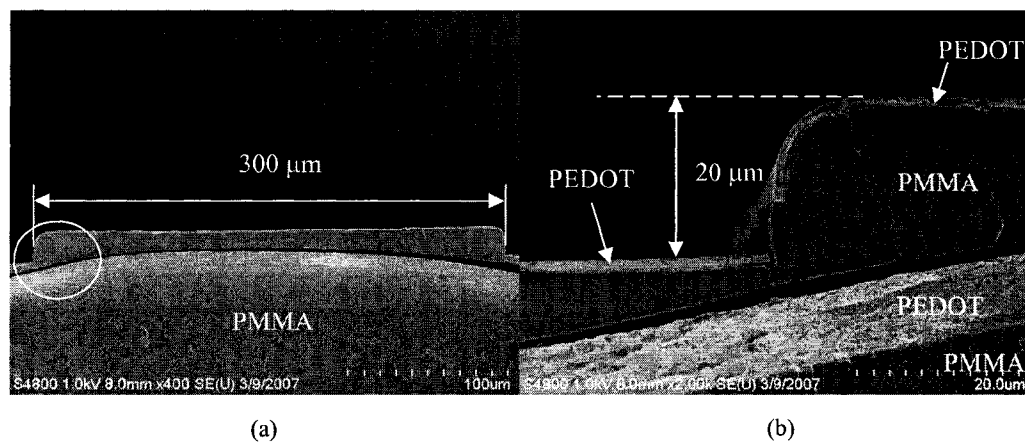
Figure 6.10 Cross section of a PEDOT/PMMA/PEDOT capacitor. The PEDOT, PMMA and PEDOT layers are about 10, 12 and 1.5 μm thick, respectively. (a) Cross section of a microline with a thickness of 300 μm. (b) Close-up view of (a).
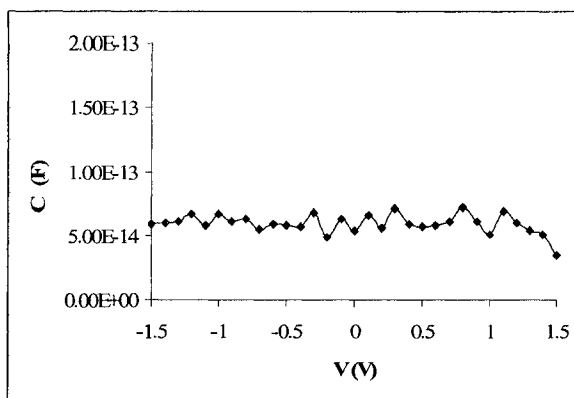
Figure 6.11 *C-V* curve of a representative PEDOT/PMMA/PEDOT capacitor.

6.5 Summary

PEDOT/PPy heterojunctions, Al/PEDOT diodes and PEDOT/PMMA/PEDOT capacitors were developed using the ILL. The geometry of the Si mold, the thickness of the polymer (or metal) film, and imprinting temperature are important parameters to fabricate good devices. Low imprinting temperatures, low applied force, and narrow cavity of mold may cause incomplete filling of PMMA into the mold cavity. The critical electrical characteristics (e.g., breakdown voltage and rectification ratio) of representative PEDOT/PPy heterojunctions and Al/PEDOT diodes were found close to the values reported in the literatures. High ideality factor of the Al/PEDOT diode was observed. The reason was not clear. The *C–V* curve of a representative PEDOT/PMMA/PEDOT capacitor was almost a straight line, which was similar to that of a typical parallel metal-plate capacitor. Because the charge carrier in a conducting polymer had lower mobility than that in a metal or semiconductor, measured capacitance of the capacitor, which is 0.06 pF, was much lower than the theoretically calculated value, which was 1.38 pF.

CHAPTER 7

FABRICATION OF METALLIC NANOWIRES

7.1 Introduction

Since the concept of nanotechnology was first defined in the 1970s, nanotechnology has attracted a huge number of researchers due to the special 'quantum effect' of nano structure and nano materials and the potential applications in medical, chemical, and IC industries. A nanowire is a tiny wire with at least the diameter less than 1 micrometer (10^{-6} meters), generally in the range from 0 to 100 nm. There are different nanowires, such as metallic (e.g., Ni, Pt, Au), semiconducting (e.g., Si, InP, GaN, etc.), insulating (e.g., SiO_2, TiO_2) and molecular nanowires (e.g., DNA) [42]. The potential applications of nanowires could be field-effect transistors [53], sensors [54], and light-emitting diodes [55]. This is because of their unique geometry and many unique physical properties, including electrical, magnetic, optical, as well as mechanical properties.

The minimum wavelength of UV light is about 200 ~ 300 nm, which compares to the size of a nanowire. Hence, metallic nanowires (MNWs) can not be generated using traditional lithography technique. Currently, the major approach to fabricate MNWs is electrochemical deposition with different templates, including negative, positive, and surface-step templates. The negative-template method uses prefabricated nanopore

91

membranes as templates [56,57]. Nanowires with the same diameter as the nanopores are fabricated by depositing metals into the nanopores. The positive template method uses linear nanostructures, such as DNA [58] and carbon nanotubes [59], as templates to guide electrodeposition on the surface of the templates. The diameters of the nanowires are controlled by the quantity of material deposited on the templates. Surface step edges on crystal surfaces can be used as templates to grow nanowires [60]. The process is based on the fact that electro deposition often starts preferentially along surface step edges. Electrochemical etching is contrary to the deposition. The width of the nanowire is controlled flexibly by etching atoms away or depositing atoms back onto the wire with the electrochemical potential [61]. The major challenge of both electrochemical deposition and etching is to generate MNWs with stable and uniform dimensions.

The third method is the local-probe method, which uses a local probe, such as the tip of a scanning tunneling microscope (STM) [62] or an atomic force microscope (AFM) [63], in close proximity to a metal or semiconductor surface to induce localized electrochemical deposition and etching. The local-probe method creates structures one at a time, so it is not suitable for mass-production of nanostructures.

In previous chapters of this dissertation, metal micropatterns and conducting polymer-base microdevices were fabricated using the ILL. One major advantage of the ILL method is that it is not constrained by light wavelength. That means, nanopatterns could be fabricated using this method.

7.2 Experiments and Discussions

7.2.1 Fabrication of Nano Molds

The minimum wavelength of UV light is about 200 ~ 300 nm. The minimum size of features fabricated using photolithography is limited to be 200 nm. Thus, the nano molds can not be fabricated using traditional UV-lithography approach. In this work, the focus ion beam (FIB) milling technique was selected to make nano molds which were used in the ILL method.

FIB is a powerful tool to fabricate nano patterns. The basic structure and principle of the machine is similar to those of SEM, which was discussed in Section 3.4. Ions are generated, accelerated, and focused inside the Magnum ion column. The ions striking the surface of the sample also generate secondary electrons and ions. These secondary electrons or ions are detected and processed to form an image of the area on the sample that was scanned by the ion beam (i.e., ion beam microscopy). The scan control system enables milling of specified patterns into the sample. When the ions hit the sample surface, not only secondary electrons are emitted, but due to their mass, sample materials are also removed. The amount of material that is removed depends on the intensity of the ion beam and the time of the exposure [64]. Therefore, FIB can directly 'write' patterns using focus ion beam.

Figure 7.1 and 7.2 shows pictures of the Si nano molds used in this work, which were fabricated using FIB etching technique by Applied Nanostructures Company.

(a)

(b)

(c)

(d)
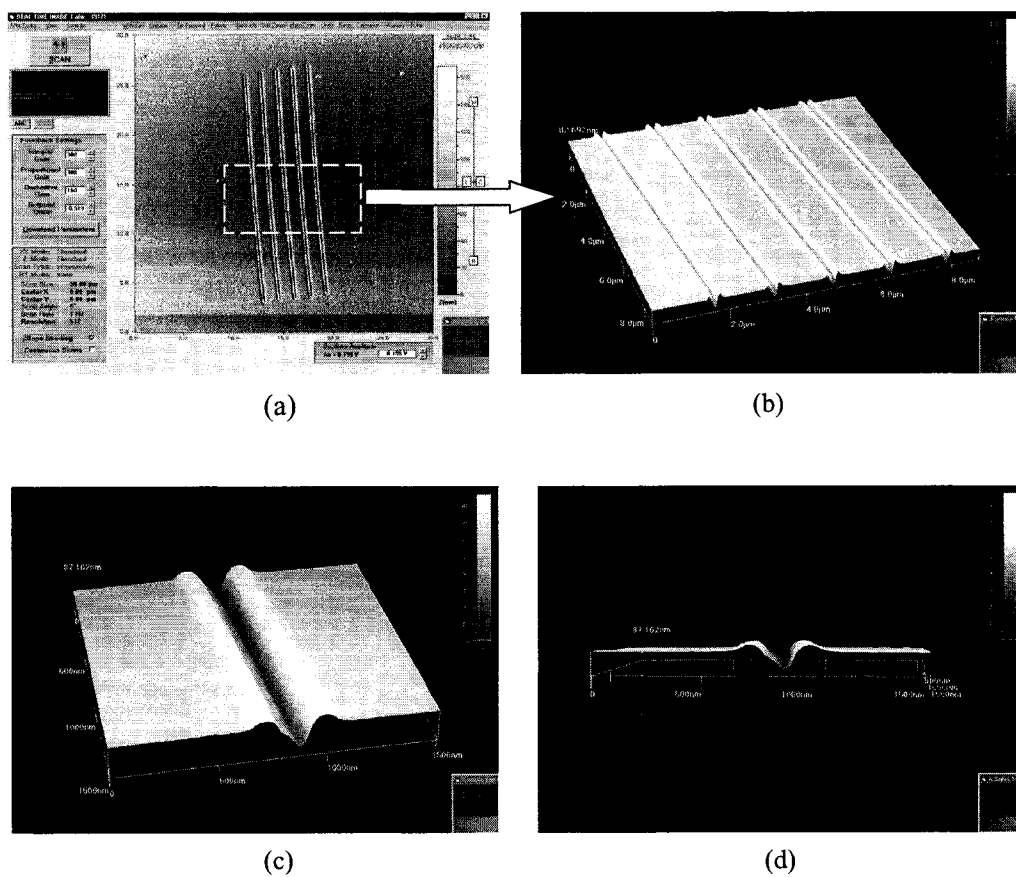
Figure 7.1 AFM pictures of a silicon nano mold. The trenches of the mold have 100 nm width and 20 μm length. (a) The overview of the pattern. (b) Close-up view of (a). (c) One trench. (d) The cross-section of a trench.

(a)

(b)

(c)

(d)
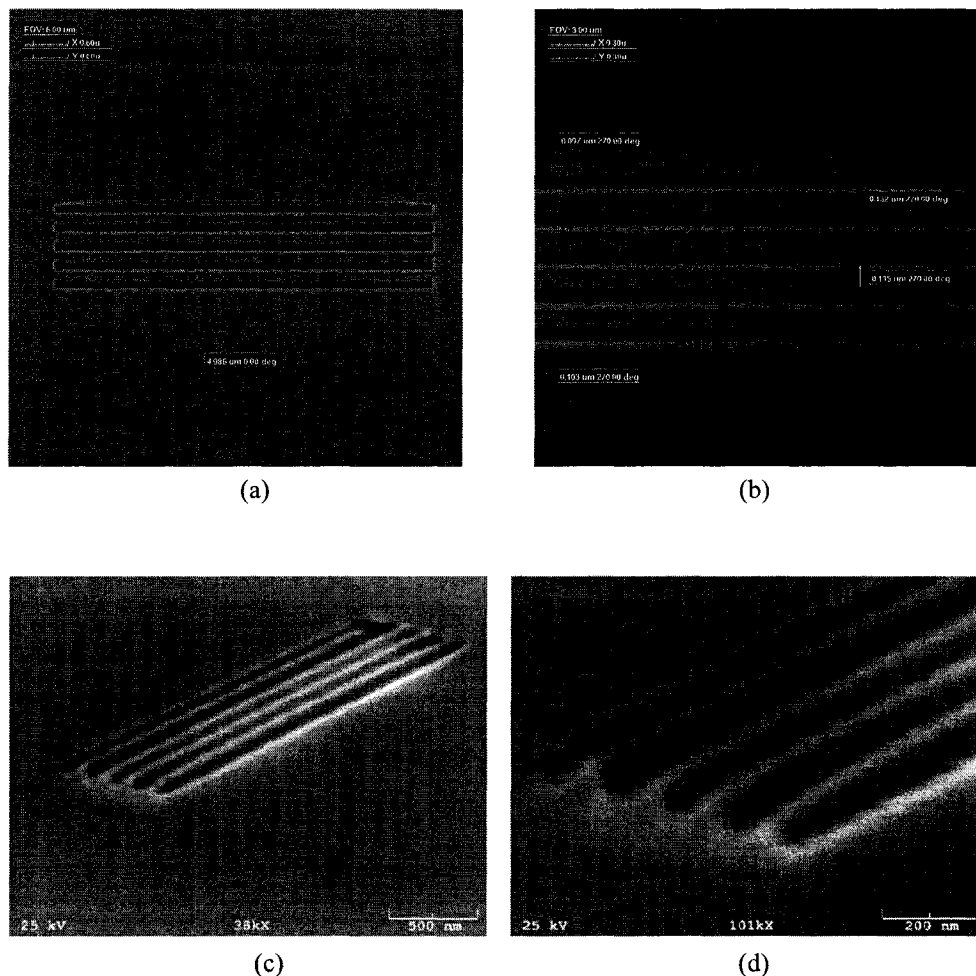
Figure 7.2 SEM pictures of a silicon nano mold. The trenches of the mold have 100 nm width and 5 μm length. (a) The overview of the pattern. (b) Close-up view of (a). (c) 3D effect. (d) Close-up view of (c).

7.2.2 Experimental Procedure

A layer of PMMA (MW=495k, MicroChem Co.) film was spin–coated on a 4-in Si substrate with 500~1000 rpm. The corresponding thickness is around 20 ~ 10 μm. Then, a layer of 10 ~ 25 nm Au film was deposited on the PMMA film in a sputter (Cressington Co., 208HR). Hot embossing was performed in a commercial hot embossing system HEX 01/LT (JENOPTIK Mikrotechnik Company). The force-control mode was adopted to keep enough pressure on the PMMA. In this work, the mold insertion speed

used was 1 mm/min, the embossing pressure was 2 ~ 3 MPa, the holding duration was

600 - 800 sec, the de-molding process was performed at 95° C with a speed of 3 mm/min,

and the imprinting temperature ranged from 160 to 175° C.

Table 7.1 Hot embossing recipe and its explanation for nano patterns

Command	Explanation.
Initialize force control [true/false]=1	Basic force unit is initialized.
Temperature [Top=90 deg, Bottom=90 deg]	Starts heating of substrate and embossing tool.
Close Chamber []	Closes the vacuum chamber.
Evacuate Chamber []	Evacuates the vacuum chamber.
Wait time [time=20 s]	Wait.
Show chart window [Show/Hide=11/0]	Displays the graphical view of the parameter change.
Touch Force [Force=50 N]	The tool, when in contact with the substrate, applies an initial force of defined limit for efficient heat transfer.
Wait time [time=20 s]	Wait.
Heating [Top=140 deg, Bottom=140 deg]	Heats the tool and the substrate to the process temperature.
Temperature >= [Temperature=105 deg, Channel=10);	Heats until the temperature of the tool and the substrate assembly reach the desired temperature.
Wait time [time=10 s]	Wait.
Heating [Top=160 deg, Bottom=160 deg]	Heats the tool and the substrate to the process temperature.
Wait time [time=60 s]	Wait.
Force-Force controlled (Force=2300 N, velocity=1.0000 mm/min);	Applies a force of 2300N for molding.
Wait time [Time=600 s]	Sets the holding duration.
Cooling [Top=60 deg, Bottom=60 deg]	Starts cooling the substrate and the tool assembly.
Wait Time [Time=50 s]	Wait.

Temperature <= [Temperature=95 deg, channel=10]	System waits until the temperature falls down to 95° C.
Wait Time [Time=50 s]	Waits for the temperature to stabilize.
Demolding Adv [Stretch=1.5 mm, velocity = 1.0 mm/min]	Demolds tool and the substrate. Demolding takes place at a set speed.
Venting []	Vents the chamber.
Open chamber []	Opens the chamber.
Show chart window [Show/Hide = 01/0]	Hides the chart which displays the graphical view of the embossing parameters with respect to time..

The ILL method has been applied successfully to generate Au nanowires with a width of 50, 100, and 500 nm, respectively. Figure 7.3 shows an example with a width of 100 nm. These experimental results indicate that the ILL method can be potentially used to generate metal patterns commonly used in the nanoelectromechanical systems (NEMS) field.

(a)

(b)

(c)
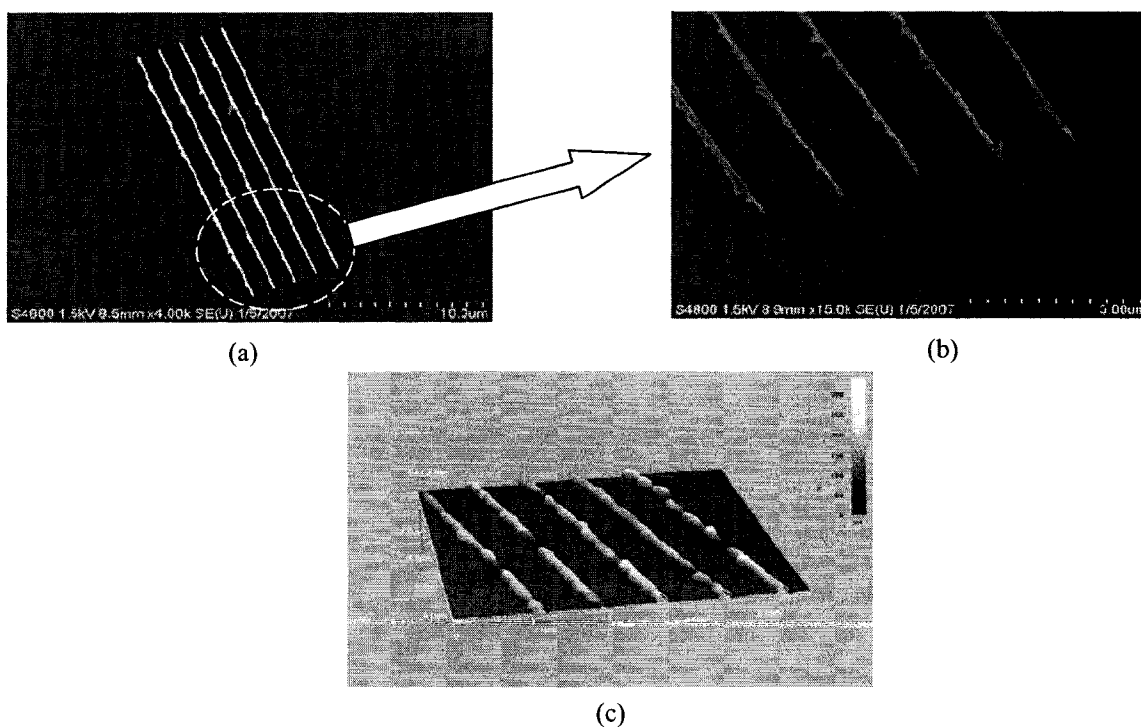
Figure 7.3 Au nanowires patterned using ILL method, which have 100 nm width and 20 μm length. (a) SEM picture of overview. (b) Close-up view of (a). (c) AFM picture to show the 3D profile of the pattern. The thickness of Au film is 20 nm.

It was discussed in Section 5.7 that micropatterns with high aspect ratio may cause Al film collapse due to large stress. Based on the same principle, nanowires with a high aspect ratio may suffer the same situation as their micro counterparts. Figure 7.4 shows such an improper nano pattern. In this case, the width of nanowires was 100 nm, and the mold depth was 1500 nm.
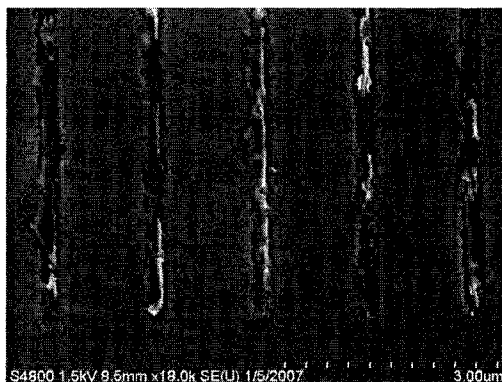
Figure 7.4 Improperly fabricated Au nanowires due to high aspect ratio. The thickness of Au film was 20 nm. The width of nanowires was 100 nm and mold depth was 1500 nm.

An interesting observation in the generation of Au nanowires using the ILL method is 'dual-peak' wire (Fig. 7.5). The 'dual-peak' phenomenon was never observed when trying to fabricate micro patterns using ILL, although Rowland et al. reported dual peak deformation of polymers in their microembossing process [65]. It is indicated in this work that high temperatures and short holding duration may cause 'dual-peak' nanowires. Actually, 'dual-peak' is a case of incomplete filling of PMMA. At high temperature (> 160° C), the behavior of PMMA is more like viscous fluid instead of hyperelastic solid (as discussed in Chapter 4). In a nano cavity, the ratio of the surface area to the volume is very large. The adhesive intermolecular forces between the liquid and a substance are stronger than the cohesive intermolecular forces inside the liquid. Hence, the capillary

force begins to dominate. The capillary force pulls the PMMA fluid on the sidewall of the

cavity. Therefore, PMMA near the sidewall of the cavity is higher than that at the center

until PMMA fills into the cavity completely.

(a1)

(a2)

(b1)

(b2)
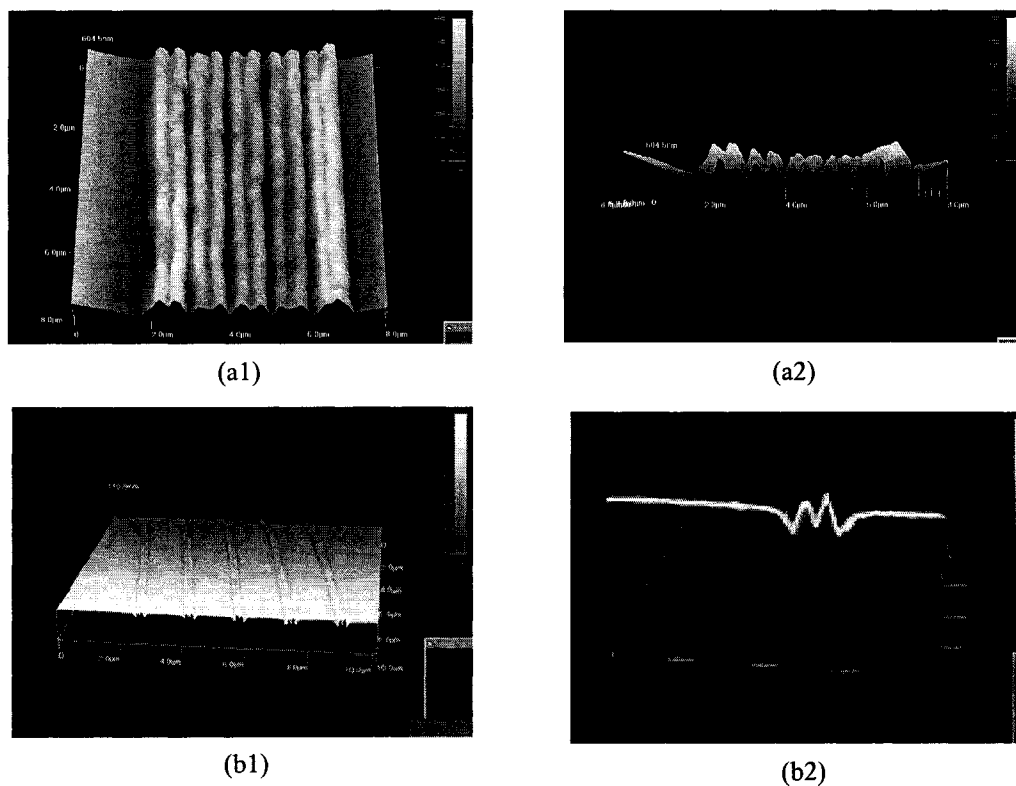
Figure 7.5 AFM pictures of (a1) 'dual-peak' nanowires with 500 nm wide, (a2) Cross section of one of the nanowires with 500 nm wide, (b1) 'dual-peak' nanowires with 100 nm wide, (b2) Cross section of one of the nanowires with 100 nm wide.

CHAPTER 8

EXTENTION OF LIFETIME OF SILICON MOLD

Si mold is the basic tool in the ILL method. The quality of the Si mold directly affects the quality of the final product. Meanwhile, the lifetime of the Si mold determines the cost of manufacturing. Hence, extending the lifetime of Si mold may cut down the production costs.

There are 3 major factors to reduce the lifetime of the Si mold and damage the mold in the ILL method: 1) When Si mold inserts into PMMA, it suffers friction forces from PMMA flow and Al film. The friction may scratch the surface of the mold (Fig. 8.1a). 2) During cutting, the edges of the Si mold suffer maximum concentration stresses. The huge stresses may damage the edges of the Si mold (Fig. 8.1b). 3) In the demolding phase, cooled down and thermally contracted PMMA bandages up the convex structures of the Si mold and generates large friction forces. The frictions which resist the demolding force may pull the mold apart (Fig. 8.1c).

(a)   (b)   (c)
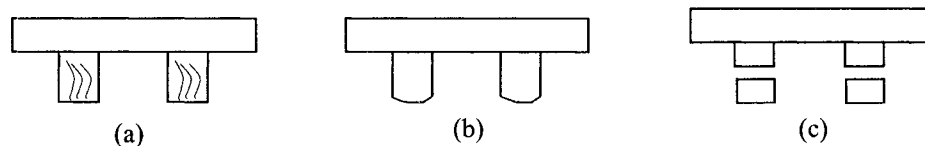
Figure 8.1 Three kinds of damages of Si mold in ILL method: (a) scratch of surface, (b) collapse of edges and (c) break of mold.

In this chapter, some methods are presented to avoid these damages and extend the lifetime of Si mold.

8.1 Design of Patterns and Mold

The life of the Si mold should be considered in the original phase of product design. Reasonable geometry of the Si mold, which will be transformed into patterns, may help to reduce frictions in ILL method.

First, features with high aspect ratio should be avoided. Deep Si structures increase the contact area between the mold and the PMMA, then increase friction. Hence, a deeper mold may have a larger friction force. It makes the Si mold more vulnerable than the relatively shallower molds. Second, it is worth noting to avoid 'neck' structure in design or manufacturing (Fig. 8.2a). The 'neck' structure part of the Si mold is stuck into the PMMA during the insertion of the mold. In the demolding phase, solidified PMMA pulls the 'neck' firmly and breaks the mold (Fig. 8.2b). Third, the smooth surface of the Si mold may reduce the friction force. Last, the coating metal or conducting polymer film should be as thin as possible. In the ILL method, the hard coating film scratches deeper marks than does the softened PMMA. Thinner coating film may help to alleviate the damages from scratch.

(a)   (b)
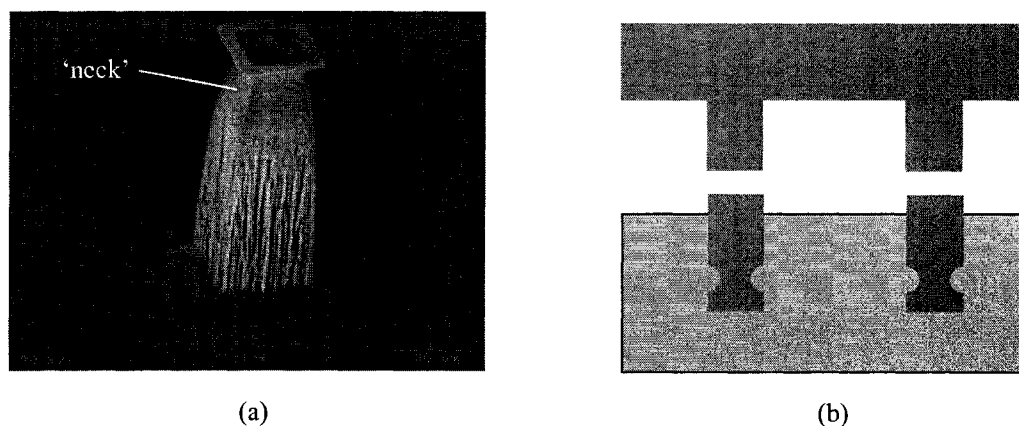
Figure 8.2 (a) SEM picture of a Si mold with 'neck' structure because of undercut. (b) Schematic illustration of breaking mold due to 'neck' structure.

8.2 Anti-Adhesion Coating

The SiO_2 or Si_3N_4 layers on a mold surface have inherent anti-adhesion properties. Therefore, they can be used to prevent adherence problems between the master and the polymer sometimes [67]. However, the effect of anti-adhesion of SiO_2 or Si_3N_4 is not good due to their relatively high surface energy. The water contact angles of Si, SiO_2, and Si_3N_4 surfaces are about 50, 30, and 12°, respectively.

Anti-adhesion coating can effectively reduce the friction force in hot embossing process and decrease the surface energy of the mold surface to prevent a sticking problem [66-70]. Naturally, it can be used in the ILL to alleviate the damages which result from friction force.

Polytetrafluoroethylene (PTFE) (DuPont™ Teflon®) is a synthetic fluoropolymer with an extremely low coefficient of friction. It is often used as a non-stick coating for pans and other cookware. PTFE and PTFE-like materials are also selected as anti-

adhesion coatings for the molds in hot embossing. Anti-adhesive PTFE and PTFE-like film are generally ion-sputtered [66,68] or plasma deposited onto the mold [21,68]. Then, a hydrophilic surface is changed into a hydrophobic surface [21]. R.W. Jaszewski *et. al.* pointed out that the plasma deposited film was of much better quality than the sputtered one [68]. Using SAM technique is another option to coat anti-adhesion film, such as n-dodecanethiol $(CH_3(CH_2)_{11}SH)$ [69] and trideca-fluoro-(1,1,2,2)-tetrahydrooctylsilane (ABCR GmbH) [70].

In this work, a PTFE film was coated on Si molds for anti-adhesion using plasma deposition in an Alcatel 610E ICP machine. A 1-μm-thick film was deposited from the plasma of C_4F_8 flow with 120 SCCM. The work power was 1800 W and deposition time was 1 min.

It is worth noting that the increase in the embossing temperature deteriorates the effect of an anti-cohesion polymer film [73]. Also, the films will decrease with the numbers of hot embossings, and the effect to improve the demolding process will be depressed [66]. In the ILL, anti-adhesion coating could be peeled off by the scratch of hard metal or conducting polymer. Therefore, it is necessary to clean and deposit new films onto the mold before the next embossing.

CHAPTER 9

CONCLUSIONS AND FUTURE WORKS

Stimulated by a macrocutting process used in the manufacturing industry, the ILL method has been developed to fabricate metal micropatterns and applied this method to generate various Al patterns of lateral dimensions ranging from 10 to 300 μm, including channels, lines, square dots, square holes, and truss structures. Al films of thickness ranging from 100 to 500 nm had been patterned by silicon molds of depths of 10 to 100 μm. The effects of imprinting temperatures, thicknesses of Al films, and geometries of silicon mold structures on the patterning results were experimentally investigated, followed by numerical exploration. As a new patterning method, the ILL approach has advantages of simplicity and massive production, and is free of aggressive chemistry. The embossing process parameters of the ILL were optimized by Taguchi methods when using a Si mold with a depth of 40 μm and a Al film with a thickness of 500 nm. Au film and free-standing Al foil were patterned using the ILL to extend its application range. Optical microscope and SEM pictures, maps of element distribution, and electrical resistance were used to examine the patterns.

The ILL has been used to successfully fabricate three conducting polymer-based micro devices: PPy/PEDOT hetrojunctions, Al/PEDOT diodes, and PEDOT/PMMA/PEDOT capacitors. The critica of electrical characteristics (e.g.,

104

breakdown voltage and rectification ratio) of the representative PEDOT/PPy heterojunctions and Al/PEDOT diodes were found close to the values reported in the literatures. High ideality factor of the Al/PEDOT diode was observed. The reason was not clear. The C–V curve of a representative PEDOT/PMMA/PEDOT capacitor was almost a straight line, which was similar to that of a typical parallel metal-plate capacitor.

Furthermore, when nanostructure-formed Si molds were adopted, the ILL was able to generate metal nanowires as well. Compared to micro patterns, MNWs needs higher imprinting temperature and embossing pressure.

Si mold is the key tool in the ILL. Extending the lifetime of the Si molds may reduce the production costs.

The ILL is a new method of pattern transfer and is under development. In the near future, the possibility of removing unwanted materials (i.e., the part of punched materials) from the substrate for cleaning the substrate will be explored, although the unwanted materials do not affect the electrical application of the patterned metal (i.e., the part of nonpunched materials). Furthermore, the following points will be explored:

- This method has been used to generate simple structures and will be used to fabricate complex structures to prove its value.

- Only PMMA is identified as a good intermediate layer. Other polymers which can be used in place of PMMA will be identified.

- The alignment of the mold with the substrate needs to be solved.

REFERENCES

[1] S. M. Sze, *VLSI Technology*, McGraw-Hill Book Company, New York, 2nd ed. (1988).

[2] M. Madou, *Fundamentals of Microfabrication*, CRC Press (1995).

[3] G. T. A. Kovacs, *Micromachined transducers sourcebook*, McGraw-Hill (1998).

[4] H. Shirakawa, E. J. Louis, A. G. MacDiarmid, C. K. Chiang and A. J. Heeger, Synthesis of electrically conducting organic polymers: halogen derivatives of polyacetylene, $(CH)_x$, *Journal of the Chemical Society, Chemical Communications*, 578 - 580 (1977).

[5] X. Liu and C. Luo, An intermediate-layer lithography method for producing metal micropatterns, *Journal of Vacuum Science and Technology B*, **25**, pp. 677-685 (2007).

[6] C. Luo, R. Poddar and X. Liu, An Innovative intermediate-layer lithography approach to replicate micropatterns in a conducting polymer. *Journal of Vacuum Science and Technology B*, **24**(2), L19-L22 (2006) [selected for the April 10, 2006 issue of *Virtual Journal of Nanoscale Science & Technology*].

[7] A. Chakraborty, X. Liu, and C. Luo, An Intermediate-layer Lithography Method for Generating Multiple Microstructures Made of Different Conducting Polymers, *Microsystem Technologies* (in press; available on the journal website).

[8] X. Liu, A. Chakraborty, and C. Luo, Generation of all-polymeric diodes and capacitors using an innovative intermediate-layer lithography, *Advances in Solid-State Technology* (invited book chapter; accepted for publication).

[9] M. S. A. Abdou, Z. W. Xie, J. Lowe and S. Holdcroft, Microlithography of π-conjugated polymers, *Proceedings of SPIE*, **2195**, 756 (1994).

[10] S. Holdcroft and M. S. A. Abdou, Fabrication of electronically conducting polymeric patterns, *US Patent, US 5561030*, (1996)

[11] Y. Xia and G. M. Whitesides, Soft lithography, *Angewandte Chemie International Edition*, **37**, 550-575 (1998).

[12] Y. Xia, J. A. Rogers, K. E. Paul and G. M. Whitesides, Unconventional methods for fabricating and patterning nanostructures, *Chemical Reviews*, **99**, 1823-1848 (1999).

[13] X. Zhao, Y. Xia and G. M. Whitesides, Soft lithographic methods for nano-fabrication, *Journal of Materials Chemistry*, **7**, 1069-1074 (1997).

[14] B. Michel, A. Bernard, A. Bietsch, E. Delamarche, M. Geissler, D. Juncker, H. Kind, J.-P. Renault, H. Rothuizen, H. Schmid, P. Schmidt-Winkel, E. Stutz and H. Wolf, Printing meets lithography: Soft approached to high-resolution patterning, *IBM Journal of Research and Development*, **45**, 697-719 (2001).

[15] S. Y. Chou, P. R. Krauss and P. J. Renstrom, Imprint of sub-25 nm vias and trenches in polymers, *Applied Physics Letters*, **67** (21), 3114-3116 (1995).

[16] S. Y. Chou, P. R. Krauss and P. J. Renstrom, Imprint lithography with 25-nanometer resolution, *Science*, **272**, 85-87 (1996).

[17] S. Y. Chou, P. R. Krauss and P. J. Renstrom, Nanoimprint lithography, *The Journal of Vacuum Science and Technology B*, **14**, 4129-4133 (1996)

[18] J. Wang and T. Cui, Design, Simulation, Fabrication, and Characterization of a PMMA Tunneling Sensor Based on Hot Embossing Technique, *Microsystems Technologies*, **11** (6), 452-455, (2005).

[19] L. W. Pan, L. Lin, J. Ni, Cylindrical plastic lens array by a microintrusion process, *Proceedings of IEEE Micro-Electro-Mechanical Systems Workshop*, 217-221 (1999)

[20] N. S. Ong, Y. H. Koh and Y. Q. Fu, Microlens array produced using hot embossing process, *Microelectronic Engineering*, **60**, 365-379 (2002).

[21] C. Choi, S. Han, B. C. Kim, S. Ahn and M. Jeong, Fabrication of large-core 1 × 16 optical power splitters in polymers using hot embossing process, *IEEE Photonics Technology Letters*, **15**, 825-827 (2003).

[22] L. Martynova, L. E. Locascio, M. Gaitan, G. W. Kramer, R. G. Christensen, and W. A. MacCrehan, Fabrication of Plastic Microfluid Channels by Imprinting Methods, *Analytical Chemistry*, **69**, 4783-4789 (1997).

[23] C. L. Chen and F. Jen, Fabrication of polymer splitter by micro hot embossing technique, *Tamkang Journal of Science and Engineering*, **7**, 5-9 (2004).

[24] J. L. Charest, L. E. Bryant, A. J. Garcia, W. P. King, Hot embossing for micropatterned cell substrates, *Biomaterials*, **25** (2004) 4767–4775.

[25] S. George and H. E. Voegeli, *Principles and methods of sheet-metal fabricating*, Reinhold Publishing Corporate, New York, 2nd ed (1966).

[26] M. J. Painter and R. Pearce, Instability and fracture in sheet metal, *Journal of Physics D: Applied Physics*, 7, 992-1002 (1974).

[27] D. Lowney, T. S. Perova, M. Nolan and P. J. McNally, Investigation of strain induced effects in silicon wafers due to proximity rapid thermal processing using micro-Raman spectroscopy and synchrotron x-ray topography, *Semiconductor Science and Technology*, 17 (10), 1081-1089 (2002).

[28] http://web.utk.edu/~prack/MSE%20300/SEM.pdf

[29] http://www.che.utoledo.edu/nadarajah/webpages/whatsafm.html

[30] H. D. Rowland, A. C. Sun, P. R. Schunk and W. P. King, Impact of polymer film thickness and cavity size on polymer flow during embossing: toward process design rules for nanoimprint lithography, *Journal of Micromechanics and Microengineering*, 15, 2414-2425 (2005).

[31] H. D. Rowland and W. P. King, Simulations of nonuniform embossing: The effect of asymmetric neighbor cavities on polymer flow during nanoimprint lithography, *The Journal of Vacuum Science and Technology B*, 23(6), 2958-2963 (2005).

[32] J. Jeong, Y. Choi, Y. Shin, J. Lee, K. Park, E. Lee, and S. Lee, Flow behavior at the embossing stage of nanoimprint lithography, *Fibers and Polymers*, 3, 113–119 (2002).

[33] M. Worgull and M. Heckele, New aspects of simulation in hot embossing, *Design, Test, Integration & Packaging of MEMS/NOEMS*, 272-274 *(2003)*.

[34] Y. Hirai, M. Fujiwara, T. Okuno, Y. Tanaka, M. Endo, S. Irie, K. Nakagawa and M. Sasago, Study of the resist deformation in nanoimprint lithography, *The Journal of Vacuum Science and Technology B*, 19, 2811-2815 (2001).

[35] Y. Hirai, T. Konishi, T. Yoshikawa and S. Yoshida, Simulation and experimental study of polymer deformation in nanoimprint lithography, *The Journal of Vacuum Science and Technology B*, 22 3288–3293 (2004).

[36] M. Moony, A theory of large elastic deformation, *Journal of Applied Physics*, 11, 582-597 (1940).

[37] L. Lin, Y. T. Cheng, C. J. Chiu, Comparative study of hot embossed micro structures fabricated by laboratory and commercial environments, *Microsystem Technologies*, 4, 113-116 (1998).

[38] V. N. Nair, B. Abraham, J. MacKay, J. A. Nelder, G. Box, M. S. Phadke, R. N. Kacker, J. Sacks, W. J. Welch, T. J. Lorenzen, A. C. Shoemaker, K. L. Tsui, J. M. Lucas, S. Taguchi, R. H. Myers, G. G. Vining and C. F. J. Wu, Taguchi's parameter design: a panel discussion, *Technometrics*, **34**, 127-161 (1992).

[39] Y. K. Shen, A Novel Fabrication Method for the Mold Insert of Microlens Arrays by Hot Embossing Molding, *Polymer Engineering and Science*, 1797-1803 (2006).

[40] J. Antony and F. J. Antony, Teaching the Taguchi method to industrial engineers, *Work Study*, **50** (4), 141-149 (2001).

[41] EDS2004 version 1.2 software user's manual, IXRF Systems Inc.

[42] http://en.wikipedia.org/wiki

[43] J. Ouyang, C. Chu, F. Chen, Q. Xu and Y. Yang, High-conductivity poly(3,4-ethylenedioxythiophene): poly(styrenesulfonate) film and its application in polymer optoelectronic devices, *Advanced Functional Materials*, **15**, 2 (2005).

[44] L. Rupprecht, *Conducting polymers and plastics in industrial application*, Plastics design library, Norwich, New York (1999).

[45] http://www.io.tudelft.nl/research/dfs/idemat/Onl_db/Id123p.htm

[46] R. Kiebooms, A. Aleshin, K. Hutchison, and F. Wudl, Thermal and electromagnetic behavior of doped poly(3,4-ethylenedioxythiophene) films, *Journal of Physical Chemistry B*, **101**, 11037-11039 (1997).

[47] Y. Liu and T. Cui, Polymer-Based Rectifying Diodes on a Glass Substrate Fabricated by Ink-Jet Printing, *Macromolecular Rapid Communications*, **26**, 289–292 (2005).

[48] R. Poddar and C. Luo, A novel approach to fabricate a PPy/p-type Si heterojunction, *Solid-State Electronics*, **50**, 1687-1691 (2006).

[49] Y. Onganer, M. Saglam, A. Turut, H. Efeoglu and S. Tuzemen. High barrier metallic polymer/P-type silicon schottky diodes, *Solid-State Electronics*, **39**, 677-680 (1996).

[50] G. Liang, T. Cui and K. Varahramyan, Fabrication and electrical characteristics of polymer-based Schottky diode, *Solid-State Electronics*, **47**, 691–694 (2003).

[51] Y. Liu, T. Cui, K. Varahramyan, All-polymer capacitor fabricated with inkjet printing technique, *Solid-State Electronics*, **47**, 1543–1548 (2003).

[52] S. O. Kasap, *Principles of electronic materials and devices*, 3rd edition, McGraw-

Hill Inc., New York (1997).

[53] D. Wang, Q. Wang, A. Javey, R. Tu, H. Dai, H. Kim and P. C. McIntyre, T. Krishnamohan, K. C. Saraswat, Germanium nanowire field-effect transistors with SiO_2 and high-k HfO_2 gate dielectrics, *Applied Physics Letters*, **83** (12), 2432-2434 (2003).

[54] F. Patolsky and C. M. Lieber, Nanowire nanosensors, *Materialstoday*, 20-28 (2005).

[55] O. Hayden, A. B. Greytak and D. C. Bell, Core-Shell Nanowire Light-Emitting Diodes, *Advanced Materials*, **17** (6), 701 - 704 (2005).

[56] T. M. Whitney, J. S. Jiang, P. C. Searson and L. Chien, Fabrication and Magnetic Properties of Arrays of Metallic Nanowires, *Science*, **261**, 1316-1319 (1993).

[57] A. J. Yin, J. Li, W. Jian, A. J. Bennett and J. M. Xu, Fabrication of highly ordered metallic nanowire arrays by electrodeposition, *Applied Physics letters*, **79** (3), 1039-1041 (2001).

[58] E. Braun, Y. Eichen, U. Sivan and G. Ben-Yoseph, DNA-templated assembly and electrode attachment of a conducting silver wire, *Nature*, **391**, 775 (1998).

[59] K. Sivakumar, S. Lu and B. Panchapakesan, Metallic and Semiconducting Nanowires from Single Wall Carbon Nanotubes, *Proceedings of Materials Research Society Symposium M*, **818**, M11.48.1-M11.48.6 (2004).

[60] E. C. Walter, M. P. Zach, F. Favier, B. J. Murray, K. Inazu, J. C. Hemminger, and R. M. Penner, Metal Nanowire Arrays by Electrodeposition, *ChemPhysChem*, **4**, 131-138 (2003).

[61] C. Z. Li, A. Bogozi, W. Huang and N. J. Tao, Fabrication of stable metallic nanowires with quantized conductance, *Nanotechnology*, **10**, 221–223 (1999).

[62] N. Kramer, H. Birk, J. Jorritsma and C. Schönenberger, Fabrication of metallic nanowires with a scanning tunneling microscope, *Applied Physics Letters*, **66** (11), 1325-1327 (1995).

[63] Y. Chen, J. Hsu and H. Lin, Fabrication of metal nanowires by atomic force microscopy nanoscratching and lift-off process, *Nanotechnology*, **16**, 1112-1115 (2005).

[64] M. J. Vasile, Z. Niu, R. Nassar, W. Zhang, and S. Liu, Focused ion beam milling: Depth control for three-dimensional Microfabrication, *Journal of Vacuum Science and Technology B*, **15** (6), 2350-2354 (1997).

[65] H. D. Rowland and W. P. King, Polymer deformation and filing modes during microembossing, *Journal of Micromechanics and Microengineering*, **14**, 1625-1632 (2004).

[66] Y. Guo, G. Liu, X. Zhu and Y. Tian, Analysis of the demolding forces during hot embossing, *Microsystem Technologies*, **13**, 411–415 (2007).

[67] C. A. Mills, E. Martinez, F. Bessueille, G. Villanueva, J. Bausells, J. Samitier and A. Errachid, Production of structures for microfluidics using polymer imprint techniques, *Microelectronic Engineering*, **78–79**, 695–700 (2005).

[68] R.W. Jaszewski, H. Schift, P. Gröning and G. Margaritondo, Properties of thin anti-adhesive films used for the replication of microstructures in polymers, *Microelectronic Engineering*, **35**, 381-384 (1997).

[69] N. Lee, S. Choi, and S. Kang, Self-assembled monolayer as an anti-adhesion layer on a nickel nanostamper in the nanoreplication process for optoelectronic applications, *Applied Physics Letters*, **88**, 073101 (2006).

[70] S. Scheerlinck, D. Van Thourhout and R. Baets, Nano Imprint Lithography for Photonic Structure Patterning, *Proceedings Symposium IEEE/LEOS Benelux Chapter*, 63-66 (2005).

[71] J. T. Kim, K. B. Yoon, and C. Choi, Passive Alignment Method of Polymer PLC Devices by Using a Hot Embossing Technique, *IEEE Photonics Technology Letters*, **16** (7), 1664-1666 (2004).

[72] N. Lee, Y. Kim and S. Kang, Temperature dependence of anti-adhesion between a stamper with sub-micron patterns and the polymer in nano-moulding processes, *Journal of Physics D: Applied Physics*, **37**, 1624–1629 (2004).

[73] S. C. Jakeway, H. J. Crabtree, T. Veres and N. S. Cameron, Helge Luesebrink, Thomas Glinsner, Transition of MEMS Technology to Nanofabrication, *IEEE, Proceedings of the International Conference on MEMS, NANO and Smart Systems*, (2003).